

UNCLASSIFIED

AD NUMBER
AD856135
NEW LIMITATION CHANGE
TO Approved for public release, distribution unlimited
FROM Distribution authorized to U.S. Gov't. agencies and their contractors; Administrative/Operational Use; 15 MAR 1965. Other requests shall be referred to Space and Missile Systems Organization, Norton AFB, CA.
AUTHORITY
SAMSO ltr 28 Feb 1972

THIS PAGE IS UNCLASSIFIED

DOC. NO. 543092
COPY NO. 1 REF
TECHNICAL LIBRARY
Aerojet-General Corporation
SACRAMENTO PLANTS

TECHNICAL LIBRARY
AEROJET-GENERAL CORPORATION
SACRAMENTO PLANTS

Enclosure #1

En/

SACRAMENTO PLANT

AD856135

PERFORMANCE CHARACTERISTICS AND ANALYSIS OF LIQUID-INJECTION THRUST-VECTOR CONTROL

TM-16-SRO

15 March 1965

FOR REFERENCE ONLY
Not to be taken from Library

D D C
RECEIVED
AUG 7 1969
RECEIVED



AEROJET-GENERAL CORPORATION
SACRAMENTO, CALIFORNIA

15 MARCH 1965

TECHNICAL MEMORANDUM 16 SRO

PERFORMANCE CHARACTERISTICS AND ANALYSIS OF
LIQUID-INJECTION THRUST-VECTOR CONTROL

STATEMENT #2 UNCLASSIFIED

This document is subject to special export controls and each transmittal to foreign governments or foreign nationals may be made only with prior approval of SAMSO (SMSD)

L. A. AFS, CALIF. 90045

by

J. D. MOCKENHAUPT

Development Engineer

Fluid Mechanics Section

APPROVED FOR DISTRIBUTION:

M. J. DITORE
M. J. DITORE, Manager
Aerophysics Programs

8825T

TM-16-SRO

PREFACE

The analysis described in Section IV was conducted for the Minuteman Wing VI motor development program under Air Force Contract AF 04(694)-258. The compilation of experimental data and the writing of this report were supported by company-sponsored independent research and development funding. Acknowledgment is made to O. J. Demuth, Assistant Manager, Advanced Design and Technology Department, M. J. Ditore, Manager, Aerophysics Programs, and S. A. Lorenc, Supervisor, Fluid Mechanics Section, for their helpful advice and assistance, which contributed significantly to the completion of this report.

SUMMARY

The current available information concerning liquid-injection thrust-vector control from the standpoint of both system performance and analysis is summarized in this report. A detailed description of the complex flow field created by the injection of a liquid into a supersonic nozzle is given on the basis of both experimental information, including pressure measurements and visual evidence, and the theory of compressible fluid flow. Also included is a brief discussion of the important individual processes, such as penetration, atomization, vaporization, and chemical reaction, which are integral parts of the overall flow interaction. Overall system performance and the effects of the many injection parameters are then considered and illustrated with experimental data from a number of sources. The final portion of the report deals with analytical methods for predicting the performance of liquid-injection TVC systems. In particular, a theoretical model based on a detailed flow field solution, which has been under development at Aerojet, is described in detail. Because of a lack of funding, this model was not fully completed. Thus, the last section contains the specific tasks that will be undertaken to complete the model when funding again becomes available.

TABLE OF CONTENTS

	<u>Page</u>
I. Introduction	1
II. Discussion of Flow Field	5
A. General Description	5
B. Effect of Vapor Body Size and Shape	7
C. Details of Individual Processes	9
III. Performance Characteristics	13
A. Typical System Performance	13
B. Significant Parameters	14
C. Axial Thrust Augmentation	26
D. Scale Effects and Dynamic Response	27
IV. Analytical Approaches	29
A. Summary of Previous Work	29
B. Current Aerojet Preliminary Model	34
V. Recommendations for Future Work	40
VI. Conclusions	43

APPENDIXES

	<u>Appendix</u>
Vapor-Body Calculations	A
Flow-Field Solution	B

FIGURE LIST

	<u>Figure</u>
General Flow Pattern for Liquid-Injection TVC	1
Flow Separation Patterns	2
Effect of Liquid-Jet Penetration on Flow Pattern	3
Shadowgraphs for Liquid-Nitrogen Injection Through a Flat Plate	4
Schlieren and Spark Shadowgraphs for Flat Plate Tests with Freon 12	5
Schlieren Photographs from Two-Dimensional Nozzle	6
Photograph of Freon-114B ₂ Injection During Hot Firing of Solid Propellant Motor	7
Measured Pressure Distributions for LITVC	8
Flash Vaporization	9
Typical Liquid-Injection TVC Performance Curves	10
Performance of Various Liquid Injectants (A) (u)	11C*
Performance of Various Liquid Injectants (B)	12
Effect of Port Diameter and Injection Pressure (u)	13C
Comparison of Injection Systems (u)	14C
Effect of Motor Chamber Pressure and Injection Pressure (u)	15C
Shock Reflections Produced by Liquid Injection	16
Effect of Injector Location	17
Effect of Injector Location for Single and Multi-port Injectors (u)	18C
Effect of Nozzle Shape on Optimum Injector Location (u)	19C
Effect of Injection Angle	20
Effect of Injection Angle and Location	21
Effect of Orifice Spacing for Multi-port Injectors (u)	22
Effect of the Number of Ports in a Multi-port Injector (u)	23 D
LITVC Performance During Motor Tail-Off	24 D
Effect of Nozzle Expansion Ratio	25
Effect of Nozzle Contour at Optimum Injector Location (u)	26 D
Axial Thrust Augmentation due to Liquid Injection	27
Effect of Injector Location and Injection Angle on Axial Thrust Augmentation	28
Liquid Injection Linearized Model	29
Liquid Injection Vapor-Body Model	30

* C Figures Are Contained in Supplement to This Technical Memorandum

D Omitted

FIGURE LIST (cont.)

	<u>Figure</u>
Correlation of Experimental Data with Approximate Model	31
Correlation of Experimental Liquid Injection TVC Performance Data (u)	32C
Comparison of Calculated Vapor Bodies with Injectant Erosion Patterns Measured on Nozzle Wall	33
Pressure Rise and Equivalent Cone Angle for Turbulent Boundary Layer Separation	34
Typical Flow Field Solution	35
Calculated Shock Intersection with Nozzle Wall	36
Comparison of Calculated with Measured Pressure Distributions	37
Comparison of Calculated with Measured Shock Waves	38

I. INTRODUCTION

The objectives of this report are:

- a. to promote a better understanding of the complex flow interaction associated with liquid-injection thrust-vector control (LITVC);
- b. to provide information that can be utilized for preliminary LITVC system design;
- c. to indicate the present status of analytical efforts that have been directed towards the development of a theoretical model for performance prediction.

Experimental data from all known sources to date have been compiled with the first two objectives in mind. These data, especially those of a more fundamental nature such as measured pressure distributions and schlieren photographs, have been used to supplement compressible flow theory in the discussions of the various facets of the liquid-injection flow field. Actual performance data have been carefully selected to illustrate the effect of each injection or motor parameter on system performance. This information, as presented in Section III, should enable the design engineer to determine approximately the performance to be expected from any given system and should also provide a means for selecting the proper parameter values for specific applications.

The sections of the report devoted to the analytical aspects of LITVC have been included to describe the approach taken here at Aerojet to develop a suitable comprehensive model, the progress that has been made to date on that model, and the steps required for its final completion. It is anticipated that soon after the conclusion of a present independent research and development experimental program, which will supply much needed flow field data, another report will follow; this report will describe the finished model.

I, Introduction (cont.)

The feasibility of thrust-vector control by fluid injection was first demonstrated in 1952 by G. F. Hausmann at United Aircraft.¹ By injecting a secondary gas cross-stream into the divergent section of a supersonic nozzle, Hausmann showed that a lateral force exceeding the magnitude of the secondary stream momentum was produced. The additional force was a direct result of the interaction of the two streams within the nozzle, which caused the formation of a local high-pressure region along the nozzle wall in the vicinity of the injector. In subsequent tests by a number of investigators,^{2,3, and 4} it was found that this interaction force was strongly dependent on such injection parameters as the location and configuration of the injector, the injectant flow rate, and the properties of the injectant itself. These initial experiments were all performed with gaseous injectants, but because of material problems with hot gases and bulky system requirements for cold gases, the use of a liquid injectant was proposed, which was proved feasible by NOTS in 1959.⁵

The first class of liquid injectants to be considered were those which readily vaporized when encountering the high temperatures within the nozzle. Of all the liquids of this type tested, the Freon group emerged as the most successful. However, it was soon discovered that injectants which chemically react with the main stream gases to liberate heat would produce greater side forces per pound of injectant. This led to the investigation of such liquids as nitrogen tetroxide, UDMH, hydrazine, bromine, and perchloroethylene, which, in addition to giving relatively high performance, also created toxicity and corrosion problems. To combat these latter effects, sodium perchlorate and strontium perchlorate solutions in water were tested at Aerojet^{6,7} and were found to have completely acceptable storage and handling characteristics, while still producing higher performance than the Freons.

Initially, the injectors consisted only of a single port in the nozzle wall, but further efforts to increase performance, resulted in multiport configurations in which the ports were spread circumferentially. This spreading of the disturbance along the nozzle wall proved to be successful as long as the distance between adjacent ports was not excessive.

1, Introduction (cont.)

The liquid-injection TVC concept emerged from the feasibility stage when it was adopted for use on three major solid-rocket motors. Both the Polaris A3 and Minuteman Wing VI second stages have flown successfully with an injection system using Freon 114B2 and a three-port injector. For the Titan III 120-in.-dia solid rocket booster, an N_2O_4 system consisting of six ports evenly spread over each 90° quadrant was selected. Excellent test results have been reported for this configuration.

The liquid-injection system has a number of advantages over other methods of thrust-vector control. Since there are no mechanical parts exposed to the propellant gases, the material problems usually associated with today's high temperature, particle-laden propellants are minimized. Also, the injection of a secondary fluid causes an increase in the axial thrust instead of a thrust loss as experienced with jetavators, jet tabs, and swiveled nozzles. Another very useful characteristic of this type of system is a very fast response, or an extremely short time lag between the command signal and application of the full control force. Since there is no break in the flow passage from the chamber through the nozzle, as with gimbaled or swiveled nozzles, nozzle design is simplified. Some additional advantages include applicability to all nozzle sizes and a decreasing system weight throughout the flight as the injectant is expended.

Of course, this system also has certain disadvantages. From a performance standpoint, the most serious drawback is the relatively poor performance at high jet-deflection angles. Deflections over 6° are usually difficult to obtain, which limits booster applications. The entire injection system can become quite complicated when such areas as pressurization, tankage, and valving are carefully considered. Finally, the possibility always exists of the injectant supply being exhausted before the end of the flight, leaving the vehicle without means of control.

The suitability of this system for a particular application must therefore be determined through trade-off studies considering system performance, weight, and

I, Introduction (cont.)

reliability. In such a study conducted by Space General for a typical vehicle, liquid injection was not recommended for the first-stage motor, but was found to be very competitive with other methods of thrust-vector control for the upper stages.⁵¹

II. DISCUSSION OF FLOW FIELD

A. GENERAL DESCRIPTION

When a liquid is injected cross-stream into a nozzle, it will penetrate as a solid jet a short distance into the supersonic gas stream before shattering into droplets. The drag forces acting upon these droplets carry them downstream, while the high temperatures of the gases cause the injectant to vaporize. The vapor thus generated forms a body along the nozzle wall, which acts as an obstruction to the primary flow. The resulting flow field, shown schematically in Figure 1 for a single port, is very similar to the interference pattern produced by a solid blunt body.

The primary feature of this flow field is a three-dimensional bow shock which stands slightly upstream of the injection port and spreads both radially and circumferentially as it extends downstream. At the intersection of the shock with the nozzle wall, the disturbance can spread upstream through the subsonic portions of the boundary layer. If the shock is sufficiently strong, the abrupt streamwise pressure gradient can cause the boundary layer to separate from the nozzle wall.

In the vicinity of the injector, where the shock is strongest, the boundary layer separates upstream of the bow shock and reattaches to the vapor body, thus modifying the effective shape of the obstacle. The presence of this separation region at the nose of the vapor body causes the shock pattern near the injector to differ somewhat from the pattern without a boundary layer. The bow shock is closer to the body, and the compression waves generated near the separation point merge into an oblique shock, which then intersects the bow shock to form the bifurcated pattern shown in Figure 2a. The size of this separation region depends on both the height and width of the body. At low injectant flow rates with little penetration, the separated region merges rather smoothly into the vapor body, causing the separation shock to be the main shock as shown in Figure 3a. At the other extreme, such as a single liquid jet penetrating far into the nozzle as in Figure 3b, the separation region will be relatively small, with the bow shock the dominating feature of the flow field. In addition, the size of the separation zone for a given body increases for greater boundary layer thicknesses.

II, A, General Description (cont.)

Downstream of the injector, the separated boundary layer reattaches to the nozzle wall, as shown in Figure 2b, in a manner similar to the shock-boundary layer interaction produced by the reflection of an oblique shock. The size of this separation region depends on the shock strength, both decreasing as the shock moves closer to the exit plane.

Photographic evidence of some of these flow patterns is presented in Figures 4 through 7. The shadowgraphs shown in Figure 4 were taken at the JPL 20-in. Supersonic Wind Tunnel during the injection of liquid nitrogen through a single port in a flat plate.⁸ For free stream Mach numbers of 2.01, 2.61, and 3.26, both vapor body and bow shock are plainly visible. The relatively small separation region can be attributed to the thin boundary layer and, most probably, to a body width much smaller than the body height. This last statement can only be postulated, of course, since there is no direct evidence of the vapor body dimension in the plane of the plate. However, it does appear reasonable because of the relatively small diameter of the single port, the high injection pressure, and small injectant flow rate.

Figure 5 is a schlieren photograph taken at the same JPL wind tunnel for $M = 2.01$, but with Freon 12 as the injectant and a 3-port injector.⁹ In this case, the separation region and shock are more prominent than in the liquid nitrogen case due to the greater lateral spreading of the vapor, relatively small penetration, and a thicker boundary layer.

The effect of an accelerating free stream was included in the tests performed at Stanford with injection through a single port into a two-dimensional nozzle.¹⁰ The overall flow pattern, Figure 6, for liquid nitrogen is quite similar to the flat plate case. In addition to the schlieren photographs, an indication of the shock and body dimensions in the plane of the nozzle wall was also found in these experiments by using a china-clay technique to show the flow pattern along the wall. These dimensions proved to be much less than the corresponding ones in the plane of the schlieren photographs, thus supporting the presence of the relatively small separation region.

II, A, General Description (cont.)

For an axisymmetric nozzle, flow visualization techniques must be replaced by thorough wall-pressure measurements, to determine details of the flow field. However, the Minuteman project at Aerojet, during an actual firing, mounted a camera just outside and above the exit plane of a nozzle, looking down the inside of the nozzle towards the throat. Figure 7 is one of the photographs taken during the injection of Freon 114B₂ through a single port, and shows the vapor body and the shock along the nozzle wall.

A typical pressure distribution for Freon 114B₂ injection through a 3-port injector in the Minuteman Wing VI nozzle is shown in Figure 8. This nozzle is contoured with an overall 24.8:1 expansion ratio, and the injector is located at an expansion ratio of 8.25:1. This pressure distribution is typical of most liquid-injection cases with the small high-pressure region near the injector, the overall decrease in pressure in the axial direction approaching the undisturbed value, and the pressure increase from the injector centerline to the shock in the circumferential direction downstream of the injector. The major portion of the total side force, about 70%, is contributed by the downstream region, while the high pressure separation region accounts for 20% and the injectant momentum the final 10%.

Similar pressure distributions were obtained at JPL⁴⁰ for Freon 12 injected through a single port into a conical nozzle. With the single port, the side-force contribution from the separation region was only approximately 10%.

B. EFFECT OF VAPOR BODY SIZE AND SHAPE

The formation of the vapor body is an extremely complex phenomenon in which the interrelated processes of atomization, vaporization, mixing, and, in some cases, reaction occur simultaneously. The size and shape of the vapor body is determined primarily by the initial penetration of the liquid stream, the rate of vapor generation, and the injector configuration. To produce the maximum side force, the body height should be large initially to produce a strong shock and large separation

II, B, Effect of Vapor Body Size and Shape (cont.)

region, and continue to increase downstream to prevent the pressure levels in this relatively large area from falling too low. A stronger shock is also produced by a greater body width as the three-dimensional flow over and around the body approaches the limiting two-dimensional case where all the flow must go over the body.

The initial height depends upon the combination of penetration and rate of vapor generation. For low penetration, the boundary of the vapor body is determined primarily by the volume of vapor generated, which is then free to spread in the cross-sectional plane both away from the wall and along it. When the penetration is high, however, the body height is mainly a function of the trajectory of the liquid jet and droplets, with a corresponding elongation of the vapor cross-section. For a single port, this might allow more of the primary flow to spill around the vapor body rather than being forced over it, which would then result in lower pressures along the nozzle wall away from the body. For a multiport injector, this decrease in body width per port might permit some of the primary flow to bleed between adjacent ports, also causing lower pressures. This initial loss could be compensated for, however, if the greater mixing provided by this multiport configuration resulted in a larger vapor body downstream due to improved vaporization and/or more complete chemical reaction. Thus, there definitely appears to be an optimum penetration, depending upon the injectant and injector configuration.

After this initial deflection and compression of the primary flow caused by the "nose" of the vapor body, the flow expands again as it follows the body contour and approaches its original direction. Thus the downstream pressure distribution is governed by the slope of the vapor body boundary, which depends on the amount of vapor generated, the mixing of the vapor and free stream, and the degree of chemical reaction. The total side force is, therefore, largely determined by the vaporization process.

For a relatively inert injectant, such as Freon, the maximum side force may be produced by a controlled, rather than instantaneous vaporization, which would result in an increasing vapor body size approaching the nozzle exit. If vaporization occurs

II. B, Effect of Vapor Body Size and Shape (cont.)

too quickly, the downstream pressure will fall rapidly and may drop below the undisturbed value as with gas injection. On the other hand, the maximum body size will not be produced if the vaporization is not completed before reaching the nozzle exit.

For a reactive injectant, however, vaporization and mixing must first take place before the chemical reaction can be initiated. Thus it would be advantageous in this case to vaporize the injectant quickly to give the vapor a chance to mix and react.

C. DETAILS OF INDIVIDUAL PROCESSES

1. Penetration

There are essentially three factors affecting the penetration of a liquid jet into a cross-current high velocity gas stream:

- a. the momentum of the jet relative to the free-stream;
- b. the break-up of the jet into droplets;
- c. the shape and solidity of the jet.

For a supersonic free-stream, additional factors may enter due to the shock-wave formation upstream of the injector. Also, vaporization of the liquid and possible reaction in both liquid and vapor phases could produce significant effects.

The important penetration parameters can be found by considering their effect on the above factors. These parameters can be grouped generally as free-stream properties, injectant properties, and injector design.

The primary local free-stream parameters are static and dynamic pressures, which, for a given gas, are functions of total pressure and Mach number. The combination of low total pressure and high Mach number will produce low values for both local pressures, thus promoting penetration. The secondary effects of shocks and vaporization depend on the free-stream total temperature and Mach number, while the gas

II, C, Details of Individual Processes (cont.)

composition affects any chemical reaction. A slight reduction in penetration would most probably result from these secondary effects.

Finally, the injector design can be quite significant since the velocity, and thus momentum, of the liquid jet is determined by the pressure drop across the injector and the port-discharge coefficient. The penetration is also a direct function of the port size, and the exact form of this relation will determine whether a scaling effect exists for any particular case. Since a solid stream will penetrate farther than a spray, the jet solidity, which depends upon the contour of the port internal flow passage, is also an important factor.

As mentioned previously, there does appear to be an optimum amount of penetration that will produce the greatest side force for any particular case. In general, the optimum value should be greater for reactive injectants and multi-port injectors. If a scaling effect does exist, it will probably be more difficult to attain this best penetration in the larger nozzles.

2. Atomization

After the initial penetration of the liquid jet, the stream is broken up into droplets by the interaction of aerodynamic, viscous, and surface tension forces. Experimental investigations of this atomization process^{11,12,13,14} have shown that the size of these droplets depends on both free stream and injectant properties, as well as the shape of the jet. To promote the formation of smaller droplets, the free-stream density, and the velocity should be high and the injectant viscosity and surface tension low. In addition, the size of the jet, which is related to the port diameter and injector configuration, should be small.

Small droplets are desirable since they result in greater amounts of vapor being generated within the nozzle. This can be attributed mainly to the additional total surface area furnished by a large number of small droplets as opposed to

11, C, Details of Individual Processes (cont.)

a smaller number of larger droplets comprising the same total mass. This larger area allows better heat transfer to the liquid, and thus faster vaporization.

3. Vaporization

Two different types of vaporization can occur within the nozzle: flash vaporization and vaporization due to heat transfer. Flash vaporization takes place when the liquid injectant is suddenly brought into an environment in which the pressure is below the vapor pressure of the liquid at its initial temperature. The temperature thus must drop for the injectant to reach an equilibrium state at the given pressure (see Figure 9), with the heat loss by the liquid utilized for vapor generation. The amount of vapor produced in this manner will be promoted by a high initial injectant temperature, a low final pressure, and a relatively flat vapor pressure curve. In most instances, the final product will be a liquid-vapor mixture, with the end state on the vapor pressure curve. However, in extreme cases, the liquid might be completely vaporized, so that the final state will be in the vapor region, and thus at a lower temperature than the liquid-vapor mixture at the same pressure.

The most prevalent form of vaporization is a direct result of the heat transfer between the injectant and the hot gases within the nozzle. It depends not only on the injectant and free-stream properties but also the physical mechanisms of mixing and atomization. In general, this vaporization will be promoted by:

- a. High free-stream temperatures;
- b. High free-stream and vapor thermal conductivity;
- c. Low free-stream and vapor specific heat;
- d. Low injectant temperature;
- e. Low injectant heat of vaporization;
- f. Low injectant density;
- g. High relative velocity between the free stream and liquid droplets;
- h. Good atomization (small droplets);
- i. Good mixing between the free stream and vapor.

II, C, Details of Individual Processes (cont.)

For injection into sea-level nozzles, this latter form of vaporization will be predominant, but flash vaporization could become significant in high-expansion-ratio nozzles, and will be the primary form in cold-flow experiments.

4. Reaction and Mixing

If an exothermic chemical reaction occurs between the species of the free stream and the injectant (liquid or vapor), the heat generated increases the amount of jet deflection by:

- a. causing the vapor body to expand, thus forming a larger obstruction;
- b. transmitting heat into the primary flow, which has been shown¹⁵ to be analogous to mass addition with resulting higher pressures.

The molecular weight of the reaction products as compared to that of the reactants is also important in determining the final body size. The choice of an optimum reactive injectant will thus depend on the composition of the primary flow, the heat of reaction, and the reaction products. To encourage this reaction, the mixing of the injectant with the free stream should be promoted, and since most reactions occur with the injectant vapor phase, vaporization should be accelerated.

As more of the free-stream gases mix with the injectant vapor, two opposing effects occur. The vapor-body size is increased due to higher temperatures, greater vaporization, and greater reaction, but less of the free stream is being deflected. However, in a study conducted at Aerojet using a computer program for turbulent mixing with chemical reactions,¹⁶ the overall effect of greater mixing was the production of a larger effective vapor body, and thus greater jet deflection or side force. This was especially true in the case of chemical reaction.

III. PERFORMANCE CHARACTERISTICS

A. TYPICAL SYSTEM PERFORMANCE

The final criterion to be used in evaluating any given liquid-injection thrust-vector-control system is, of course, the performance of that system, i.e. the amount of side force produced by a given injectant flow rate, or conversely, the injectant flow rate required for a given amount of side force. To present system performance, either of the curves shown in Figure 10 are most frequently used.

The first, sometimes referred to as the "gain curve", shows side force as a function of injectant flow rate, with the motor thrust and mass flow used to nondimensionalize the variables. It is convenient to present the performance in terms of these ratios since the side force ratio (F_s/F_A) is the arctangent of the resultant jet deflection angle, and the mass flow ratio (\dot{w}_s/\dot{w}_A) is a scaling parameter that enables the performance of different size motors to be compared.

The second curve shows the injectant specific impulse, $(I_s)_s$, or the side force per unit injectant flow rate, as a function of the side-force ratio. Since the system requirements are usually stated in terms of jet deflection, this latter curve allows the efficiency of the L1VC system to be evaluated for given requirements.

Either of these two curves can readily be transformed to the other, since, for a constant motor specific impulse, straight lines emanating from the origin represent lines of constant $(I_s)_s$ in the gain curve, and constant \dot{w}_s/\dot{w}_A in the I_s curve.

The shape of the curves in Figure 10 are typical for a constant injection pressure system. As the injectant flow rate increases, the slope of the gain curve tends to level off, and in some cases, will actually become negative due to the reflection of the shock off the opposite nozzle wall. Thus, for a given set of injection conditions, there is a maximum side force, which usually occurs at a very high injectant flow rate.

III, A, Typical System Performance (cont.)

The loss in system efficiency at the higher mass flow and side force ratios is indicated by the I_s curve of Figure 10. The higher the jet-deflection requirement, the lower the injectant specific impulse. Thus, at the maximum side-force condition for the system, the (I_s) s is usually so low, that it would not be desirable to operate the system at this point.

B. SIGNIFICANT PARAMETERS

Since the mechanism producing the side force is so complex, it is not surprising to find that system performance is sensitive to a large number of parameters. These parameters can be grouped in the following manner:

1. Injection parameters
 - a. injectant properties
 - b. port diameter and injection pressure
 - c. injector location
 - d. injector configuration
 - e. angle of injection
2. Motor parameters
 - a. chamber conditions
 - b. propellant properties
 - c. nozzle size and shape

In general, the effect of each parameter can be deduced from experimental data, and by considering the flow field and individual processes discussed in the previous section, these effects can usually be logically explained. However, with so many parameters, it is sometimes very difficult to isolate a single parameter and its effects, since a change in one parameter may necessarily cause a corresponding change

III, B, Significant Parameters (cont.)

in some other parameter. An example of this is the relationship between injectant flow rate, port area, and injection pressure. It is not possible to change only one of these parameters for a given injectant.

1. Injectant Properties

Liquid injectants can in general be grouped into three classes:

- a. inert liquids,
- b. reactive liquids,
- c. monopropellants or bipropellants.

The inert liquids essentially do not react with the propellant gases of the primary flow, and thus depend primarily upon vaporization to produce the body of vapor which forms the flow obstruction. Since the vaporization requires energy from the free stream, the effective flow deflection is somewhat reduced. In the inert liquid class, the Freon compounds have been found to produce the best performance due largely to their low heats of vaporization. Freon 113 and 114B₂ have been extensively used since their relatively high liquid density reduces tankage requirements.

Reactive liquids, due to chemical reaction with the propellant gases, usually liberate heat within the nozzle, which not only tends to increase the size of the vapor body by increasing temperature and the amount of gas generation, but, in transferring energy to the primary flow, also tends to increase the flow deflection. Since most propellant gases are fuel rich, the most successful reactive injectants have been oxidizers, such as nitrogen tetroxide and hydrogen peroxide. Because of storability and corrosion problems associated with these particular liquids, a new class of liquid oxidizers arose - perchlorate salt solutions. Excellent performance has been obtained with saturated water solutions of sodium, strontium, and lead-perchlorates, and by using a reactive solvent such as hydrogen peroxide, this performance was further increased. With a reactive solvent, however, the storability and corrosion problems again arise, but would not be as significant as in the case of the solvent alone used as the injectant.

III, B, Significant Parameters (cont.)

In the third class of injectants, the monopropellants and bipropellants, the injectant itself reacts as soon as it is raised to a sufficiently high temperature. Thus, the performance of these injectants does not greatly depend on the composition of the propellant gases as with the reactive liquids. In actual tests with typical liquid and solid propellants, the performance of such injectants as hydrazine, UDMH, Cavea-B nitromethane, UDMH-hydrazine, and UDMH-IRFNA have in general been greater than the inert liquids, but less than the oxidizers. One scheme that has been proposed to increase the performance of monopropellants and bipropellants is the use of a pre-combustion chamber to initiate the chemical reaction just before the injectant enters the nozzle. Thus, some of the greater performance associated with a gas injectant could be realized.

A wide range of liquid injectants have been tested at Aerojet^{41,42}, NOTS⁵, and Lockheed³⁰ in actual hot firings and some of the results of these tests are shown in Figures 11C* and 12. In these figures, the relative performance of different injectants can be compared for the same injection and motor parameters. It should be noted, however, that some injectants may be more sensitive than others to certain parameters, which could cause a shift in relative performance levels. A good example of this is the greater effect the propellant gas composition and temperature have on the performance of reactive liquids than on inert liquids, monopropellants and bipropellants.

In addition to performance, the final selection of an injectant for a given application will depend greatly on such properties as density, corrosiveness, toxicity, and storability, which will affect the size, weight, complexity, and reliability of the injection system.

* Figure numbers designated with the letter "C" are contained in the confidential supplement to this report.

III, 1, Significant Parameters (cont.)

2. Port Diameter and Injection Pressure

The effects of port diameter and injection pressure cannot be determined separately, since at a given injectant flow rate one cannot be varied without causing a corresponding change in the other. The port diameter is an important parameter in the atomization process, with smaller droplet sizes, and subsequently faster and more efficient vaporization, resulting from the smaller port sizes. The penetration of the liquid jet, which affects both the initial strength of the main shock and the size of the separation region, is primarily a function of the initial injectant velocity, which in turn depends greatly on the injection pressure. Therefore, in most cases it would appear that the combination of a small port and high injection pressure would produce the best performance at a given injectant flow rate. This trend is illustrated in Figure 13C, where the lines of constant injection pressure and constant port diameter are shown in the I_s plot for a single port injector.

The question that now naturally arises is which of the two methods of varying injectant flow rate is preferable - constant port area with variable injection pressure, or constant injection pressure with variable port area. To compare the performance of the two systems, they must be matched at some particular design point. The natural choice for this design point is the maximum injectant flow rate, for which the highest injection pressure and largest port size would be required. At the lower flow rates then, the constant pressure system would have a larger injection pressure and smaller port size, thus producing greater penetration and higher side forces. The performance of the constant area system would be especially poor at the very low flow rates, where with the low injection pressures, the injectant may barely penetrate the boundary layer.

A good comparison of the two systems is given in Figure 14C where the typical performance curves for each system are shown. Unlike the curves previously discussed for a constant pressure system, the gain curve for a constant

III, B, Significant Parameters (cont.)

area system has an inflection point, with a corresponding maximum in the I_s curve. Thus, in the low flow range, the efficiency of a constant area system decreases at the smaller injectant flow rates, while the constant pressure system efficiency increases.

The trend of increasing performance with increasing injection pressure at a given flow rate does not hold indefinitely as illustrated in Figure 15C. In the previous section, it was concluded that an optimum amount of penetration did exist. This conclusion is supported by the fact that there is an optimum injection pressure, which varies with motor chamber pressure. For higher pressures within the nozzle, higher injection pressures are required to reach the optimum penetration.

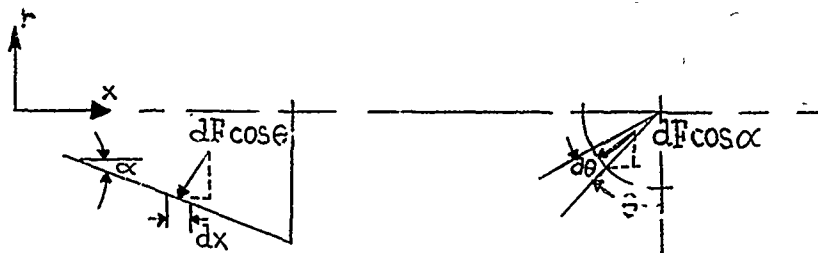
3. Injector Location

There are a great number of factors to be considered in determining the optimum injector location.. From an aerodynamic viewpoint, as the injector is moved closer to the throat, the shock wave becomes steeper, for a given flow deflection, because of the lower free-stream Mach number. Thus the nozzle wall area covered by the disturbance increases. Also, despite the fact that the shock strength is less at the lower Mach numbers, the difference between the pressures behind the shock and the free-stream pressures is still greater for locations closer to the throat since the free-stream pressures are higher. The combination of larger area and greater pressure differences would produce higher side forces, so that from strictly aerodynamic considerations, the optimum injector location should be as close to the throat as possible. However, two other important factors must be considered - nozzle geometry and vapor body size.

Due to the circular cross-section of a nozzle, the nozzle geometry tends to reduce performance as the injector is moved closer to the throat. This

III, B, Significant Parameters (cont.)

effect can best be explained by first setting up a cylindrical coordinate system (r, θ, x) with the nozzle center line as the x axis and the injector located on the nozzle wall at $\theta = 0^\circ$.



Since the pressure force always acts normal to the nozzle wall, a differential force

$$dF = PdA = Pr d\theta \frac{dx}{\cos \alpha}$$

acting at any point on the wall, will have the following component contributing directly to the side force:

$$\begin{aligned} dF_s &= dF \cos \theta \cos \alpha \\ &= (P r d\theta dx) \cos \theta \end{aligned}$$

As θ increases, df_s becomes smaller, and for $90^\circ < \theta < 270^\circ$, a negative side force component is produced. Therefore, as the pressure disturbance spreads along the nozzle wall in the circumferential direction, it becomes less effective in producing a side force. As the disturbance spreads substantially into the upper half of the nozzle, an actual decrease in side force may result.

This performance loss due to geometry, sometimes called "curvature loss," will become more predominant as the injector is moved closer to the throat. The steeper shock waves at these locations tend to further aggravate the problem. Figure 16 illustrates a situation in which the injector was too close to the throat in a Minuteman nozzle³⁵ and the shock wave was hitting the opposite nozzle wall.

III, B, Significant Parameters (cont.)

- 6 Pressure taps were located at various x stations at $\theta = 180^\circ$, and the shock reflection was clearly indicated by a sharp rise in pressure, which moved upstream as the injectant flow rate increased. The gain curve for this test is shown in Figure 24, and is extremely "flat" for $\dot{w}_s/\dot{w}_A > 0.15$.

The final factor that must be considered in a discussion of the optimum injector location is the size of the vapor body, which determines the initial flow deflection and the downstream pressure distribution. For a given flow rate and injection pressure, the penetration of the liquid jet will be less at locations nearer the throat and the volume occupied by the resulting vapor near the injector will be smaller due to the higher free stream pressures. Thus, the initial flow deflection will be less. However, the higher free-stream temperatures and greater distance to the nozzle exit will promote vaporization, mixing, and reaction, which will tend to produce higher downstream pressures as long as these processes have not been completed within the nozzle.

To summarize then, the injector should be located

- a. Close to the throat to optimize the aerodynamic effects;
- b. far from the throat to minimize the losses due to the geometrical effects;
- c. at some intermediate point to optimize vapor body size.

Thus, there is definitely some optimum location, which will depend upon the relative importance of each of the above three factors. Such an optimum location is clearly shown in Figure 17, where for this particular case, the maximum side force for a given flow rate would be produced by injection at $x/L = 0.45$ (x = axial distance from throat to injector, L = nozzle length).⁵ As the flow rate is increased, the location of this maximum usually shifts slightly downstream as the geometrical effects become more significant.

III, E, Significant Parameters (cont.)

A multiport injector also tends to shift the optimum location downstream, since this injector spreads the disturbance more circumferentially than a single port. The curvature losses, therefore, become effective sooner as the injector is moved towards the throat. Figure 18C compares the effect of injector location on a single port and multiport injector for the same nozzle.

One point that has been a source of confusion for some time is the variation of optimum location from nozzle to nozzle. This variation has been quite significant, ranging from $x/L = 0.2$ to $x/L = 0.6$. The cause of such an inconsistency may lie once again with the geometrical effects. For a given x/L , shock reflection and curvature losses will be more of a problem with a long slender nozzle than with a short stubby one. Thus, the ratio of nozzle length to exit diameter, L/D , appears to be a possible correlating parameter. Figure 19C shows that such a correlation does exist, with the optimum location moving downstream as L/D increases. Of course, the optimum x/L will vary somewhat for a given nozzle, depending on the various injection parameters, and thus only the general trend can be indicated. Also, in some cases, an actual optimum was not reached, but was either upstream or downstream of the range tested. This is indicated by an arrow in Figure 19C.

4. Injection Angle

Experimental data indicate that increased performance can be gained by injecting the liquid upstream against the flow of the main stream, as can be seen in Figure 20. One of the main effects of this upstream injection angle is an increase in the size of the separation region upstream of the injector. Actual pressure distributions measured at JPL⁴⁰ show that separation was initiated more than twice the distance upstream of the injector when the injection angle was increased from 0° to 40° (measured with respect to the plane normal to the nozzle center line, with upstream values positive). The pressures downstream of the injector were found to be slightly higher and spread more circumferentially with the 40° angle.

III, B, Significant Parameters (cont.)

The larger separation region with an upstream injection angle can be attributed to a greater penetration with respect to the nozzle wall, as well as a slight upstream shift in the actual physical obstruction. The higher relative velocities between injectant and primary flow near the injector, and longer stay time for the injectant within the nozzle, promote atomization, vaporization, mixing, and reaction, which increase the vapor body size and thus account for the larger downstream pressure area.

For cases where the shock-reflection effects predominate, (i.e. high flow rates and locations near the throat), the curvature losses with the larger upstream angles will be greater, thus reversing the usual trend. This situation is illustrated in Figure 21, which shows a 0° injection angle to be superior to a 30° angle for $x/L = 0.2$, but the 30° angle to be better farther downstream.^{33, 34} Also, the effect of flow rate is evident since the crossing of the 0° and 30° performance curves occurs farther downstream at the higher flow rates.

5. Injector Configuration

The multiport injector usually produces higher side specific impulses than a single port due to the greater spread of the disturbance area. Also, by distributing the injectant, the intermediate processes of atomization, vaporization, mixing and reaction are greatly enhanced, so that a multiport injector would definitely be recommended for a reactive liquid. The only port arrangement that has proved successful is a circumferential spacing at the same axial coordinate. Therefore, it is necessary to consider two additional variables with multi-port injectors- the spacing between ports and the number of ports.

Figure 22C shows that there is an optimum spacing for a given port size and number of ports. When the ports are too close together, mutual interference occurs between the disturbances generated from each port, thereby,

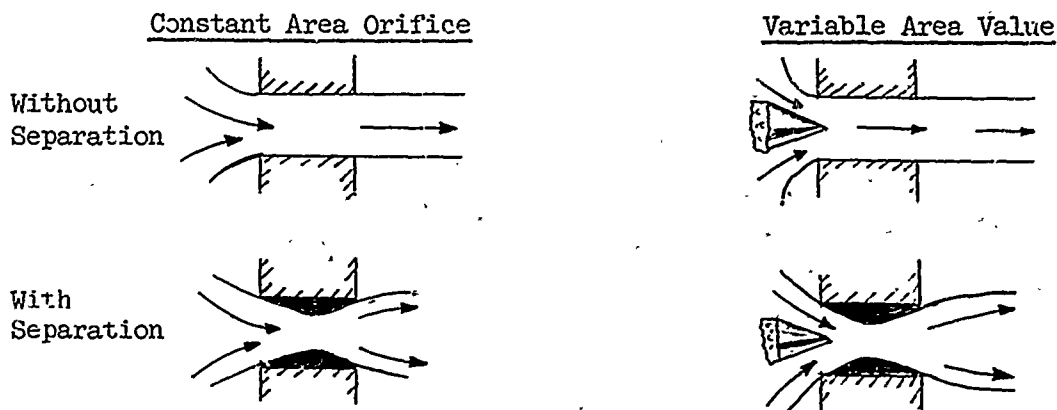
III, B, Significant Parameters (cont.)

reducing the effectiveness of the interaction process. If the ports are too far apart, some of the primary flow may go between the ports essentially unaffected, and the greater spread of the disturbance will once again bring the curvature losses into effect.

Available data indicate that increasing the number of ports has a much greater effect on reactive liquids than on inert injectants. This can be attributed to the better mixing and more complete chemical reaction that results from the greater dispersion of the injectant. Figure 23C shows the increase in the performance of a reactive liquid as the number of ports is increased. However, since the curvature losses are also increasing as the total spread of the ports increases, a point is finally reached where performance will drop if additional ports are added.

The best combination of port spacing and number of ports will depend strongly on the particular injectant, and will also vary with certain injection parameters, particularly injector location.

In discussing the injector, one factor that should be mentioned is the shape and solidity of the liquid jet as it enters the nozzle. This factor will greatly influence the penetration of the jet, as well as the atomization process to a lesser extent. Lockheed⁴³ stated that for both a constant area orifice and variable area valve, the liquid stream may separate from the flow passage walls, changing a solid stream to a spraylike jet, as shown below.



III, B, Significant Parameters (cont.)

This separation is promoted by a short flow passage, a high flow rate, or a low back pressure, and will greatly depend on the shape of the passage. In tests with a constant area orifice at Lockheed, as the injection pressure was increased, a discontinuity developed in the flow rate because of the onset of separation. Such a phenomenon was also noticed at UTC for a variable area valve, and could explain some of the irregularity of liquid injection data.

This separation of the liquid stream causes a decrease in side force since the jet penetration is drastically reduced. This effect appears to dominate over the better atomization, which would improve performance. A good example of the separation effect was the loss in performance that occurred with the Minuteman LIITVC system when the shape of the pintle in the variable-area valve was changed to give better flow control. Bench tests showed that the new valve produced a definite spray pattern, in contrast to a solid stream from the old valve.

It thus appears that the performance of any LIITVC system can be directly affected by the flow characteristics of the liquid stream, and the evidence to date indicates a solid rod-like flow to be best.

6. Motor Parameters

Performance of identical injection systems may still vary from one motor to another, making it necessary to determine the effect of certain motor parameters on TVC performance. These parameters can be grouped as: chamber conditions, propellant properties, and nozzle size and shape.

The performance of inert liquids has been found to be quite sensitive to chamber pressure, as was indicated in Figure 15C, but with some reactive injectants, little effect was noticed.³⁰ A good example of the larger variation in performance that can be experienced with inert injectants as the chamber pressure changes is shown in Figure 24, where Freon 114B₂ was injected at a constant flow rate during motor tail-off.³⁵ As the chamber pressure dropped

III, B, Significant Parameters (cont.)

from 450 to 250 psia, the side-force ratio increased by a factor of 3 and the injectant specific impulse by a factor of 2. At this point, flow separation occurred at the nozzle exit, and then moved upstream into the nozzle as the chamber pressure further decreased. This separation caused a sharp drop in performance as the effective nozzle wall area covered by the pressure disturbance was reduced.

The increase in performance with a decrease in chamber pressure can most likely be attributed to greater penetration of the liquid jet, increased vaporization, and greater expansion of vapor, resulting in greater initial flow deflection and higher downstream pressure differences. Since the inert liquids appear to be more dependent on chamber pressure than certain reactive injectants, the vaporization effects must be the dominant ones.

Higher chamber temperatures would be expected to increase the performance of all liquid injectants, since both the vaporization and chemical reaction processes are temperature dependent to a large extent. Reactive injectants will, in addition, be strongly dependent on the propellant composition. For instance, a propellant producing large amounts of H_2 and CO will contribute greatly to the effectiveness of an oxidizer-type injectant.

Size and shape of the nozzle is an important factor to be considered since the geometrical effects play such a large role in the side force production. The dependence of the optimum injector location on the nozzle L/D has already been discussed.

Another significant parameter is the nozzle expansion ratio. Figure 25 compares the performance at various injector locations of a 30:1 contoured nozzle with another nozzle having the same contour, but cut off at a 12:1 expansion ratio.³⁷ At a given location (ϵ_1), the nozzle with the greater expansion ratio will generally produce the greater side force because of the greater length from injector to exit, and thus greater available wall area for the

III, B, Significant Parameters (cont.)

pressure disturbance. However, the larger nozzle will also be more subject to shock reflection and curvature losses, which would make the shorter nozzle more effective at locations close to the throat. At the same relative location (x/L), the performance of the smaller expansion ratio nozzle will be greater because of smaller Mach numbers, and thus larger pressure differences and steeper shocks. Both of these trends are substantiated by the data plotted in Figure 25.

The actual nozzle contour also appears to have a substantial effect on TVC performance. Figure 26C shows that at the optimum injector location, considerably higher injectant specific impulses for both inert and reactive liquids were produced in a contoured nozzle as compared with conical nozzles. A possible reason for this may be the greater primary flow mass concentration near the wall in a contoured nozzle, which would allow a greater effective flow deflection by an obstruction on the wall. It may be possible to actually optimize a nozzle contour for TVC performance and with such an objective, NESCO²⁹ has worked a great deal with an adverse pressure gradient nozzle. However, there is usually a loss in axial performance associated with such a change in contour, which in most cases cannot be tolerated.

C. AXIAL THRUST AUGMENTATION

A favorable by-product of the secondary injection concept is an increase in axial thrust during injection. Because of the diverging shape of the nozzle exit cone, the pressure force acting normal to the nozzle wall also has an axial component acting in the same direction as the thrust. This component is primarily a function of the nozzle divergence angle, α , and does not depend upon the azimuthal coordinate, θ , as does the side force. Thus, the axial thrust augmentation will continue to increase as the pressure disturbance spreads in the circumferential direction, and will be substantial when the shock reflects off the opposite nozzle wall. Also, the closer the injector is to the throat, the greater the projected wall area in the cross-sectional plane, so the greater the thrust augmentation.

III, C, Axial Thrust Augmentation (cont)

The momentum of the injected liquid may also have an axial component, depending on the injection angle. However, since the momentum is usually less than 10% of the side force, this component would not be significant in most cases.

Figures 27 and 28 show some thrust augmentation data for Minuteman subscale nozzles^{33,34,35, and 36} and illustrate the effects of injectant flow rate, injector location, and angle of injection. As would be expected, the greater pressure differences and larger disturbance area associated with greater flow rates cause a corresponding increase in axial thrust augmentation. Unlike the side force, however, at the locations close to the throat, the thrust increment continues to increase at the higher flow rates, instead of leveling off and actually decreasing because of curvature effects. Also, there is no optimum injector location as with the side force, so that a location closer to the throat always results in greater thrust augmentation. It can be seen in Figure 28 that upstream injection angles produced greater thrust increments. This indicates that the greater pressure forces more than compensated for the negative momentum axial components associated with the upstream angles. However, it is possible that at locations near the exit this relation may be reversed and a negative thrust increment produced.

This thrust augmentation characteristic of secondary injection is an important point to be considered when comparing this system with mechanical methods of TVC for which there is usually a loss in axial thrust.

D. SCALE EFFECTS AND DYNAMIC RESPONSE

A question that has yet to be fully answered is whether there is a difference in the IVC performance between two different size motors with geometrically similar nozzles and TVC system parameters. At first glance, it would seem that such a difference would exist since such phenomena as penetration, atomization, boundary layer separation, and chemical reaction would not appear to be directly scalable. However, experimental data from Aerojet, with Minuteman motors, and

III, D, Scale Effects and Dynamic Response (cont.)

at Lockheed^{31,32} has failed to indicate any definite scale effects. Such effects may still exist though for different parameter ranges, and, on the basis of the above phenomena, a slight loss in performance with the larger nozzles might be expected. Additional experimental verification is needed to settle this particular question.

As compared with mechanical TVC systems, secondary injection has an extremely fast response, or a short time lag between command and application of the control force. Because of test-stand inadequacies, actual measurement of this response has been very difficult. However, a technique was developed at Aerojet⁴⁴, using exit-cone pressure-tap readings instead of load-cell measurements. In tests with a sinusoidal-injectant flow-rate variation, it was found that the phase lag between the side force and the flow rate, excluding valve dynamics, was negligible up to 20 cps. Also, the side force amplitude ratio varied little from unity for this same range.

It is hoped that the data compiled in this section on performance characteristics will lead to a better understanding of the liquid-injection process, and that the parameter effects illustrated may be useful for preliminary design purposes until an adequate analytical or empirical performance prediction method is developed.

IV ANALYTICAL APPROACHES

A. SUMMARY OF PREVIOUS WORK

Although the liquid injection concept has been investigated for a number of years, an analytical model for adequately predicting the performance of any LIJVC system has not been found. This is not surprising when one considers the complicated processes of liquid-jet penetration, atomization, vaporization, mixing, and reaction that must be analyzed, in addition to the extremely complex three-dimensional flow field. However, from the models that have been proposed, a greater insight into the various problem areas has been gained, which, along with the accumulation of additional experimental data, leads to the formulation of more realistic assumptions in future approaches.

Early in 1960, the first liquid-injection analytical study was begun by NESCO (National Engineering Science Company) under contract to Aerojet.¹⁷ The model proposed in this study is illustrated in Figure 29. The liquid was assumed to flow along the nozzle wall, instead of penetrating into the main stream, and to form a uniform distribution of mass sources due to vaporization. Linearized theory for supersonic aerodynamics was used to calculate the side force produced by the resulting wedge-shaped vapor body. This model produced fair agreement with experimental data for low injectant mass flow rates, when penetration was relatively small, but the correlation was quite poor through the remainder of the mass flow range.

A much more sophisticated approach to the liquid vaporization process was presented by NESCO in 1961 under a subsequent Aerojet contract.¹⁸ In this model, shown in Figure 30, the intermediate processes of atomization and droplet vaporization were included, which, along with the droplet trajectories, determined the resulting vapor "body". The liquid jet was assumed to break up immediately on entering the nozzle and a mean droplet size was determined from the empirical relations of Ingebo and Foster,¹² based on free-stream conditions behind a normal shock just upstream of the injector. The droplet vaporization rate was taken from Penner,¹⁹

IV, A, Summary of Previous Work (cont.)

and by considering the drag on the mean size droplets due to the primary flow, the trajectory of these droplets was computed. The free-stream conditions governing the droplet motion and vaporization were taken as those existing at the injector before injection, and were assumed to be unaffected by the presence of the droplets and vapor. The injected liquid was thus distributed within the nozzle as a continuous line of mean size droplets along the calculated trajectory. The vapor from this line source was assumed to form a blunt-nosed half-body of revolution lying along the nozzle wall between the injector and exit plane, and acting as a solid physical obstacle.

The separated region upstream of the injector was assumed to have the shape of a half-cone tangent to the nose of the vapor body. The equivalent obstacle was then a sharp-nosed body of revolution, with the axis of symmetry being the nozzle element passing through the center of the injector. The resulting shock and flow field were assumed to be symmetric about this same axis, and were calculated by a simple shock expansion method for uniform and constant free-stream conditions. The side force was then calculated by integrating the wall pressures behind the shock and adding the momentum component of the liquid jet. The effects of nozzle curvature in the cross-sectional plane were not included, although the nozzle divergence angle was taken into consideration.

The side forces calculated in this manner were generally 30 to 50% below experimental values, but this analysis contributed a great deal to the state of the art by indicating the basic processes that need be considered, and by representing the actual flow field within the nozzle with an equivalent simplified model.

This same model was later improved at JPL²⁰ by including a more realistic vaporization rate and a relatively sophisticated droplet drag coefficient. Also, the separation zone was modified to more closely represent the observed double-shock pattern as shown in Figure 2a. Calculated results were compared with experimental values for only two cases, being 4% high in one case, and 20% high in the other.

IV, A, Summary of Previous Work (cont.)

Broadwell²¹ in 1962 proposed an entirely different model for secondary-injection TVC, applicable to both liquid and gas injectants. This model is based on the blast-wave analogy, which transforms results derived from one-dimensional, unsteady flow to two-dimensional, steady flow. Thus empirical relations found for an expanding cylindrical shock wave produced by the explosion of a line charge are applied to the problem of determining the steady-state axisymmetric shock about a blunt body of revolution. For a solid body, the drag forces on the body are equated to the energy released by the original line charge to determine the size and shape of the shock. For secondary injection, the injectant momentum, along with energy either taken from the free stream to vaporize the liquid, or added to the free stream due to a chemical reaction, must also be included.

Broadwell considered only the first-order blast-wave solution, which is limited to very high free-stream Mach numbers. A second-order solution has been used by Dahm⁵⁰ at Vidya in an effort to improve the treatment.

Unfortunately, the blast-wave analogy is strictly applicable only for constant free-stream conditions in front of the shock. Also, since vaporization is assumed to take place immediately as the injectant enters the nozzle, the effects of the parameters which influence the atomization and vaporization processes (i.e., port diameter, angle of injection, and injectant properties), as well as the effects of boundary layer separation and nozzle wall curvature, are not included. Consequently, the calculated results agree well with data at the low injectant flow rates, but the analysis does not predict the decrease in side specific impulse with increasing flow rate, nor the correct variation of side force with injector location.

At Aerojet, the interest in a theoretical liquid-injection model continued after the initial investigations by NESCO¹⁸ were completed. Using the same general approach as NESCO, modifications were first made to the vapor-body calculations to improve the portions dealing with the vaporization rates and drag coefficients. These modifications were very similar to those later published by JPL.²⁰

IV, A, Summary of Previous Work (cont.)

Also, a method was sought for simplifying the tedious, time-consuming flow field calculations included in the NESCO report. A dimensional analysis approach was first taken in which the side force was related to the size of the vapor body and several nozzle and motor parameters. With the vapor body assumed to form a half-body of revolution for a single-port injector, the vapor body radius at the nozzle exit was taken as the significant body dimension. This radius was a function of such variables as the injectant properties, port diameter, angle of injection, free-stream properties, and nozzle-wall length between the injector and the exit plane, and was calculated with a computer program similar to the one described in Appendix A. Using dimensional analysis, the following expression was derived for a single-port injector and nonreactive injectant.²²

$$\frac{F_s'}{F_a} = 0.67 \left(\frac{\epsilon_T}{\epsilon_i} \right)^{\frac{1}{2}} \left(\frac{\cos \alpha}{C_F} \right) \left(\frac{R_v}{R_T} \right)^2 \quad (1)$$

where

- F_s' = the induced side force, or the side force caused by interference only (not including the injectant momentum);
- F_a = axial thrust;
- ϵ_T = nozzle expansion ratio;
- ϵ_i = expansion ratio at the injector;
- α = nozzle divergence angle;
- C_F = nozzle thrust coefficient;
- R_v = vapor body radius at nozzle exit;
- R_T = nozzle radius at exit.

The total side force was found by adding the momentum of the injectant entering the nozzle, F_m , to the interference force, F_s' . The momentum can be written as

$$F_m = \left(\frac{\dot{W}_s V_L}{g} + P_i A_i \right) \cos \varphi \quad (2)$$

IV, A, Summary of Previous Work (cont.)

where \dot{W}_s = the injectant mass flow rate;
 V_L = the velocity of the injectant entering the nozzle;
 ϕ = the angle of injection with respect to the normal to the nozzle center line;
 P_i = the injectant pressure at the port exit;
 A_i = the port area.

The side forces calculated in this manner correlated fairly well with a wide range of experimental data as shown in Figure 31. This correlation was encouraging since it indicated the ability of the vapor-body model to predict the relative changes produced by a variation in injection or nozzle parameters.

This same approach was used in Reference 23 to include the effects of reactive injectants and multiport injectors. The vapor body radius, however, was calculated in a different manner. An initial mixture of vapor and free stream gases was determined by the penetration of the liquid jet, and the volume increase caused by chemical reaction was calculated by assuming the mixture to attain thermochemical equilibrium. This model, therefore, also includes the effect of the propellant properties, as well as additional injectant properties, and the circumferential extent of the injector. Figure 32C shows that the correlation with experimental data obtained with this model is similar to that found with the previous model, which was applicable to a single port and nonreactive injectant. The results from both models, however, were not sufficiently accurate for design purposes, especially in the high mass flow range and for injector locations far from the exit. As a consequence, continued efforts at Aerojet have been directed towards the development of an improved analytical model for better parametric correlations.

IV, Analytical Approaches (cont.)

B. CURRENT AEROJET PRELIMINARY MODEL

1. Description

Because of the complexity of the interference pattern created by the injection of a secondary fluid into a nozzle, a detailed flow-field solution appears to be the only way to properly evaluate the effects of the large number of significant parameters over the effective range of each. Such a solution would have to be more accurate and less cumbersome than the ones proposed in References 18 and 20.

With this in mind, a method of characteristics computer program was developed for calculating a two-dimensional (plane) or axisymmetric curved shock wave and the rotational flow behind the shock. This program, which is discussed in more detail in Appendix B, requires, as input, initial conditions along a start line in the undisturbed region upstream of the shock, and the shape of the solid body producing the shock. If the shock is detached, an additional start line must be specified in the supersonic region between the shock and body, with the subsonic flow upstream of that point calculated independently. The start line in the undisturbed region enables the program to handle nonuniform free-stream conditions before the shock, and thus the actual initial conditions existing in a nozzle can be taken into account.

If the shock strength does vary along the shock, the entropy rise, and thus total pressure drop, across the shock will also vary. Therefore, the equations for rotational flow, in which the entropy is constant along a streamline, but may vary from streamline to streamline, must be used in calculating the flow field between the shock and body. The general logic used in propagating the solution is described in Appendix B.

IV, E, Current Aerojet Preliminary Model (cont.)

The present preliminary analytical model for liquid-injection EVC consists primarily of three parts:

- a. vapor body calculation;
- b. flow field solution;
- c. pressure integration over nozzle walls.

The vapor-body calculation is based on the approach previously described in connection with NESCO's model,¹⁸ but includes the improvements in vaporization rate and drag coefficients described in Reference 22. An additional modification has been made to include variation in free-stream properties in the axial direction. To briefly review this approach, a mean-size droplet is found from empirical relations, and the trajectory of this droplet is calculated by considering the drag forces acting on the droplet because of the free stream. The presence of the droplets is assumed to have no effect on the free-stream properties used to calculate the drag forces. As the droplets travel along their trajectory, vaporization occurs because of the high free-stream temperatures. The resulting vapor body is found by considering the injectant distributed along the mean size droplet trajectory to act as a line source, and by assuming the vapor to form a half body of revolution. This entire procedure, described in more detail in Appendix A along with the derivation of the significant equations, has been incorporated into a computer program on the GE 225. In Figure 33, calculated vapor bodies are compared with erosion patterns formed by injection of Freon 114B₂ into a Minuteman nozzle during a hot firing. If the actual vapor body is axisymmetric, these comparisons indicate its size and shape are represented fairly well by the analytical model.

Before the vapor-body shape can be input to the flow field solution, it must be modified to include the separated region upstream of the port. For the sake of simplicity in this preliminary model, this region was first assumed to be conical and tangent to the nose of the vapor body as in Reference 18. Thus

IV, B, Current Aerojet Preliminary Model (cont.)

only a single attached shock results, as shown in Figure 3a, and the entire flow field can be calculated with the method of characteristics program previously described. Provision can be made later to include the general two shock system shown in Figure 2a, or the limiting bow shock at the high mass flows as shown in Figure 3b.

To find the vertex angle of this conical separation region, the relation derived by Mager²⁴ was used in which the plateau pressure rise associated with the separation of a turbulent boundary layer, P_f/P_∞ , is given as a function of the free-stream Mach number, M_∞ , the flow deflection angle, δ , and the ratio of specific heats, γ . The resulting equation is

$$\frac{P_f}{P_\infty} = \left[1 + \frac{(1-K)}{2} \frac{\gamma M_\infty^2}{1 + \left(\frac{\gamma-1}{2}\right) M_\infty^2} \right] \left[1 + 0.328 \frac{K \gamma M_\infty^2 \delta}{1 + K \left(\frac{\gamma-1}{2}\right) M_\infty^2} \right] \quad (3)$$

where K is the ratio of the square of the Mach number at the separation point to M_∞^2 . Experimental data indicates this ratio to be approximately 0.55.

For given values of M_∞ and γ , the pressure rise across a conical shock can be found as a function of cone angle. By satisfying this additional relation along with the above equation, the resulting value of P_f/P_∞ and δ can be found. Figure 34 shows the variation of these variables with M_∞ for $\gamma = 1.2$. The value of δ determines the size of the separation region since it is assumed to be tangent to the vapor body.

To utilize the method of characteristics flow field solution, the assumption is made that the shock and flow behind it is axisymmetric with respect to the nozzle element passing through the center of the injector. This is probably the weakest point in the present model, since the actual flow is three-dimensional. However, it was felt that the axisymmetric solution should

IV, B, Current Aerojet Preliminary Model (cont.)

represent the actual flow to a fairly good degree, and could be corrected for the major three-dimensional effects. A typical calculated vapor body, separated region, shock, and flow-field network is shown in Figure 35.

The last step in finding the side force is the integration of the calculated pressures over the nozzle walls. By superimposing the given nozzle shape upon the axisymmetric flow-field solution, the shock and nodal points in the characteristic solution can be located along the nozzle wall. Figure 36 shows a typical intersection of a calculated axisymmetric shock wave with a nozzle wall. To calculate the side force, these points are then projected into a plane parallel to the nozzle center line and perpendicular to the plane formed by the nozzle center line and the shock axis of symmetry. Thus, when the calculated pressures are integrated in this plane, the effects of the nozzle divergence angle and wall curvature in the cross-sectional plane are included. Also, provision has been made for handling the case of a shock intersection with the nozzle wall above the center line, which produces a negative force component.

The axial thrust augmentation is found in the same manner, except the solution points are projected into a plane normal to the nozzle center line. In this case, no reversal of force occurs when the shock crosses over the center line.

An additional item calculated is the center of force, or the effective point of application for the induced side force, F_s' . This axial distance, x_c , (using the nozzle throat plane as the reference plane) can be found from the following expression:

$$x_c = \frac{\int_0^{A_s} x (P - P_\infty) dA}{\int_0^{A_s} (P - P_\infty) dA} = \frac{\int_0^{A_s} x (P - P_\infty) dA}{F_s'} \quad (4)$$

IV, B, Current Aerojet Preliminary Model (cont.)

- A_s = the nozzle wall area behind the shock in the plane perpendicular to the side force;
- x = the axial distance of dA from the reference plane;
- P = the average static pressure acting upon dA during injection;
- P_{∞} = the average static pressure that would act on dA with no injection.

This pressure integration routine has been combined with the flow field solution into a single computer program, which takes less than 1 minute per run on the IBM 7094. The calculation of the vapor body and separation region will also be included in this one program when the final form of the body shape has been decided.

2. Results

To evaluate the performance prediction capability of this model, side forces were calculated for a number of different motors encompassing a wide range of injection and nozzle parameters. Axial thrusts for these motors varied from 1,000 to 100,000 lb, nozzle expansion ratios from 6.64:1 to 24.8:1, injectant mass flows for Freon 113 and 114B₂ from 2% to 22% of the primary flow, and injector locations at expansion ratios from 3:1 to 12.5:1. When these calculated results were compared with the measured data for these motors, it was found that the model predicted side forces that were generally 40 to 50% too low. However, the ratio of calculated to measured side forces did not appear affected by the wide parameter variation.

The main reason for these low values can be found by comparing the calculated and measured pressure distributions. Figure 37 shows that the theoretical axial pressure distributions along the vapor body itself agree fairly well with the measured values, but the circumferential spread of the calculated disturbance is much less than indicated by experimental data. This latter result

IV, B, Current Aerojet Preliminary Model (cont.)

is more evident in Figure 38, where the traces of both the theoretical and experimental shock waves along the nozzle wall are shown. The largest deviation between the two shock patterns occurs in the separation region, as might be expected, with the measured disturbance hyperbolic shaped, while the calculated shock and separation form a vortex of a triangle. The assumed conical shape for the separation region is thus obviously incorrect. Farther downstream, the difference might be attributed to three-dimensional effects and/or too small a calculated vapor body. In addition, boundary layer separation may also occur in the area downstream of the port due to the impingement of the shock on the nozzle wall. This would tend to spread the disturbance farther upstream from the shock itself. Since relatively high pressures occur in this additional area not covered by the theoretical shock, the difference in area causes a substantial difference in side force. This preliminary model has thus indicated definite areas that must be improved before the final form of the model is determined.

V. RECOMMENDATIONS FOR FUTURE WORK

Although the results from the preliminary model are not satisfactory at present, the consistency of the relation between the calculated and measured side forces is very encouraging. This model thus not only forms a firm basis for future work, but also indicates the specific areas needing improvement and the definite directions to go in each area. It is estimated that the model in its present form is approximately 70% complete. To bring it to full completion, the following tasks will be undertaken:

1. a better representation of the separation region;
2. corrections to the flow field solution for three-dimensional effects;
3. more realistic vapor-body calculations.

These tasks will depend greatly on basic experimental data in the form of pressure distributions and visual evidence, such as shadowgraphs and/or schlieren photographs of the flow. A current IR&D program for gas-injection TVC has been designed to provide specific information of this kind, which will be directly applicable to the first two tasks.

According to data now available, the separation region apparently spreads out along the wall much more than would be indicated by a simple half-conical shape. Thus, the flow over this region is three-dimensional, and cannot be included in the axisymmetric flow field solution. Therefore, it will be necessary to calculate this region separately, possibly by semiempirical means. In addition, in the higher injectant flow ranges, when a strong shock is produced, the calculation of this shock and the subsonic flow behind it must also be included. If this subsonic region is relatively small, a simplified approach such as the method of Moeckel²⁵ might be adequate for defining the initial conditions for the supersonic solution. If a more sophisticated subsonic solution is required, the method of integral relations²⁶ has proven successful for calculating detached shocks with the accompanying subsonic flow, and can be combined with the method of characteristics to give the entire flow field.²⁷

Recommendations for Future Work (cont.)

The two major three-dimensional effects for which the axisymmetric flow-field solution should be corrected are the initial conditions in the nozzle before the shock, which are not symmetric with respect to the shock axis, and the nozzle wall curvature in the cross-sectional plane. In this particular area, the data obtained from the aforementioned gas-injection program will be quite valuable since a given set of injection conditions will be kept constant for injection:

1. through a flat plate into a uniform free-stream;
2. into a two-dimensional (plane) nozzle;
3. into an axisymmetric nozzle.

By comparing the shock shapes and pressure distributions obtained for each case, the three-dimensional effects will be determined.

The ultimate answer to the problems in this area is the use of the three-dimensional method of characteristics in the flow-field solution. The logic involved in programming such a solution is much more involved in comparison with the two-dimensional or axisymmetric method of characteristics, but the approach presented by Moretti²⁸ has been successfully programed. Since the three-dimensional subsonic solution can also be included, as shown in Reference 27, the entire flow field about the body with its attached three-dimensional separation region could once again be calculated in one step. Also, the vapor body would no longer be restricted to a half-body of revolution, and could thus include the effects of liquid-jet penetration and multiport injectors. Because of the great value of a three-dimensional method of characteristics program, not only for a secondary injection model, but for many other supersonic flow problems as well, work has been initiated here for the development of such a program.

The vapor body calculation, the heart of the liquid injection model, has one big weakness--the use of the free-stream conditions outside the body to determine droplet trajectories, vaporization, etc. In reality, the droplets are traveling in a medium which is a mixture of vapor and free-stream gases. In a model proposed by

V, Recommendations for Future Work (cont.)

Mayer,²⁹ the droplet behavior is based on the properties of such a mixture, and the resulting droplet velocities are much lower than those calculated by the present method. For a given amount of vapor generated, a larger vapor body will thus be produced, resulting in a greater side force. The present vapor body calculation will therefore be modified to include this more realistic treatment of the interaction between the liquid droplets, vapor, and free-stream gases.

Once satisfactory results have been obtained for injection of an inert liquid through a single port, the model will be expanded to include reactive liquids and multi-port injectors. The chemical reaction between the injectant and free stream can probably best be handled by thermochemical calculations similar to those described in Reference 23. With the three-dimensional method of characteristics, the vapor-body shape can be made dependent on the number and spread of the injection ports, as well as the liquid-jet penetration.

The tasks proposed here, with the exception of the three-dimensional method of characteristics, will not amount to major efforts, but, for the most part, must await the forthcoming experimental data. When the three-dimensional characteristic solution has been completed, and each portion of the model satisfactorily checked with experimental data, the entire model will be combined into a single computer program.

VI. CONCLUSIONS

Liquid injection may now be considered a proven reliable method of thrust-vector control as a result of its performance on the Polaris and Minuteman test flights. Although LIIVC appears best suited for upper-stage applications, static test results for the Titan IIIC 120-in.-dia solid booster have shown the performance of a system using N_2O_4 as the injectant to be entirely adequate. Also, because of its fast response, LIIVC has been designated for the upcoming Sprint anti-missile missile. Therefore, this type of thrust-vector control will most likely be used extensively in future designs, with performance increases coming as the technology grows. Although greater performance can be attained with gas injectants, it will be some time yet before a system with a hot-gas valve will reach the stage of reliability currently associated with liquid-injection systems.

Despite the fact that LIIVC systems have proved successful in many applications, there is still relatively little known about the complex flow interaction which produces the side force. The present system designs have been reached only after extensive and costly testing, and still may not be completely optimum. There is thus a great need for a method of predicting the performance of any LIIVC system, which can be used in lieu of many tests to determine more realistic preliminary designs. Such a method would be used for:

1. evaluating the performance of a given system;
2. optimizing system parameters for a given application;
3. extrapolating subscale test data to full-scale designs;
4. sizing system components.

The simplified analytical models and empirical methods that have been attempted to date do not include sufficient detail for design purposes. Only a model which actually represents the flow within the nozzle during injection can include the first order effects of all parameters, while contributing to a greater knowledge and understanding of the associated phenomena.

VI, Conclusions (cont.)

It was towards this objective that the development of the model described in this report was initiated. When completed, this model will have the additional advantage of providing detailed pressure distributions for nozzle stressing, heat-transfer studies, and injector design. Also, individual portions of the solution can be easily modified as additional information becomes available.

In the very near future, when the experimental results from the current gas-injection cold-flow test program are available, this model should be completed for inert injectants and single port injectors. Additional modifications to handle reactive liquids and multiport injectors do not appear to be major undertakings. The final objective is a single computer program that will include any injectant, gas or liquid, for any kind of injector, in any type of nozzle.

NOMENCLATURE

A_i	-	Injector port diameter
A_s	-	Nozzle wall area behind shock projected into plane perpendicular to side force
C_D	-	Droplet drag coefficient
$(C_p)_v$	-	Vapor specific heat
C_F	-	Axial thrust coefficients
C_w	-	Injector port discharge coefficient
d_i	-	Injector port diameter
D_o	-	Initial mean droplet diameter
D	-	Nozzle exit diameter
L^*	-	Nozzle throat diameter
F_A	-	Axial thrust
$(F_A)_o$	-	Axial thrust without injection
F_D	-	Drag force on droplets
F_M	-	Component of injectant momentum contributing to side force
F_s	-	Side force
F_s'	-	Side force excluding injectant momentum
I_s	-	Motor axial specific impulse
$(I_s)_s$	-	Injectant side specific impulse
K	-	Ratio of Mach number at separation point, squared, to free-stream Mach number, squared
L	-	Nozzle length
L_v	-	Injectant latent heat of vaporization

NOMENCLATURE (cont.)

m	-	Mass of vapor generated per droplet
M	-	Mach number
N	-	Number of mean-size droplets entering nozzle per unit time
n	-	Normal to streamline
p	-	Static pressure
p_c	-	Chamber pressure
p_f	-	Plateau pressure in separation region
p_{inj}	-	Injection pressure
p_t	-	Total pressure
Pr	-	Prandtl number, $(c_p \mu / \lambda)$
r	-	Radial coordinate
r_d	-	Droplet radius
r_o	-	Initial mean droplet radius
R	-	Gas constant
R_T	-	Nozzle exit radius
R_v	-	Vapor body radius
Re	-	Reynolds number $(\rho V d / \mu)$
s	-	Entropy
t	-	Time
T_c	-	Chamber temperature
T_L	-	Injectant boiling temperature
u	-	Axial velocity component
v	-	Radial velocity component

NOMENCLATURE (cont.)

\vec{V}	- Total velocity
\vec{V}_d	- Total droplet velocity
\vec{V}_L	- Initial injectant velocity
\vec{V}_r	- Relative velocity
w_A	- Motor propellant mass flow rate
w_S	- Injectant mass flow rate
We	- Weber number
x	- Axial coordinate
x_c	- Distance of center of force from nozzle throat
(x,y,z)	- Cartesian coordinates
(r,θ,x)	- Cylindrical coordinates
α	- Nozzle wall angle (Mach angle in Appendix B)
β	- Vaporization rate
β ₀	- Vaporization rate in a stagnant atmosphere
γ	- Ratio of specific heats
ζ	- Flow deflection angle across shock
ε	- Shock angle
ε _i	- Nozzle expansion ratio at injector
ε _T	- Nozzle expansion ratio at exit
θ	- Azimuthal coordinate (Flow angle in Appendix B)
λ _v	- Vapor thermal conductivity
μ	- Absolute viscosity
ν	- Kinematic viscosity
ξ	- Distance along droplet trajectory

NOMENCLATURE (cont.)

- ρ - Density
- σ - Surface tension
- Φ - Injection angle

Superscripts

- (\quad) - Denotes average quantities in finite difference solution

Subscripts

- A, A₁, - Denotes points in shock point solution
- A₂, B,
- B₁, B₂,
- C, D, E,
- F
- d - Pertains to droplets
- i - Denotes conditions at injector port
- I - Pertains to left-running characteristic
- J - Pertains to right-running characteristic
- L - Pertains to the injectant in liquid form
- n - Denotes point to be computed in finite difference solution
- n-1 - Denotes point previously computed in finite difference solution
- N - Denotes conditions behind normal shock
- v - Pertains to injectant vapor
- ∞ - Denotes free-stream conditions
- o - Denotes initial conditions
- 1,2,3, - Denote points in internal point and boundary point solutions
- 4

REFERENCES

1. Hausman, G. F., Thrust Axis Control of Supersonic Nozzles by Airjet Snock Interference, United Aircraft Corporation, Research Department, Report R-63143-24, May 1952.
2. Schulmeister, M., Static Evaluation Tests of an Oblique Shock Wave System for Rocket Exhaust Deflections, Naval Air Rocket Test Station, Final Report 77, December 1955.
3. Lingen, A., Jet Induced Thrust Vector Control Applied to Nozzles Having Large Expansion Ratios, United Aircraft Corporation, Research Department, Report R-0937-33, March 1957.
4. Bankston, L. T., and Larsen, H. M., Thrust Vectoring Experiments With Gas Injection, Naval Ordnance Test Station, NAVORD 6548, NOTS 2247, May 1959.
5. Green, C. J. and McCullough, F., Jr., Liquid Injection Thrust Vector Control, Naval Ordnance Test Station, NAVWEPS Report 7744, NOTS TP 2711, June 1961.
6. Firing Report for Motor 44SS-1 Liquid-Injection With Thrust Vector Control, Aerojet-General Corporation, Report No. 0434-01S13-T5, December 1961.
7. Evaluation of Strontium Perchlorate as Injectant Fluid, Aerojet-General Corporation, SRP:62:5210:L:312, August 1962.
8. Dowdy, Mack W. and Newton, John F., Jr., Investigation of Liquid and Gaseous Secondary Injection Phenomena on a Flat Plate with $M=2.01$ to $M=4.54$, Jet Propulsion Laboratory, Technical Report No. 32-542, December 1963.
9. Dowdy, M.W. and Newton, J.F., Jr., Wind Tunnel Experiments of Freon-12 Secondary Injection, Jet Propulsion Laboratory, Space Programs Summary No. 37-17, Vol. IV, October 1962.
10. Hsia, H. T., Seifert, H. S., and Karamcheti, K., Shocks Induced by Secondary Fluid Injection, Stanford University, Stu SUDAER-167, September 1963.
11. Longwell, J. P., "Combustion of Liquid Fuels," Combustion Processes, High Speed Aerodynamics and Jet Propulsion Series, Volume II, Princeton University Press, 1956.

REFERENCES (cont.)

12. Ingebo, R. D., and Foster, H.H., Drop-Size Distribution for Crosscurrent Breakup of Liquid Jets in Airstreams, NACA TN 4087, October 1957.
13. Bitron, M.D., "Atomization of Liquids by Supersonic Airjets," Industrial and Engineering Chemistry, Vol. 47, January - June 1955.
14. Weiss, M. A. and Worsham, C. H., "Atomization in High Velocity Airstreams," ARS Journal, April 1959.
15. Wilmarth, W. W., The Production of Aerodynamic Forces by Heat Addition on External Surfaces of Aircraft, The Rand Corp., RM-2078, 30 Dec 1957.
16. Chenoweth, D. R., Calculation of Turbulent Mixing with Chemical Reactions, Aerojet-General Corporation, Technical Paper 132 SRP, March 1964.
17. Wu, J. M., Chapkis, R. L., Chenoweth, J. M., and Mager, A., Analytical Study of Thrust Vectoring, National Engineering Science Company, Final Report, Contract No. PO S-409721-OP, 9 November 1960. Also ARS Journal, December 1961.
18. Wu, J. M., Chapkis, R. L., Ai, D. K., and Rao, G. V. R., Polaris Thrust Vector Control Analysis, National Engineering Science Company, Final Report, Contract No. PO S-412707-OP, 31 July 1961.
19. Penner, S. S., "On Maximum Evaporation Rates of Liquid Droplets in Rocket Motors," ARS Journal, March 1953.
20. Sehgal, R., and Wu, J. M., "A Study of Thrust Vector Control by Liquid Injection into Rocket Nozzles," Bulletin of the Interagency Solid Propulsion Meeting, Volume III, July 1963.
21. Broadwell, J. E., An Analysis of the Fluid Mechanics of Secondary Injection for Thrust Vector Control (Revised), Space Technology Laboratories, INC., 6120-7744-MU-000, 15 March 1962. Also AIAA Journal, May 1963.
22. Mockenhaupt, J. D., An Approximate Method for Side Force Calculation, Memo 4710: 1064M, Aerojet-General Corporation, 16 October 1962.
23. Brumby, R. E., An Empirical Method for Determining the Performance of Any Liquid Injection System, Aerojet-General Corporation, Memo SRP-64-5570-M-392, 29 April 1964.
24. Mager, A., "On the Model of the Free, Shock-Separated, Turbulent Boundary Layer," Journal of Aeronautical Sciences, February 1956.
25. Moeckel, W. E., Approximate Method for Predicting Form and Location of Detached Shock Waves Ahead of Plane or Axially Symmetric Bodies, NACA TN 1921, July 1949.

REFERENCES (cont.)

25. Belotserkovskii, O. M., Computation of the Flow Around Axisymmetric Bodies with a Detached Shock, Computation Center, Academy of Sciences, Moscow, 1961.
27. Supersonic Flow About General Three-Dimensional Blunt Bodies, Wright-Patterson AFB, Report No. ASD-TR-61-727, Vol. I, October 1962.
23. Moretti, G., A Technique for Computing Three-Dimensional Steady Inviscid Supersonic Flow, General Applied Science Laboratory, Report TR-172, July 1960.
29. Mayer, E., Houser, B., and Hays, W., Feasibility Studies of Adverse Pressure Gradient Nozzles for Liquid Injection Thrust Vector Control, National Engineering Science Company, Vol. I, Contract No. NORI 17017, November 1962.
30. Grunwald, G. J. and LeCount, R. L., Fluid Injection TVC Research (u), Lockheed Missiles and Space Co., TM 53-42-4, October 1963 (Confidential Report).
31. Grunwald, G. J., Fluid Injection TVC Research (u), Lockheed Missiles and Space Co., TM 55-12-05, October 1964 (Confidential Report).
32. Huizinga, J., Liquid Injection Thrust Vector Control Effectiveness (u), Lockheed Missiles and Space Co., TM 57-11-21, August 1961 (Confidential Report).
33. Final Report, Firing of Second-Stage Minuteman Subscale Engine 37FW-38, Aerojet-General Corporation, SRP:61:5220:L:238, 15 August 1961.
34. Final Report, Firing of Second-Stage Minuteman Subscale Engine 37FW-59, Aerojet-General Corporation, SRP:61:5220:L:282, 22 September 1961.
35. Final Report, Firing of Minuteman Second-Stage Subscale Motor 37FW-57, Aerojet-General Corporation, SRP:62:5210:L:1, 2 April 1962.
36. Final Report Firing of Minuteman Second-Stage Subscale Motor 37FW-60, Aerojet-General Corporation, SRP:62:5210:L:176, 9 May 1962.
37. Magnusson, A. W., and Heirz, C. W., Scale Model Evaluation of the Fluid Injection Concept for Thrust Vector Control, Aerojet-General Corporation, Contract No. LMSD 18-2201, NORI 17017, August 1961.
38. Unpublished Data on 10KS Motor Firings with Liquid Injection Thrust Vector Control Conducted by Polaris Project.
39. Rimington, D. A., Final LITVC Test Report on 52FW-8 (TVC-17) (u) Aerojet-General Corporation, SRP:61:5270:M:1111, 2 January 1964 (Confidential Report).

15987
REFERENCES (cont.)

40. Newton, J. F., Jr., and Spaid, F. W., Experiments on the Interaction of Secondary Injectants and Rocket Exhaust for Thrust Vector Control, Jet Propulsion Laboratory, Technical Report No. 32-203, 12 February 1962.
41. Summary Report of 1OKS-2500 Liquid Evaluation Program, Aerojet-General Corporation, SRP:61:5210:L:308, 20 September 1961.
42. 1OKS Motor Evaluation of Strontium Perchlorate as an Injectant Fluid, Aerojet-General Corporation, SRP:62:5210:L:312, 24 August 1962.
43. Final Report - Sprint Missile Control System Study (u), Lockheed Missiles and Space Company, LMSC-655480, 31 October 1964 (Confidential Report).
44. Langill, A. W., Dynamic Response Analysis of Motor 52-TW-7, Aerojet-General Corporation, 9 September 1963.
45. Ingebo, R. D., Drag Coefficients for Droplets and Solid Spheres in Clouds Accelerating in Air-Stream, NACA TN 3762, September 1956.
46. Williams, F. A., "Progress in Spray-Combustion Analysis," Eighth International Symposium on Combustion, The Williams and Wilkins Company, Baltimore, 1962.
47. Courant, R. and Friedrichs, K. O., Supersonic Flow and Shock Waves, Interscience Publishers, New York, 1948.
48. Ferri, A., Elements of Aerodynamics of Supersonic Flows, The MacMillan Company, New York 1949.
49. Shapiro, A. H., The Dynamics and Thermodynamics of Compressible Fluid Flow, Volumes I and II, The Ronald Press Company, New York, 1954.
50. Dahm, T. J., The Development of an Analogy to Blast-Wave Theory for the Prediction of Interaction Forces Associated with Gaseous Injection Into a Supersonic Stream, Vidya Division of Itek Corp., Vidya Technical Note 9166-TN-3, May 1964.
51. Thrust Vector Control Evaluation (u), Appendix C, Space General Corporation, Document No. 02046 (Final) for A. C. Spark Plug, January, 1965. (Confidential Report.)

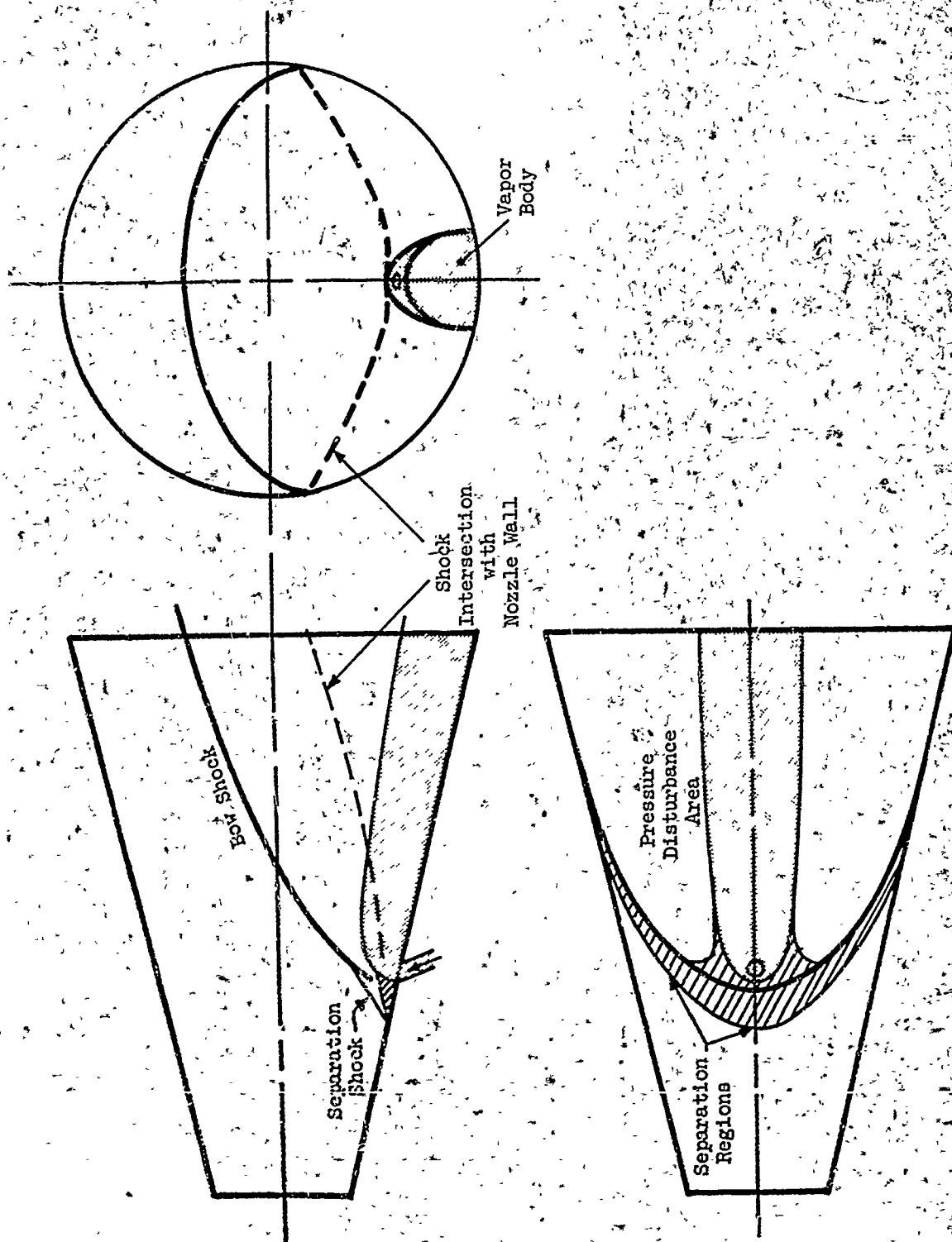


Figure 1

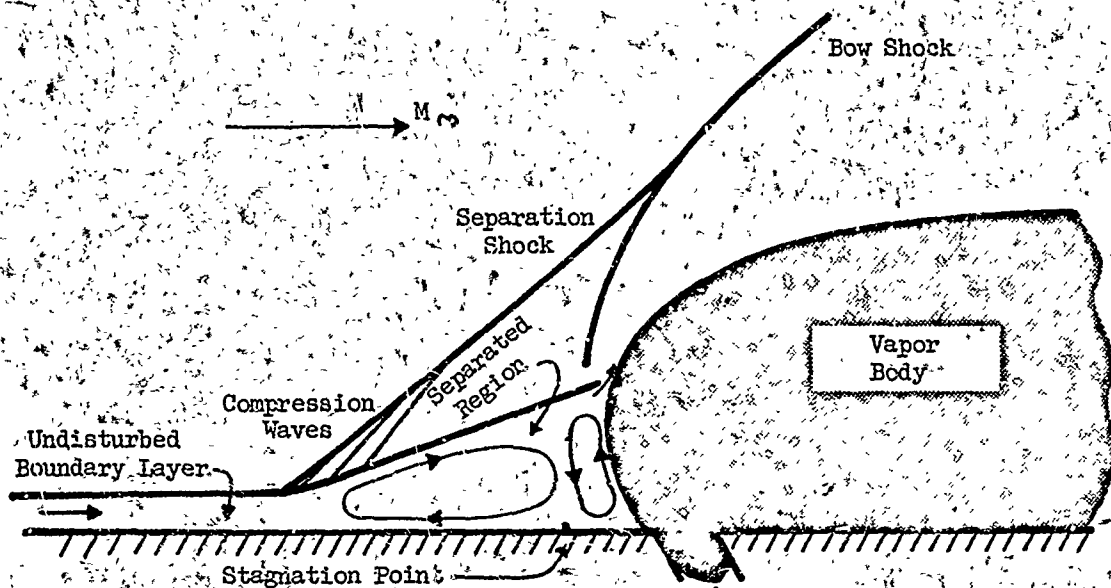


Figure 2a, Forward Separation Region

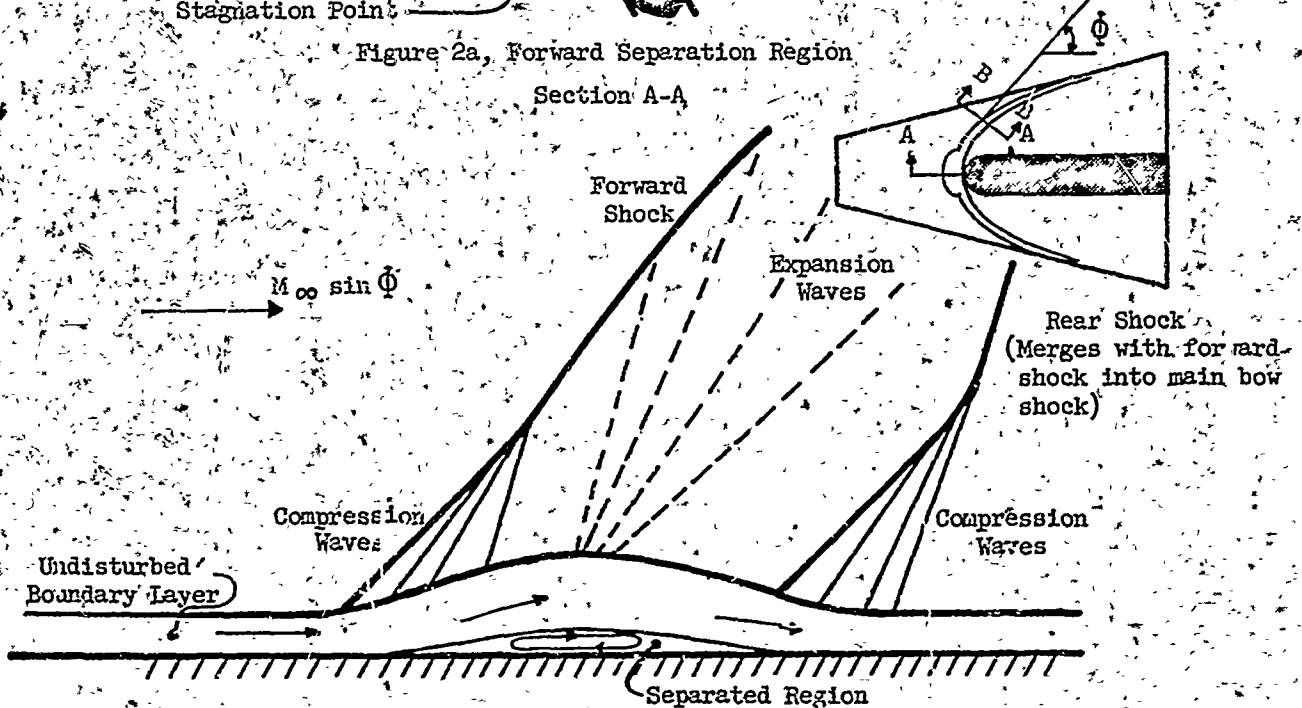


Figure 2b, Shock Intersection with Wall

Section B-B

Flow Separation Patterns

Figure 2

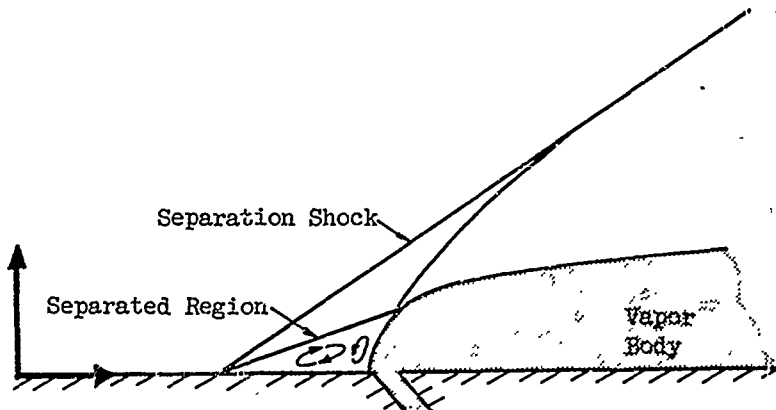
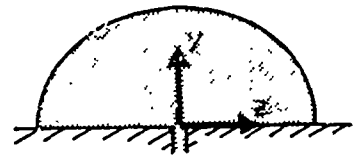


Figure 3a, Low Penetration



Vapor Body
Cross-Sections

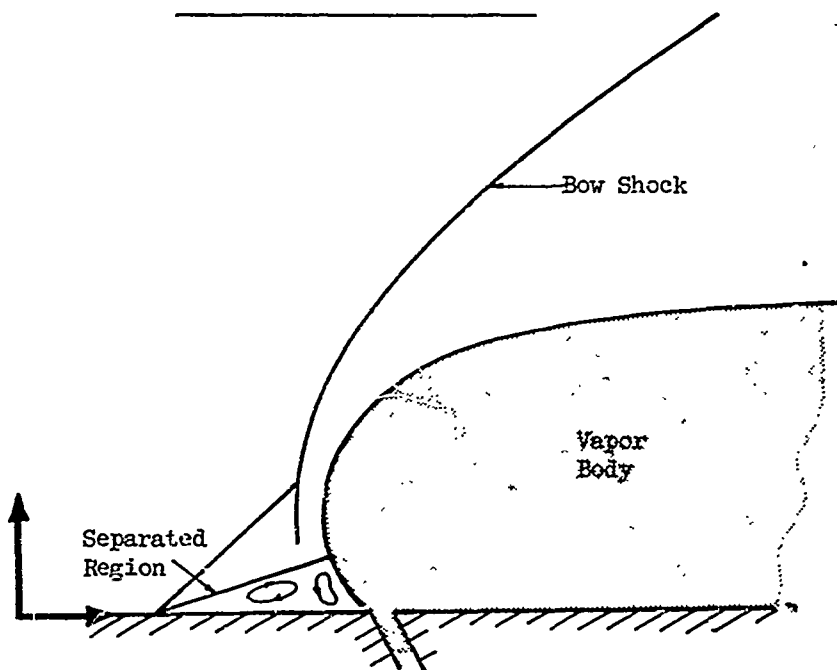
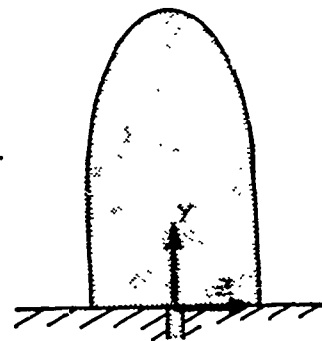


Figure 3b, High Penetration

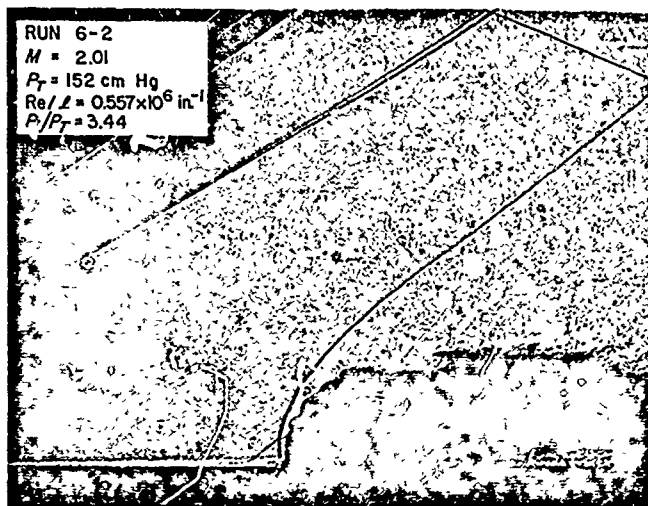


Effect of Liquid-Jet Penetration on Flow Pattern

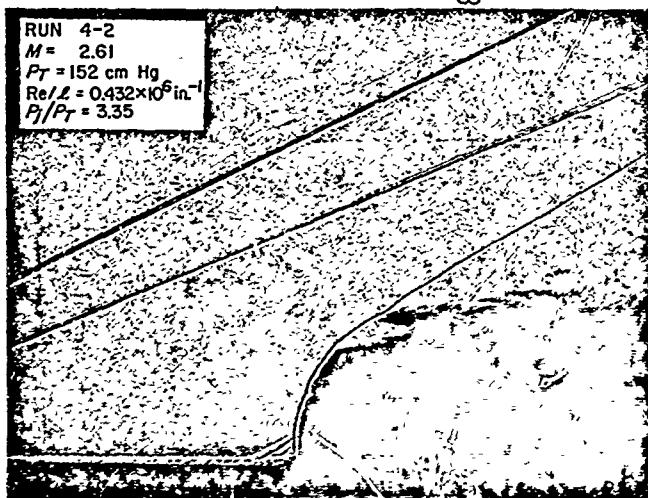
Figure 3

TM-16-SRO

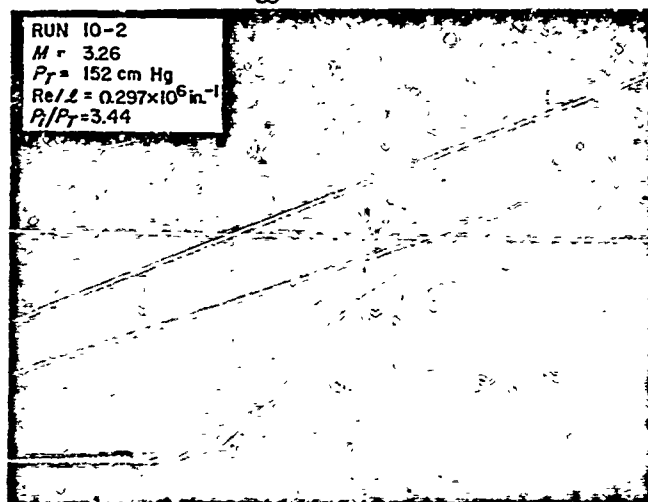
(REF. 8)



Free Stream Mach Number, $M_\infty = 2.01$



$M_\infty = 2.61$

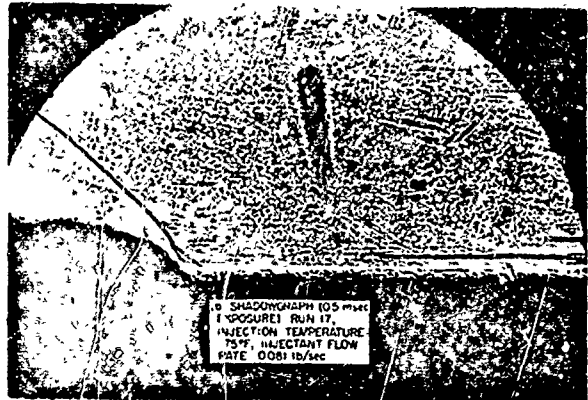
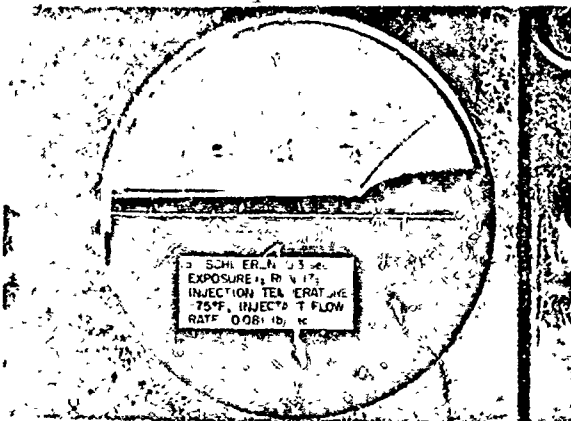


$M_\infty = 3.26$

Shadowgraphs for Liquid Nitrogen Injection through a Flat Plate

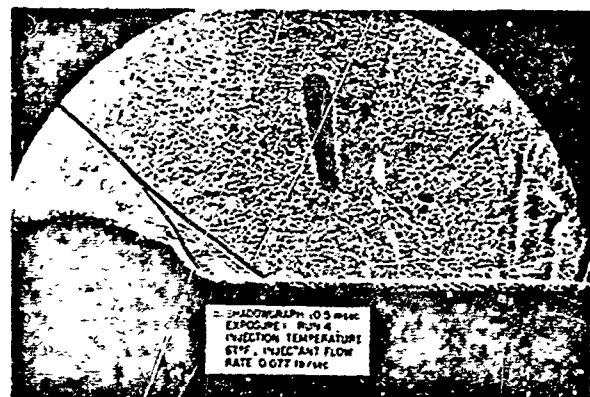
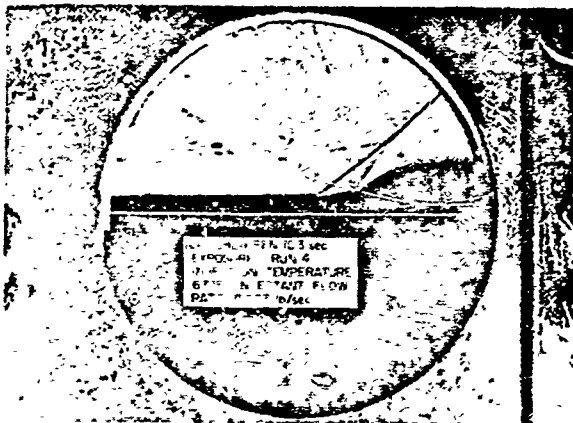
Figure 4

TM-16-SRO



SCHLIEREN AND SPARK SHADOWGRAPH FOR FREON 12 WITH AN INJECTION TEMPERATURE OF -75°F

$$M_{\infty} = 2.01$$



SCHLIEREN AND SPARK SHADOWGRAPH FOR FREON 12 WITH AN INJECTION TEMPERATURE OF 67°F

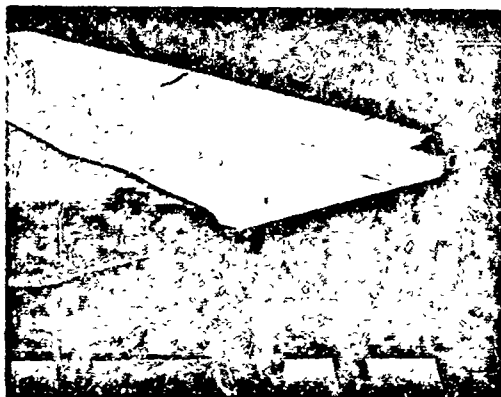
$$M_{\infty} = 2.01$$

Schlieren and Spark Shadowgraphs for Flat Plate Tests with Freon 12

Figure 5

TM-16-SRO

(REF. 10)



Liquid Nitrogen Injection $\dot{w}_s/\dot{w}_A = 0.060$, $M_\infty = 3.20$



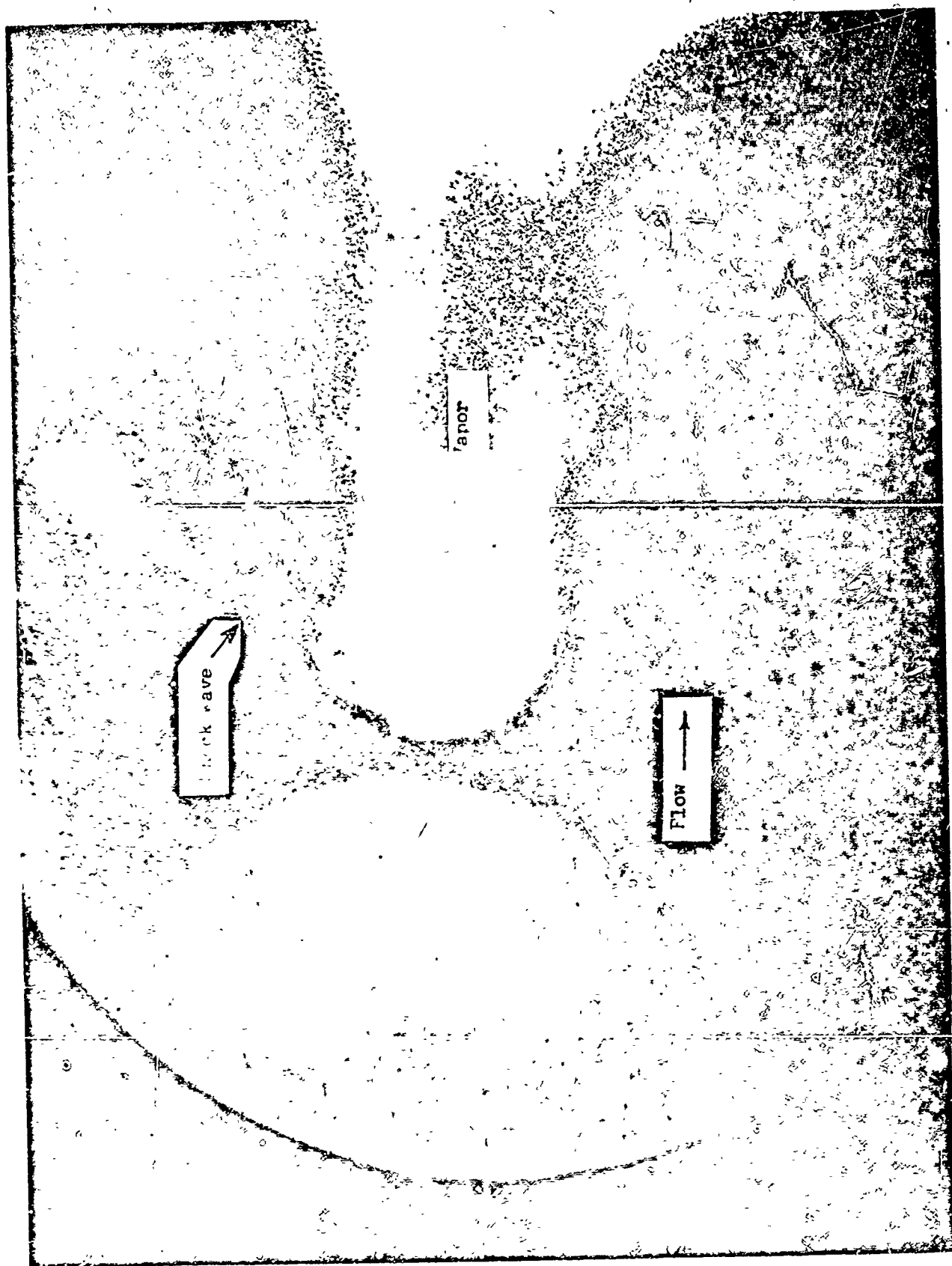
Liquid Nitrogen Injection $\dot{w}_s/\dot{w}_A = 0.059$, $M_\infty = 2.20$

Schlieren Photographs from Two-Dimensional Nozzle

Figure 6

[NOT REPRODUCIBLE]

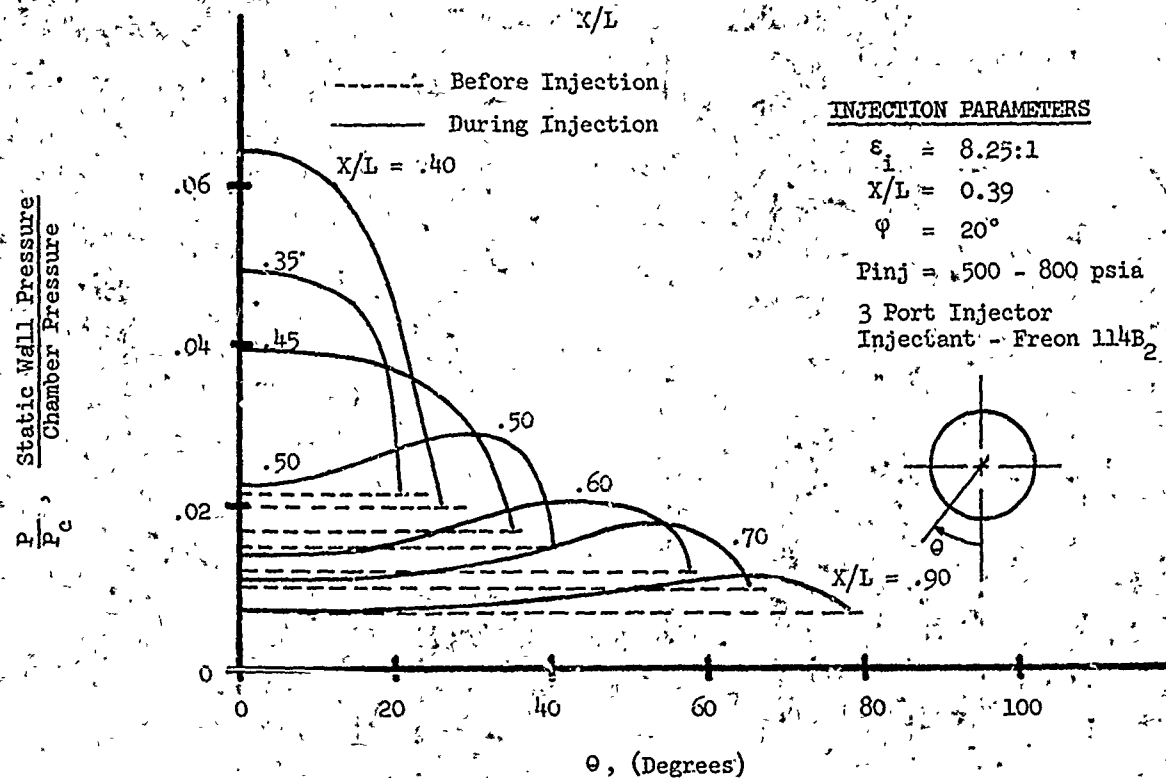
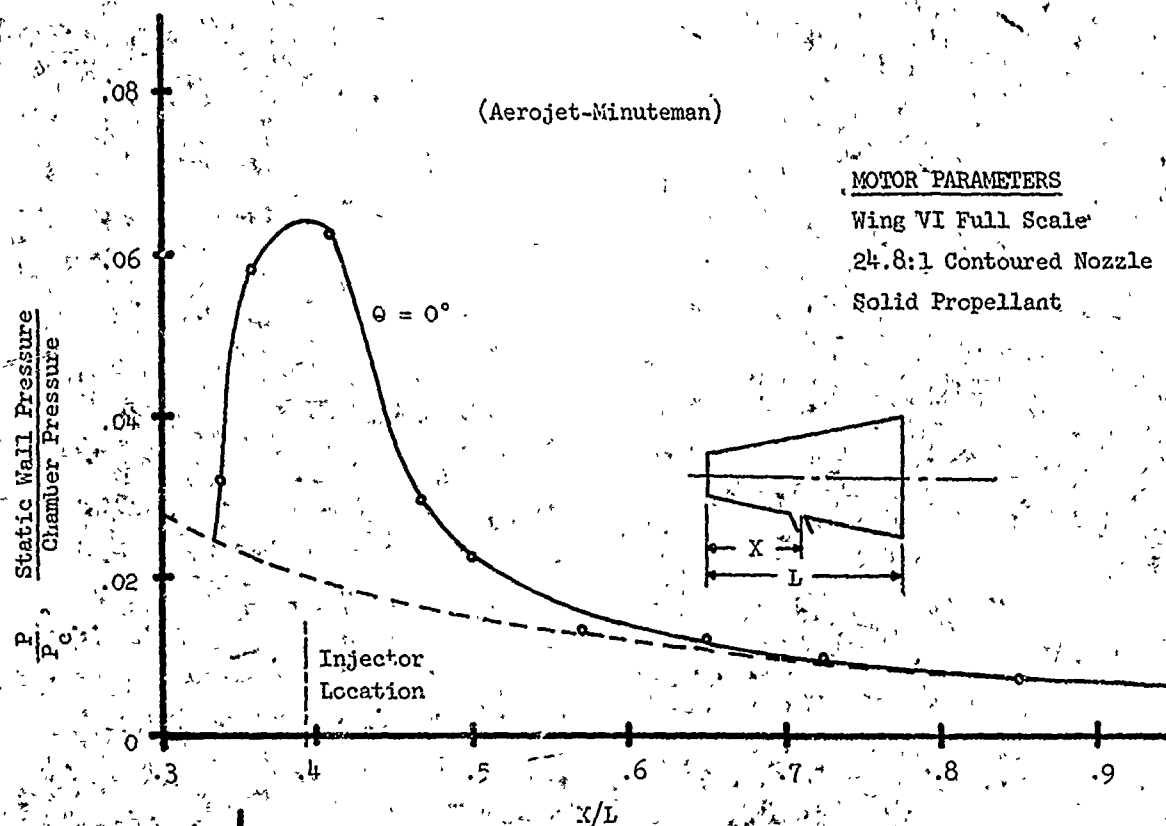
TM-15-SRO



Photograph of Freon 114B₂ Injection During Hot Firing of Solid
Propellant Motor

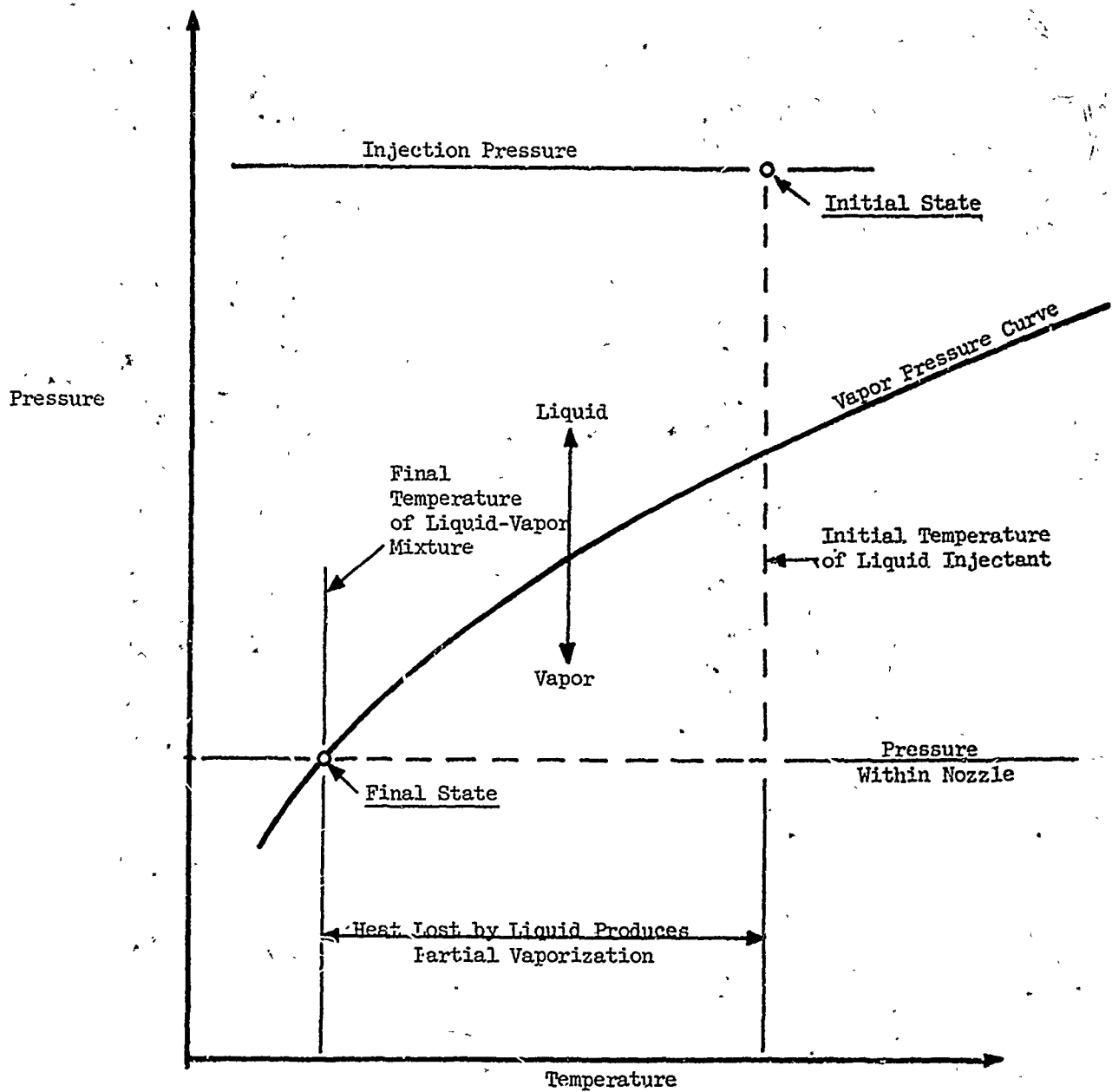
Figure 7

TM-16-SRO



Measured Pressure Distributions for LITVC

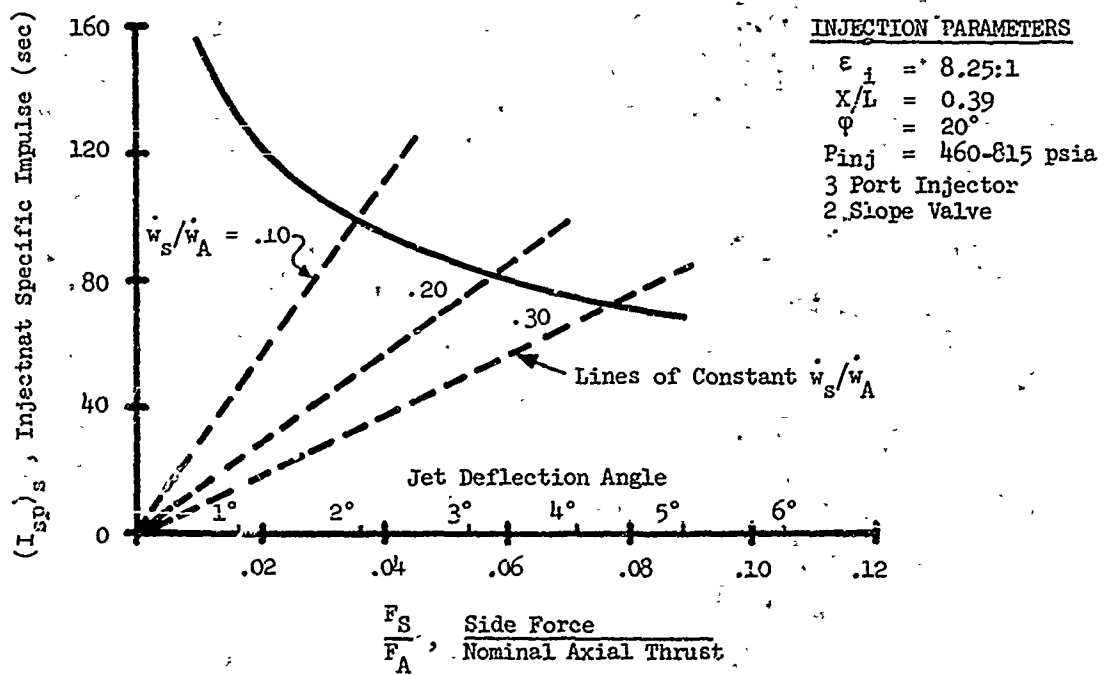
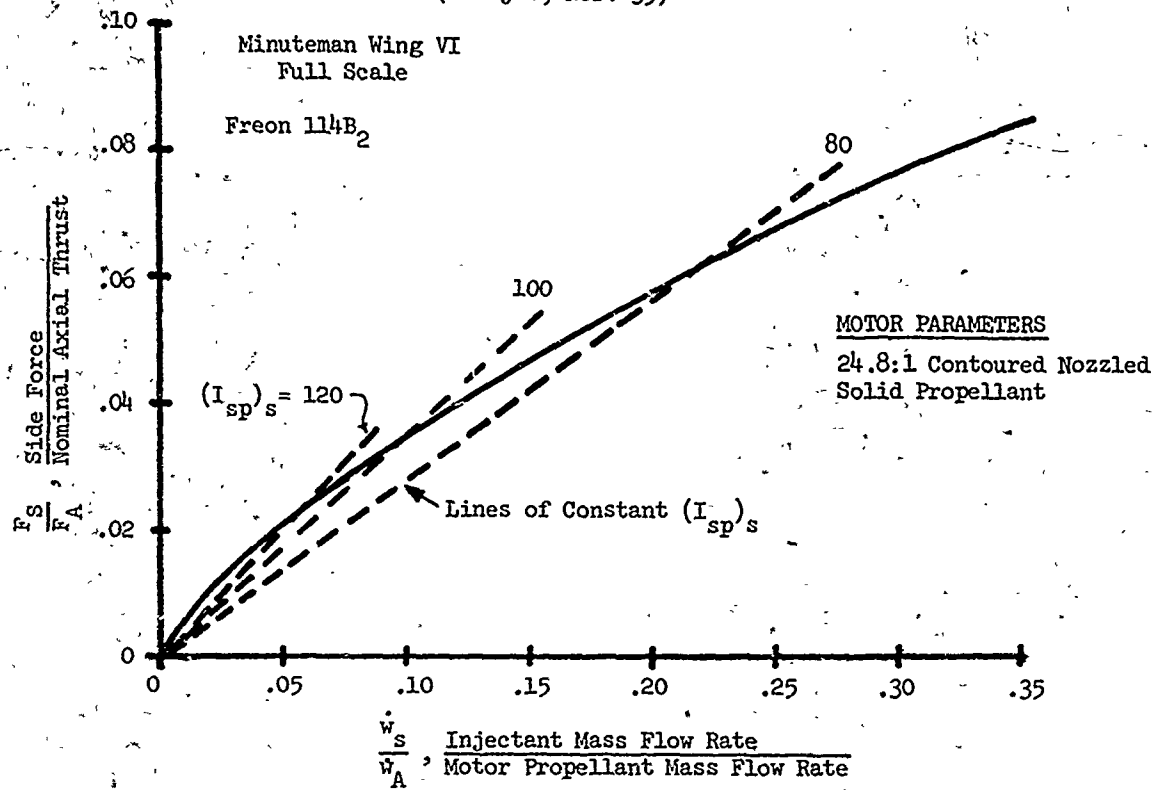
Figure 8



Flash Vaporization

Figure 9

(Aerojet, Ref. 39)

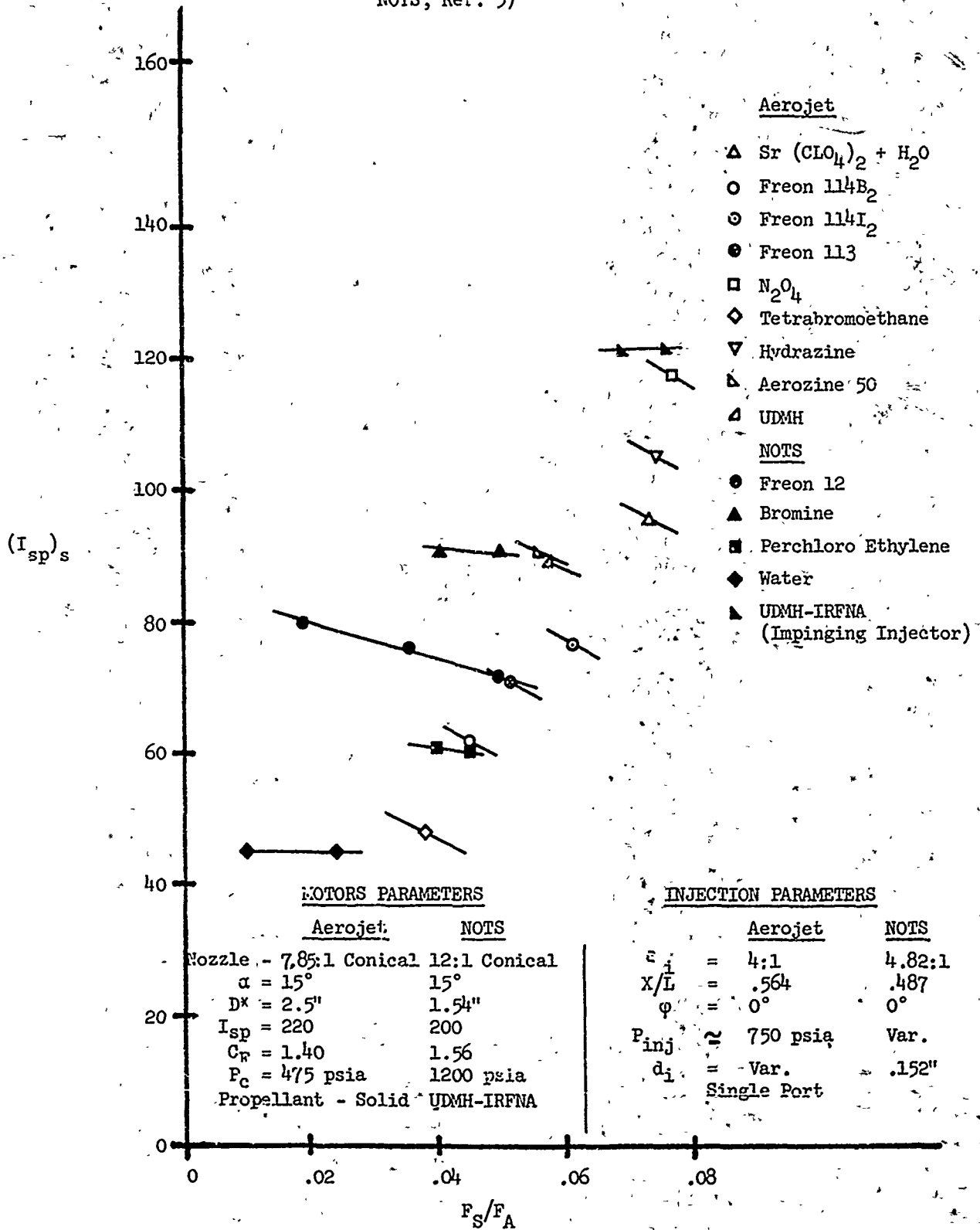


Typical Liquid-Injection TVC Performance Curves

Figure 10

TM-16-SRO

(Aerojet, Ref. 41, 42
NOTS, Ref. 5)



Performance of Various Liquid Injectants (B)

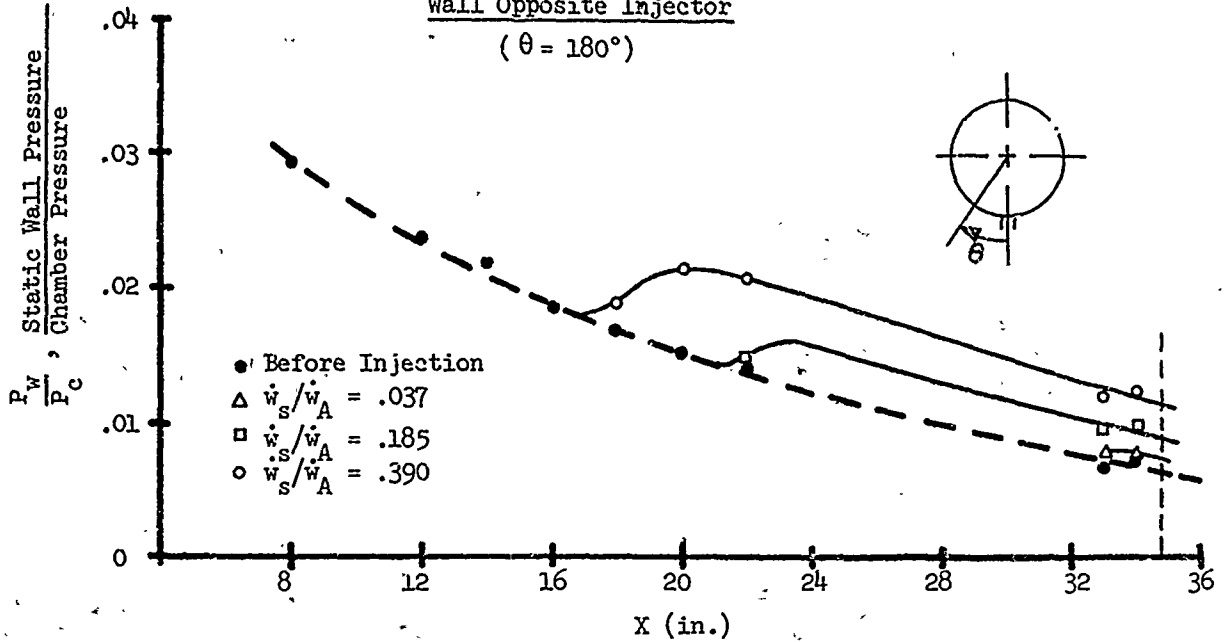
Figure 2

TM-16-SRO

(Aerojet - Minuteman, Ref. 35)

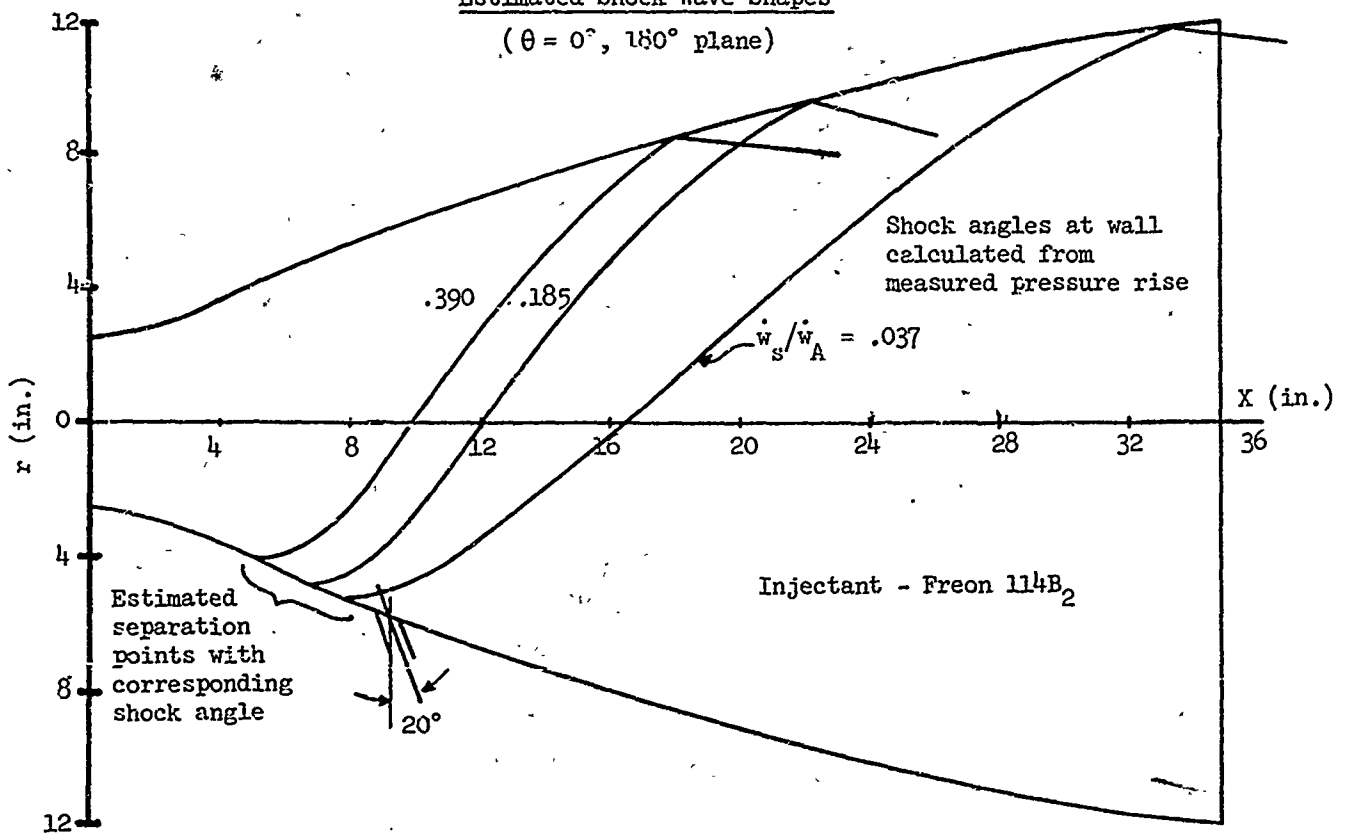
Pressure Distributions on Nozzle
Wall Opposite Injector

($\theta = 180^\circ$)



Estimated Shock Wave Shapes

($\theta = 0^\circ, 180^\circ$ plane)



Shock Reflections Produced by Liquid Injection

Figure 16

TM-16-SRO

(NOTS, Ref. 5)

MOTOR PARAMETERS

12:1 Conical Nozzle

$\alpha = 15^\circ$

$D^* = 1.54''$

$I_{sp} = 200$

$C_F = 1.57$

$P_c = 1200$ psia

Propellant - UDMH/IRFNA

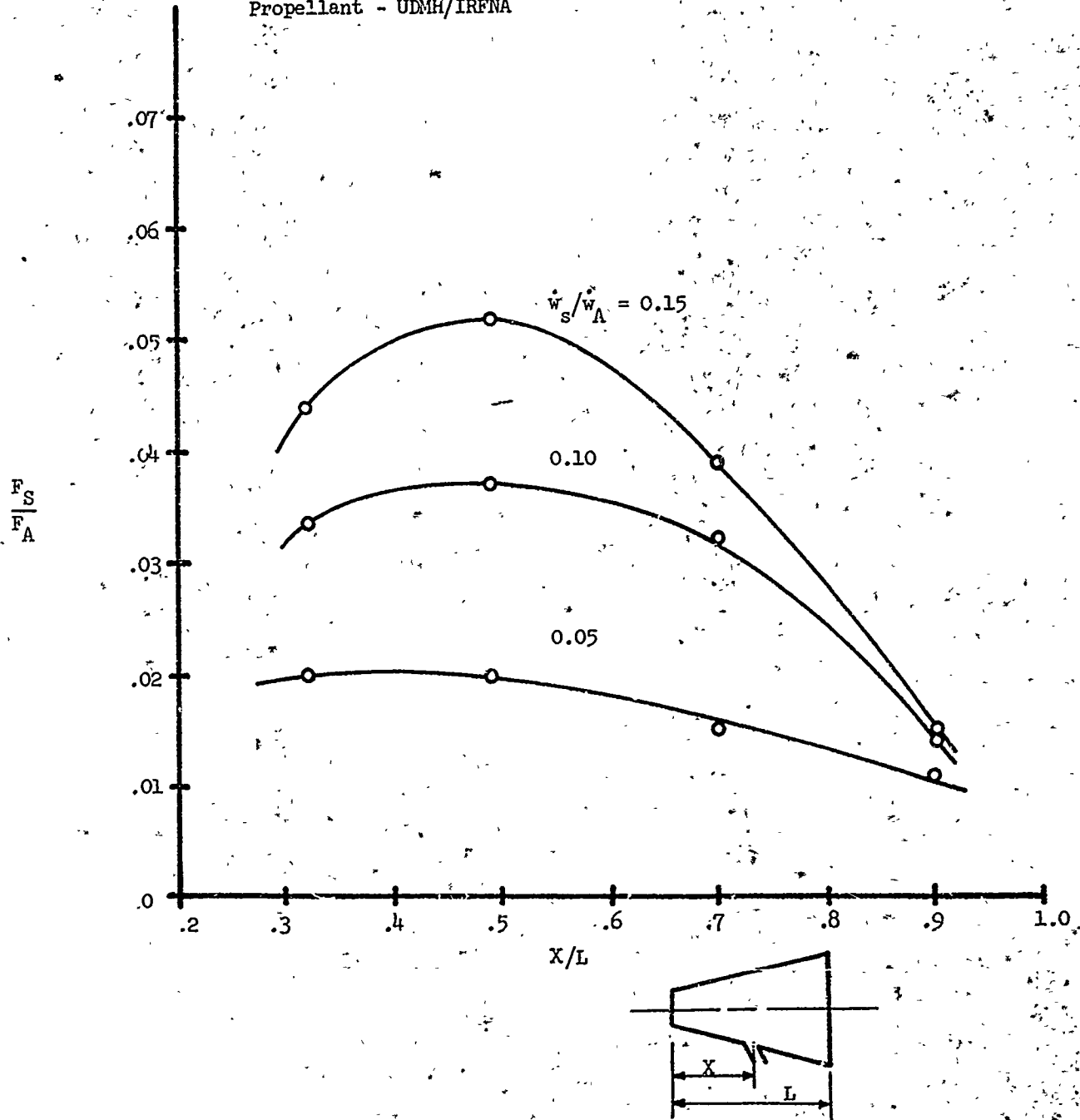
INJECTION PARAMETERS

$\phi = 0^\circ$

$d_i = 0.152''$

Single Port

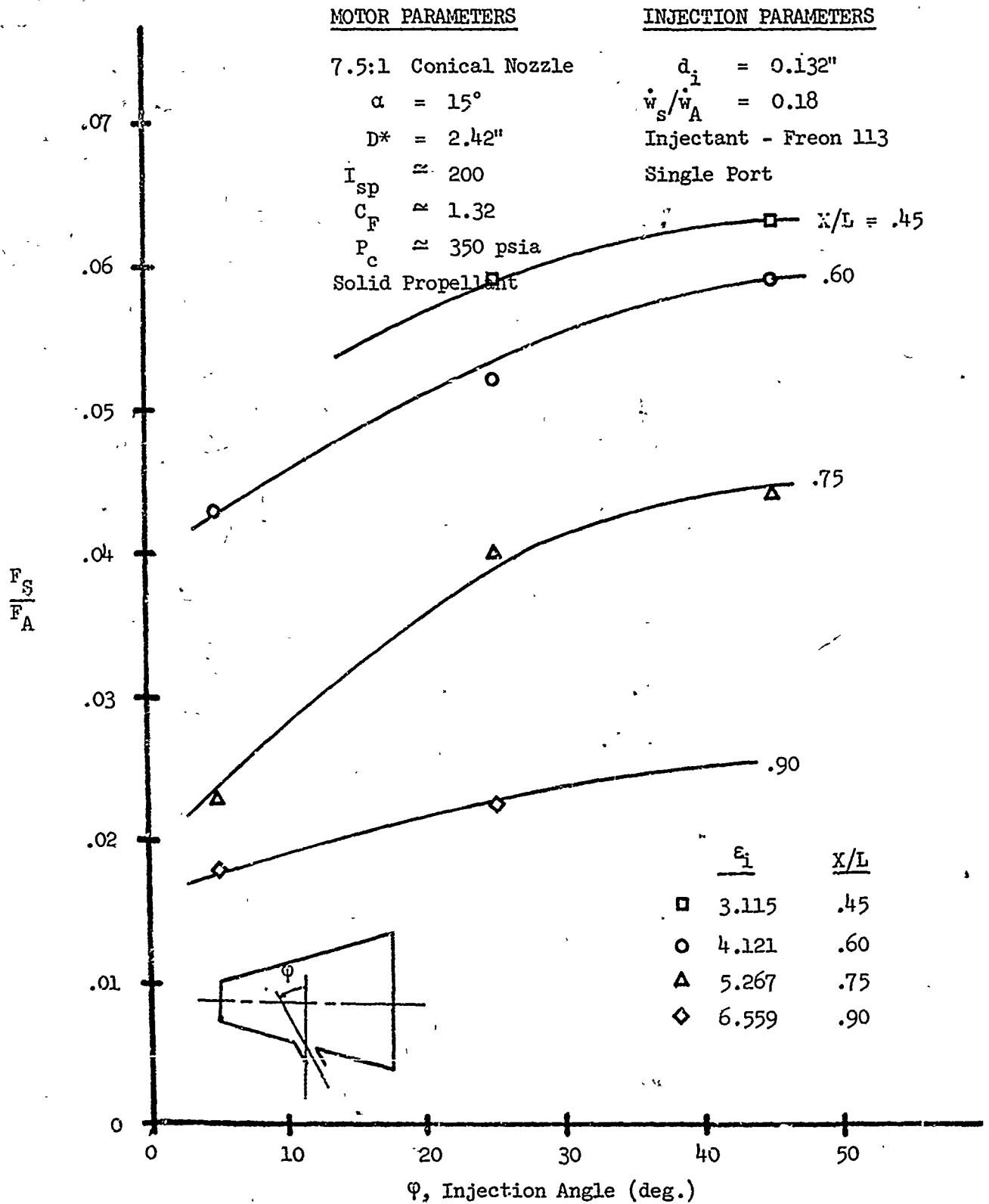
Injectant - Freon 12



Effect of Injector Location

Figure 17

TM-16-SRO
(Aerojet - Polaris, Ref. 38)



Effect of Injection Angle

Figure 20

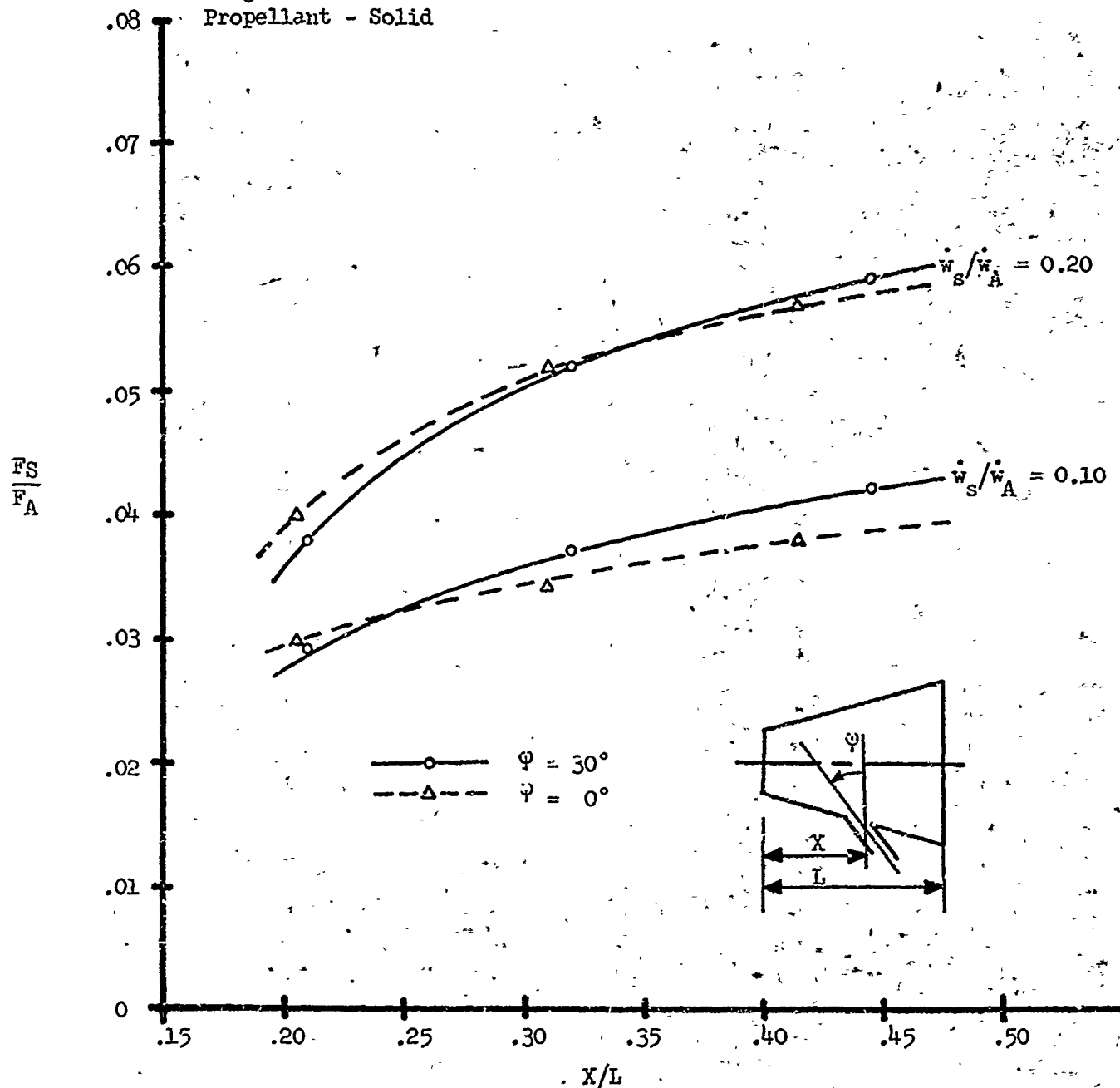
(Aerojet - Minuteman, Ref. 33, 34)

MOTOR PARAMETERS

23.5:1 Contoured Nozzle
 $D^* = 4.988''$
 $I_{sp} \approx 279$
 $C_F \approx 1.75$
 $P_c \approx 500$ psia
 Propellant - Solid

INJECTION PARAMETERS

$P_{inj} \approx 1200$ psia
 Single Port
 Injectant - Freon 114B₂



Effect of Injection Angle and Location

Figure 21

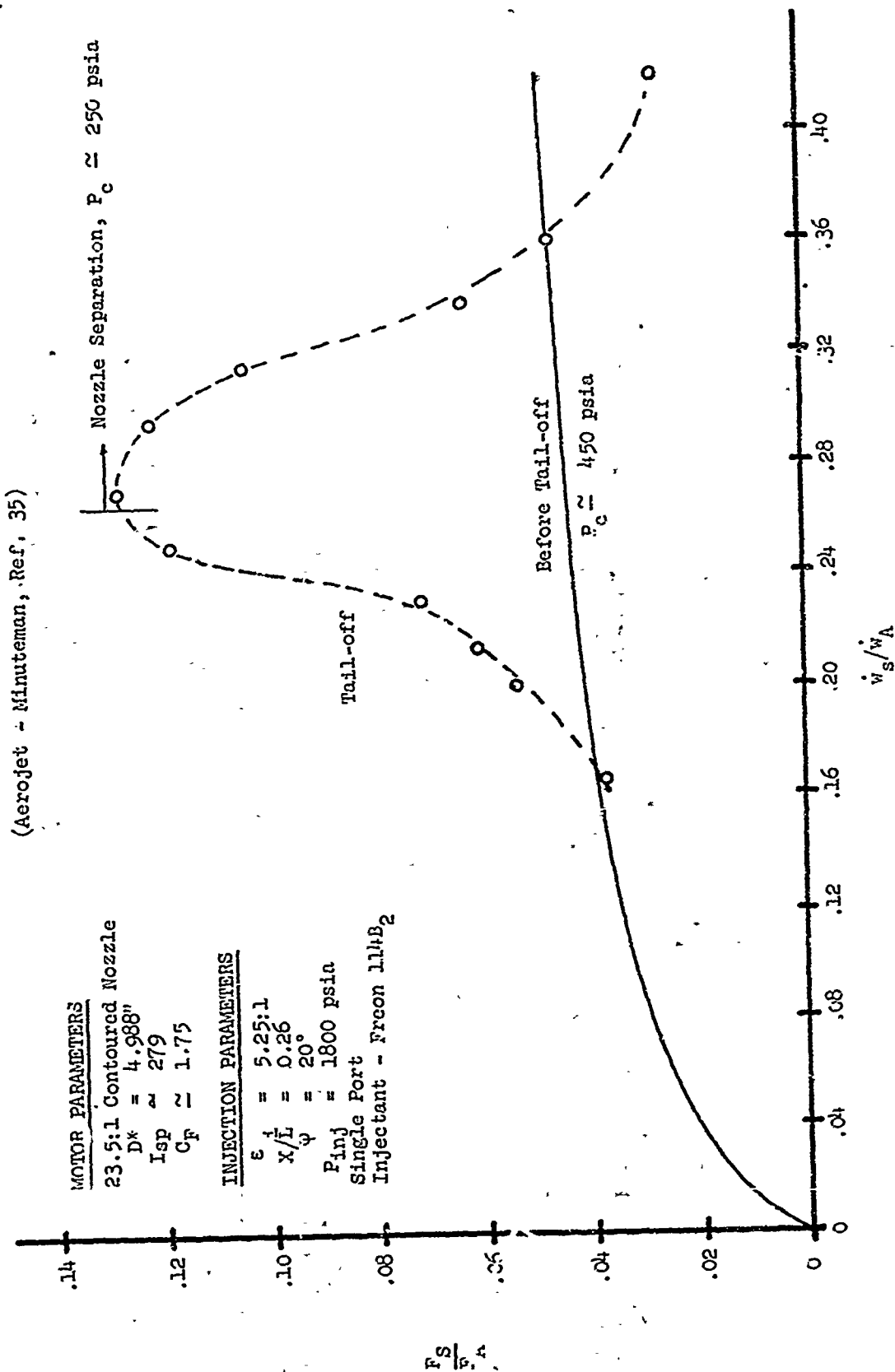
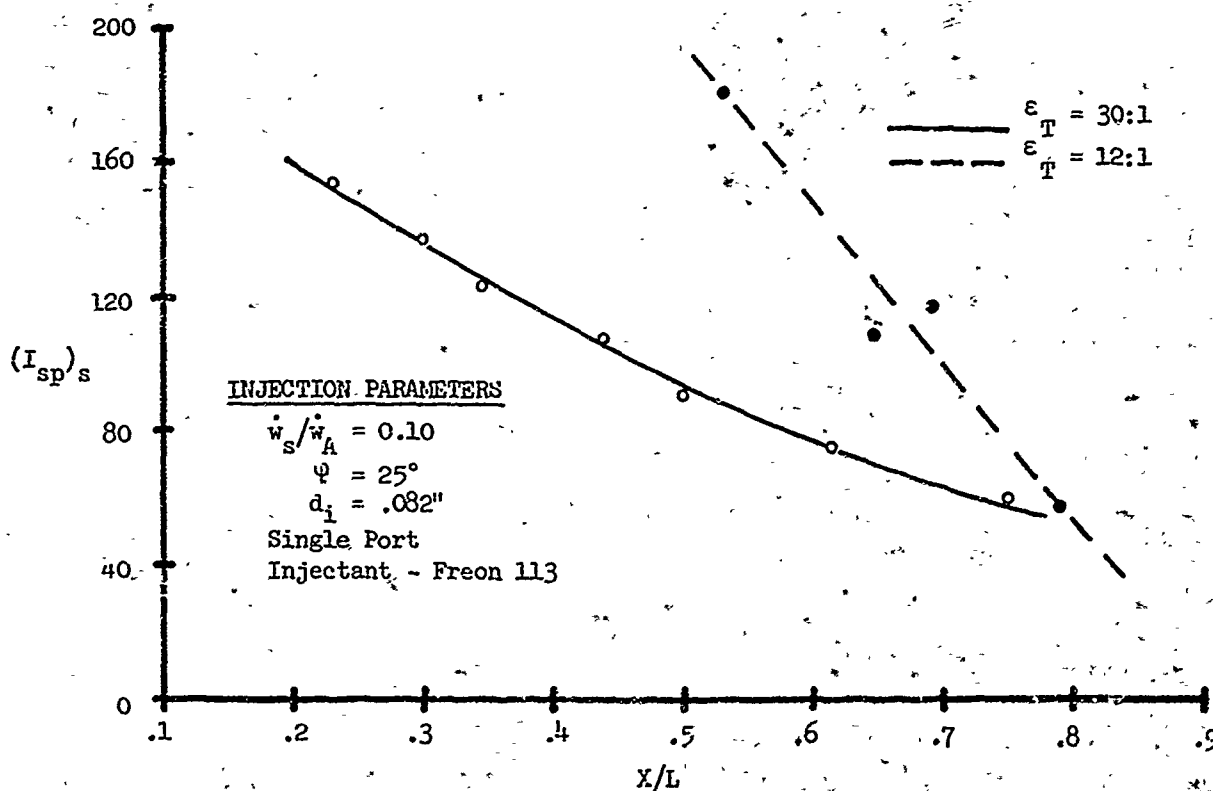
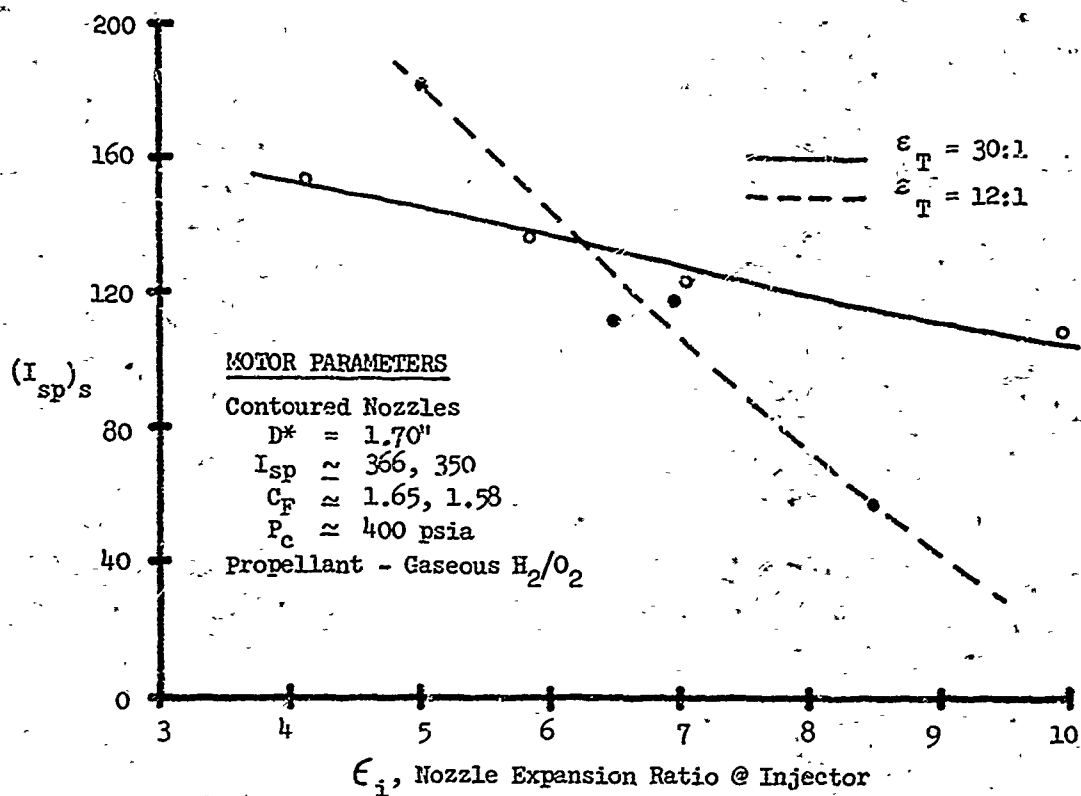


Figure 24

LITVC Performance During Motor Tail-off

TM-16-SRO

(Aerojet - Polaris, Ref. 37)



Effect of Nozzle Expansion Ratio

Figure 25

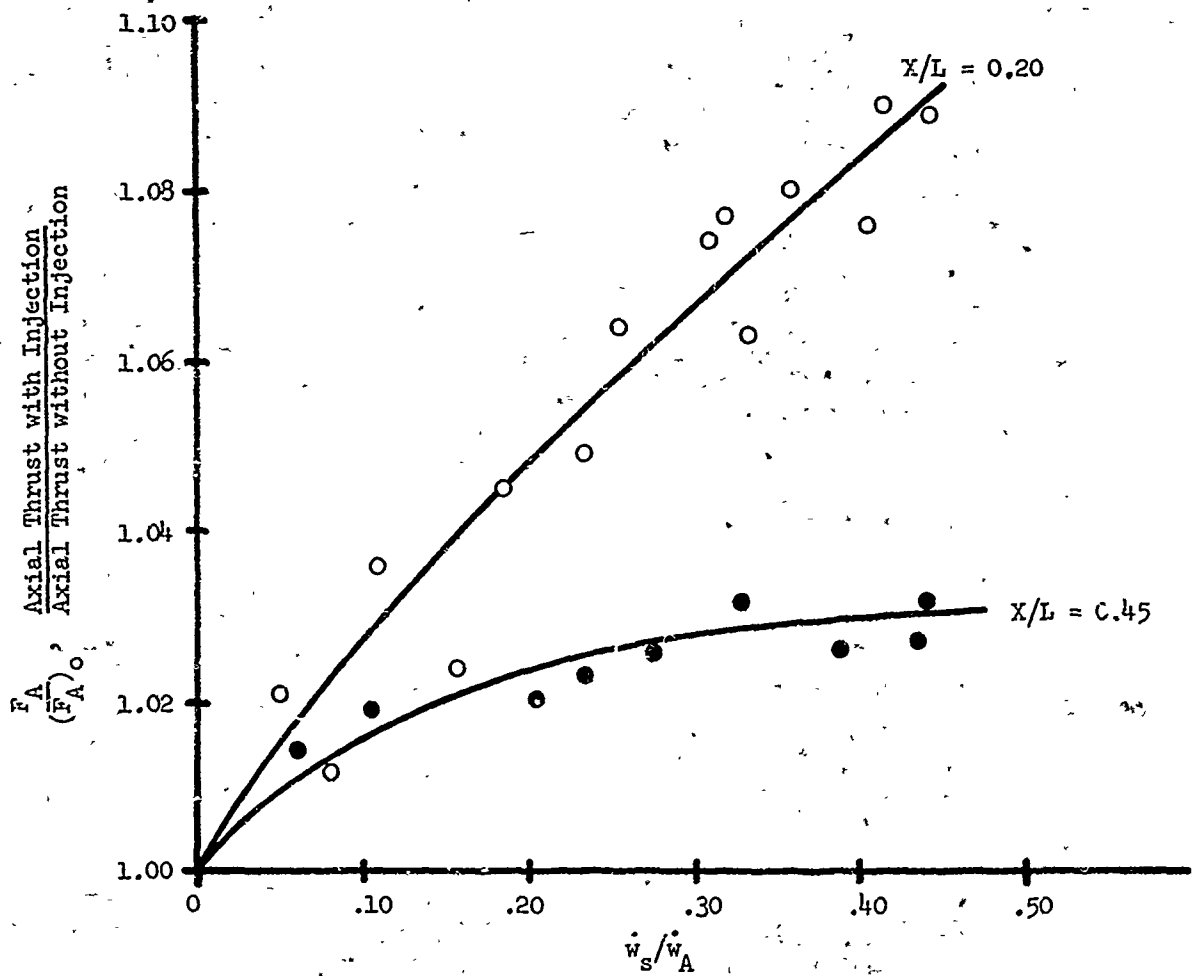
(Aerojet - Minuteman, Re 34)

MOTOR PARAMETERS

23.5:1 Contoured Nozzle
 $D^* = 4.988''$
 $I_{sp} \approx 279$
 $C_F \approx 1.75$
 $P_c \approx 450$ psia
 Solid Propellant

INJECTION PARAMETERS

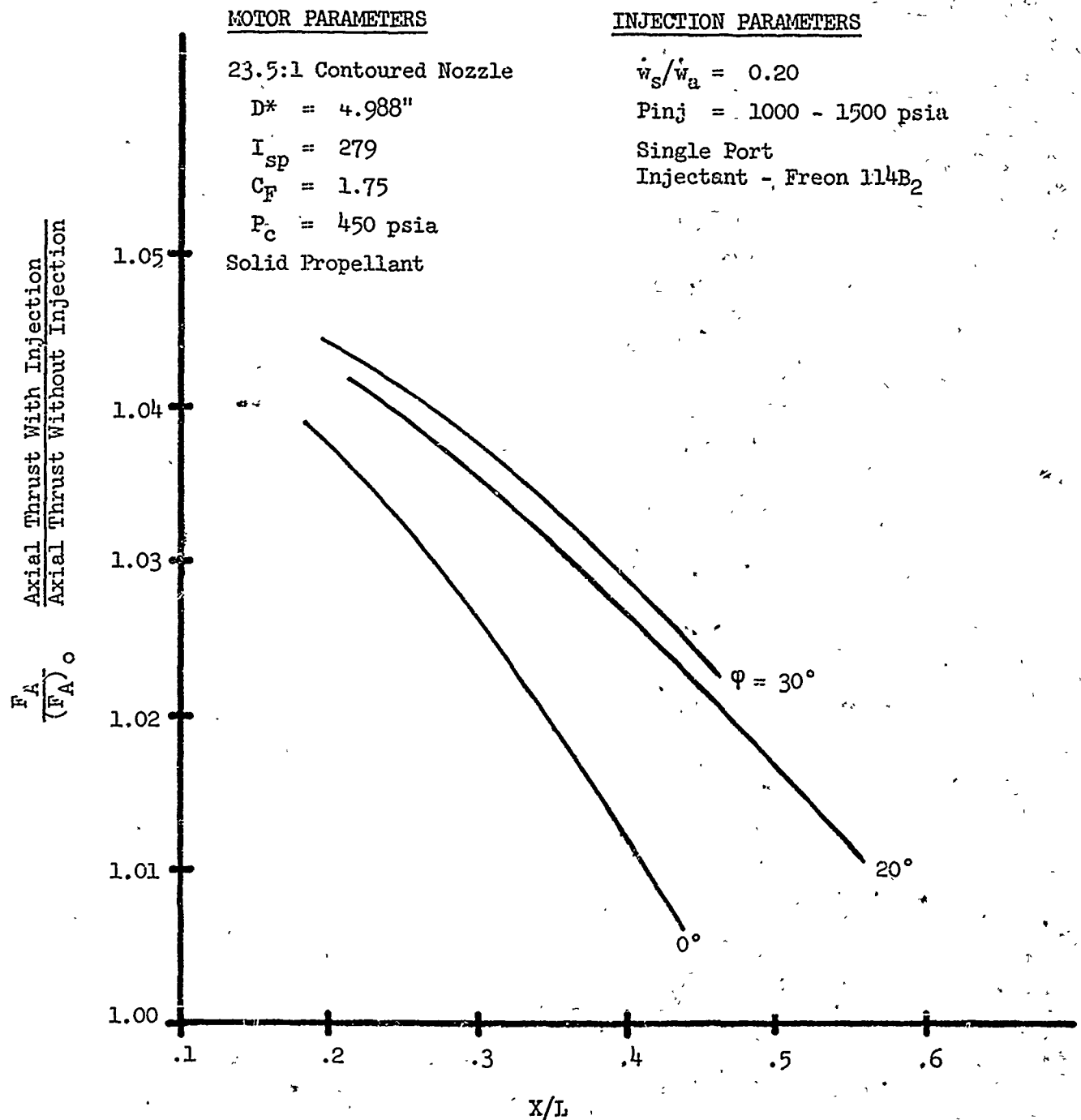
$\psi = 30^\circ$
 $P_{inj} = 1500$ psia
 Single Port
 Injectant - Freon 114B₂



Axial Thrust Augmentation due to Liquid Injection

Figure 27

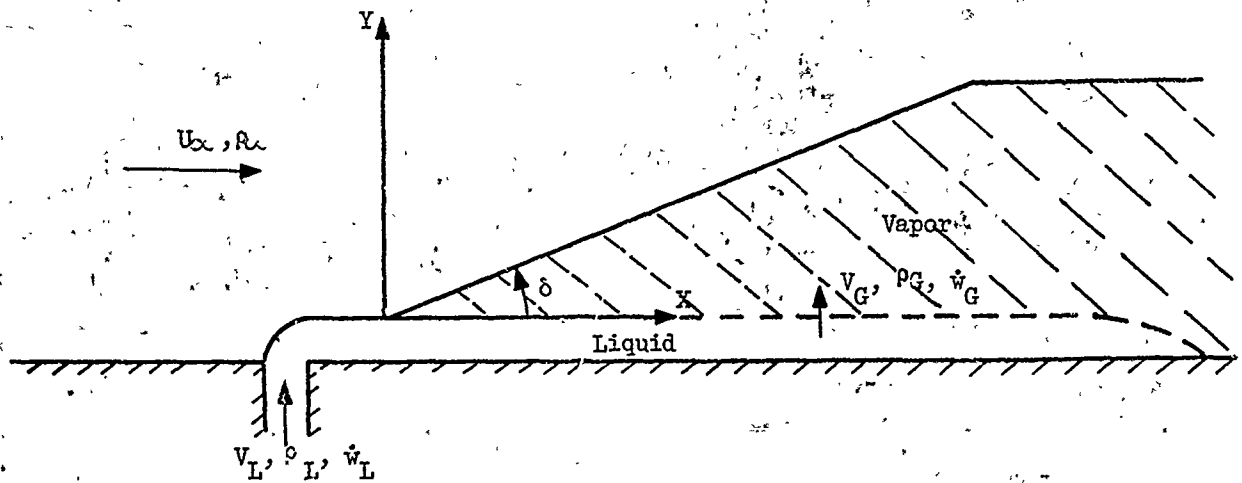
(Aerojet-Minuteman, Ref. 33 - 36).



Effect of Injector Location and Injection Angle on Axial Thrust Augmentation

Figure 28

(NESCO, REF. 17)



Flow assumed to be deflected by a wedge with a half angle δ determined by rate of vapor generation.

Liquid Injection Linearized Model

Figure 29

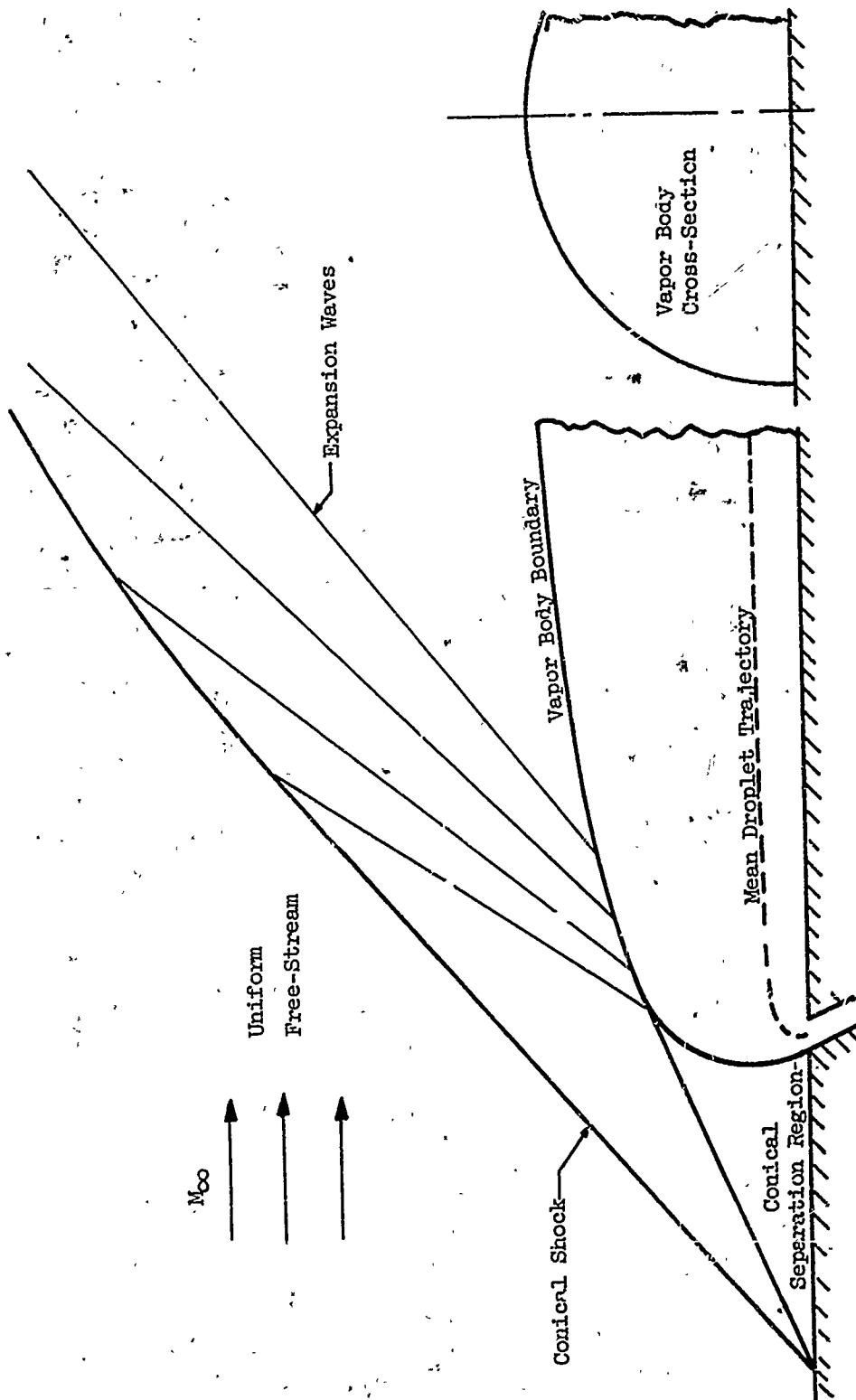


Figure 30

(NESCO, REF. 18)

Liquid-Injection Vapor-Body Model

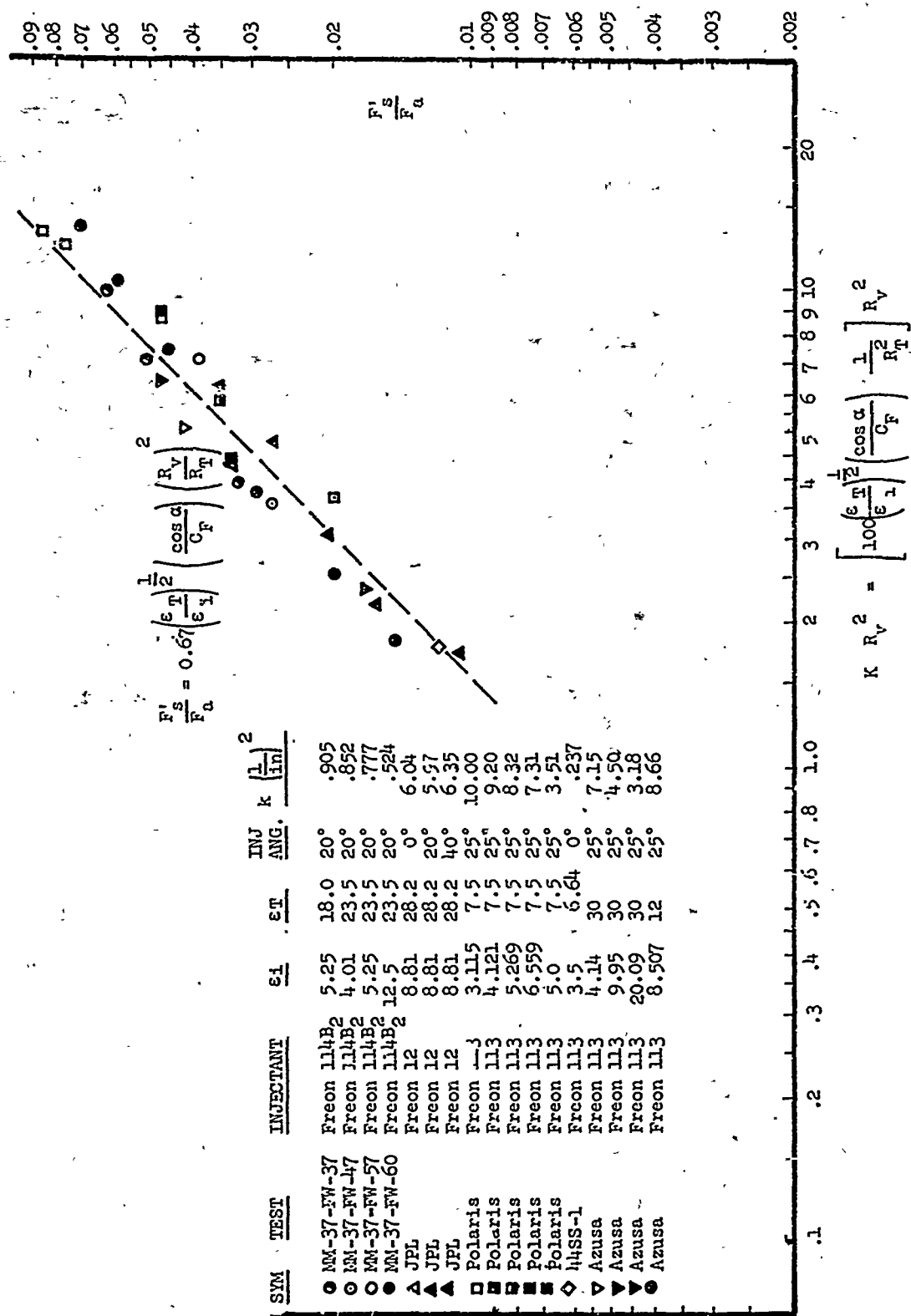
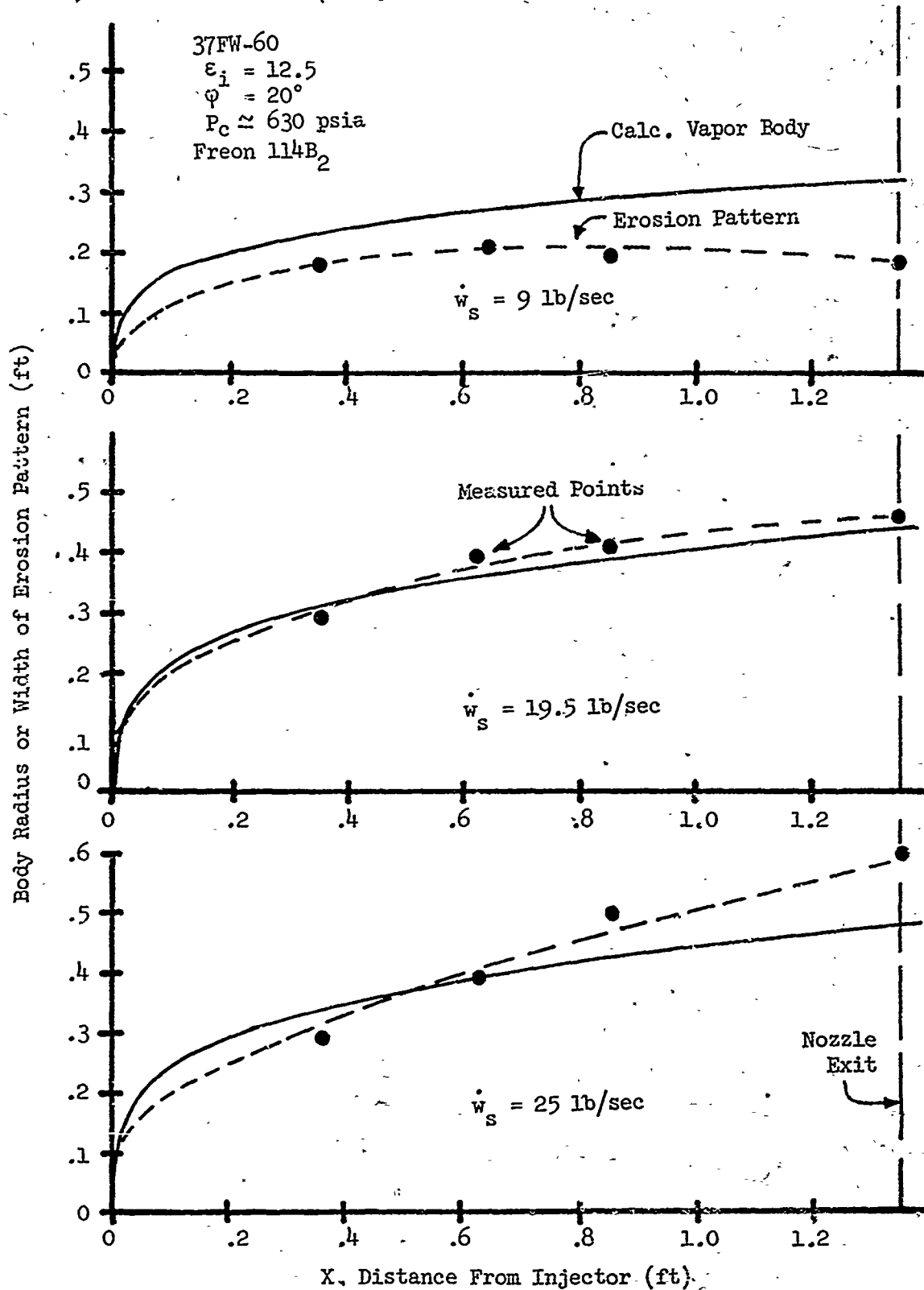


Figure 31

Correlation of Experimental Data with Approximate Model

TM-16-SRO

(Aerojet - Minuteman)



Comparison of Calculated Vapor Bodies with Injectant Erosion Patterns Measured on Nozzle Wall

Figure 33

$\gamma = 1.2$
(Ref. 24)

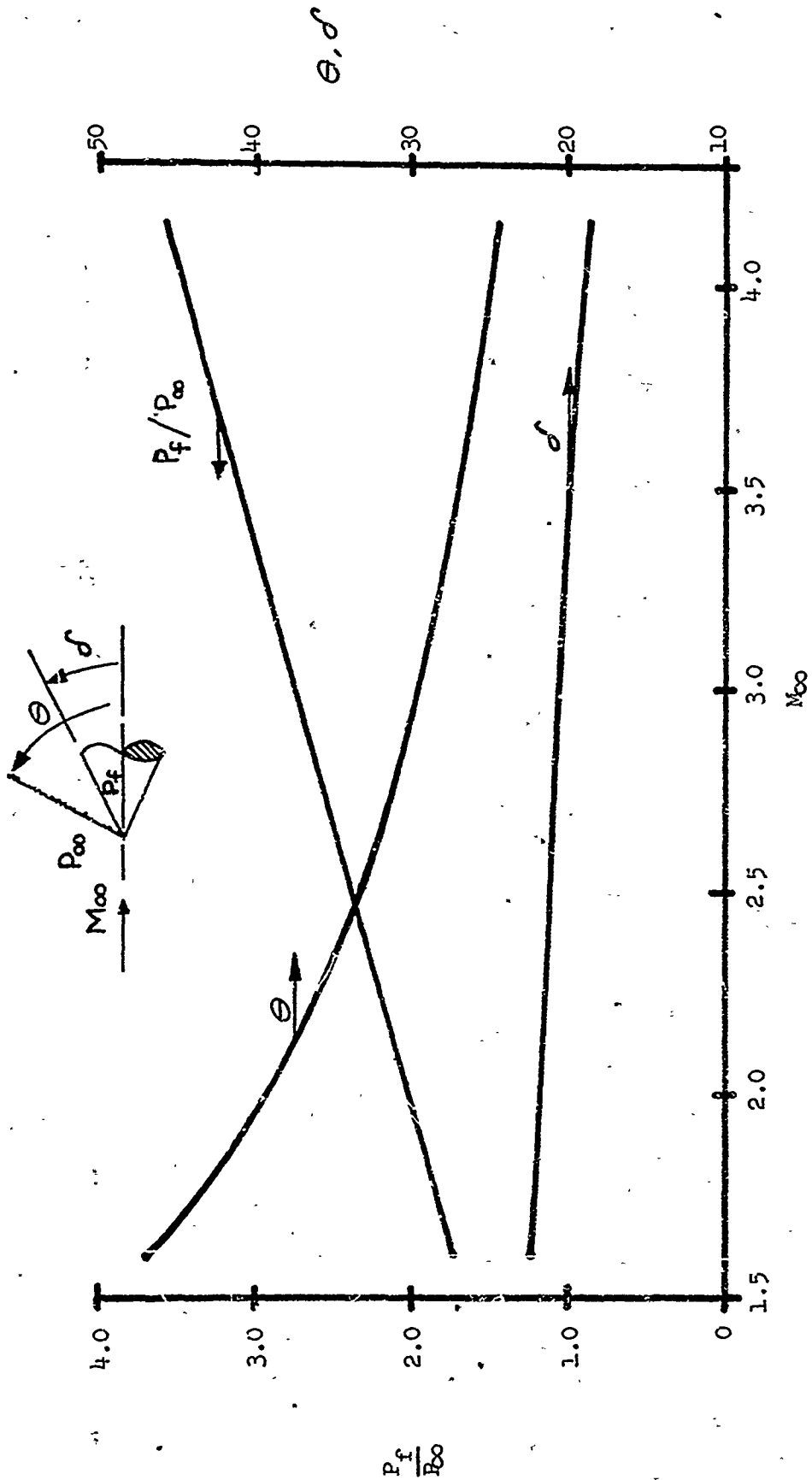


Figure 34

Pressure Rise and Equivalent Cone Angle for Turbulent Boundary Layer Separation

Minuteman Full Scale Nozzle

Freon 114B₂

$\dot{w}_g/\dot{w}_A = .085$

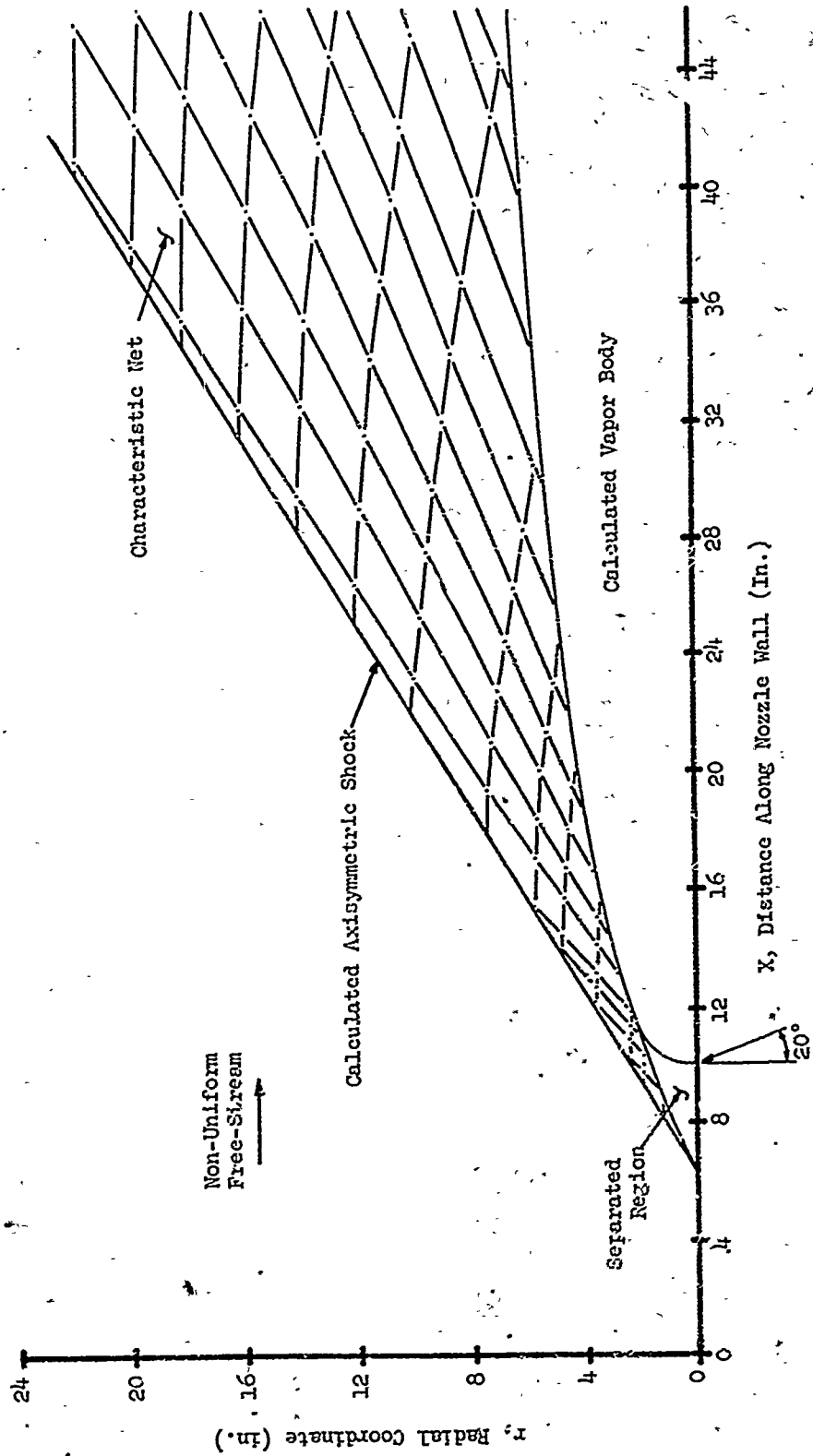


Figure 35

Typical Flow Field Solution

TM-10-SRO

Minuteman Full Scale Nozzle

Freon 114B₂

$\dot{w}_s/\dot{w}_A = .085$

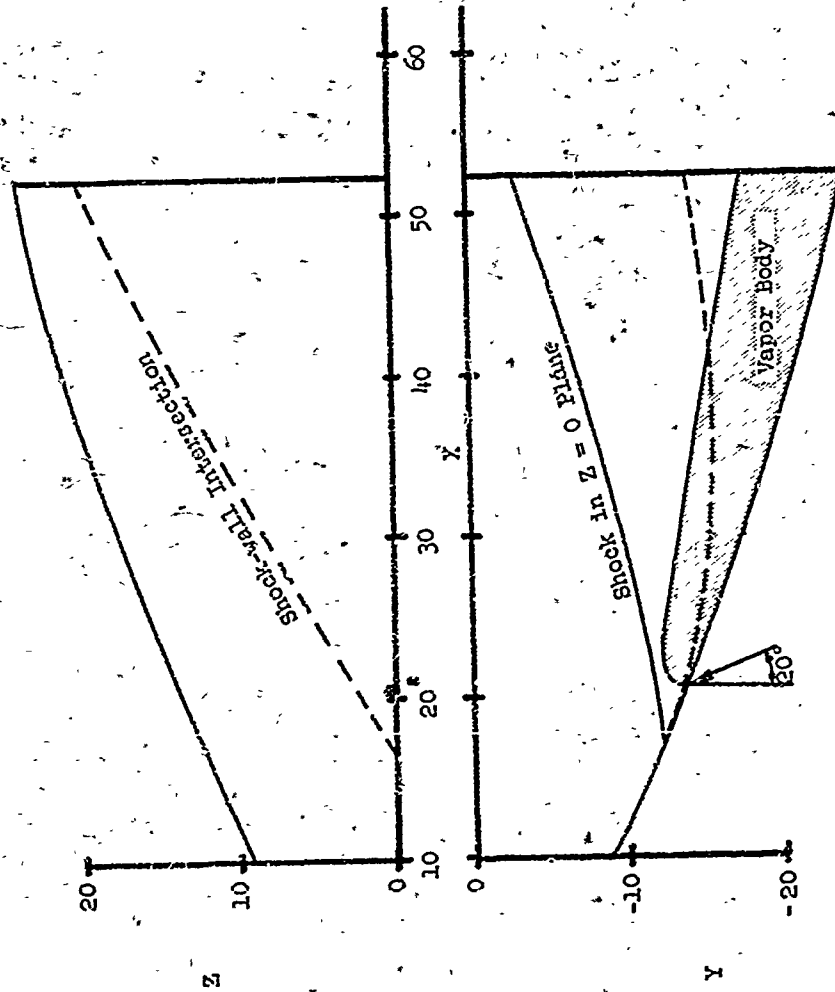
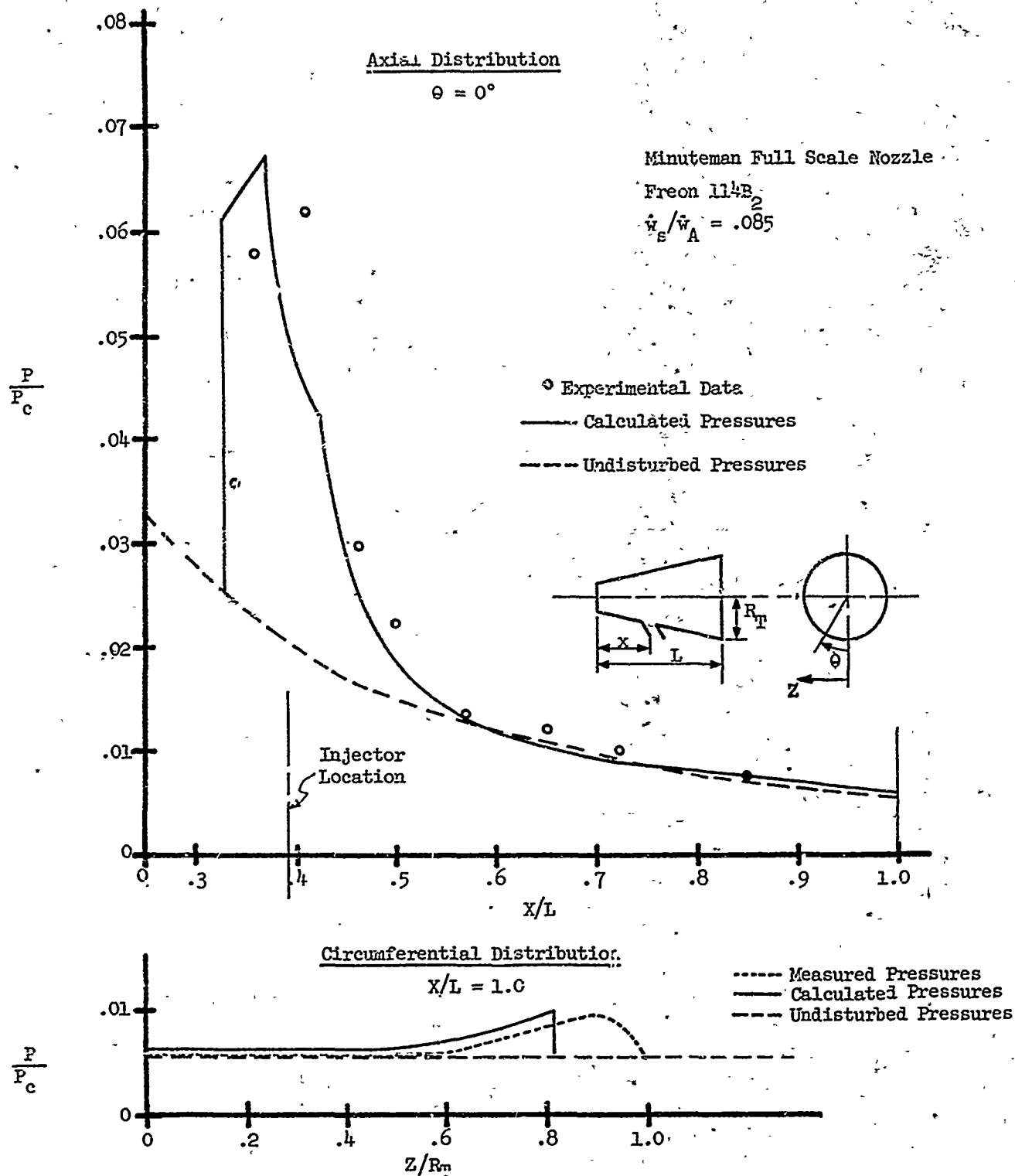


Figure 36

Calculated Shock Intersection with Nozzle Wall



Comparison of Calculated with Measured Pressure Distributions

Figure 37

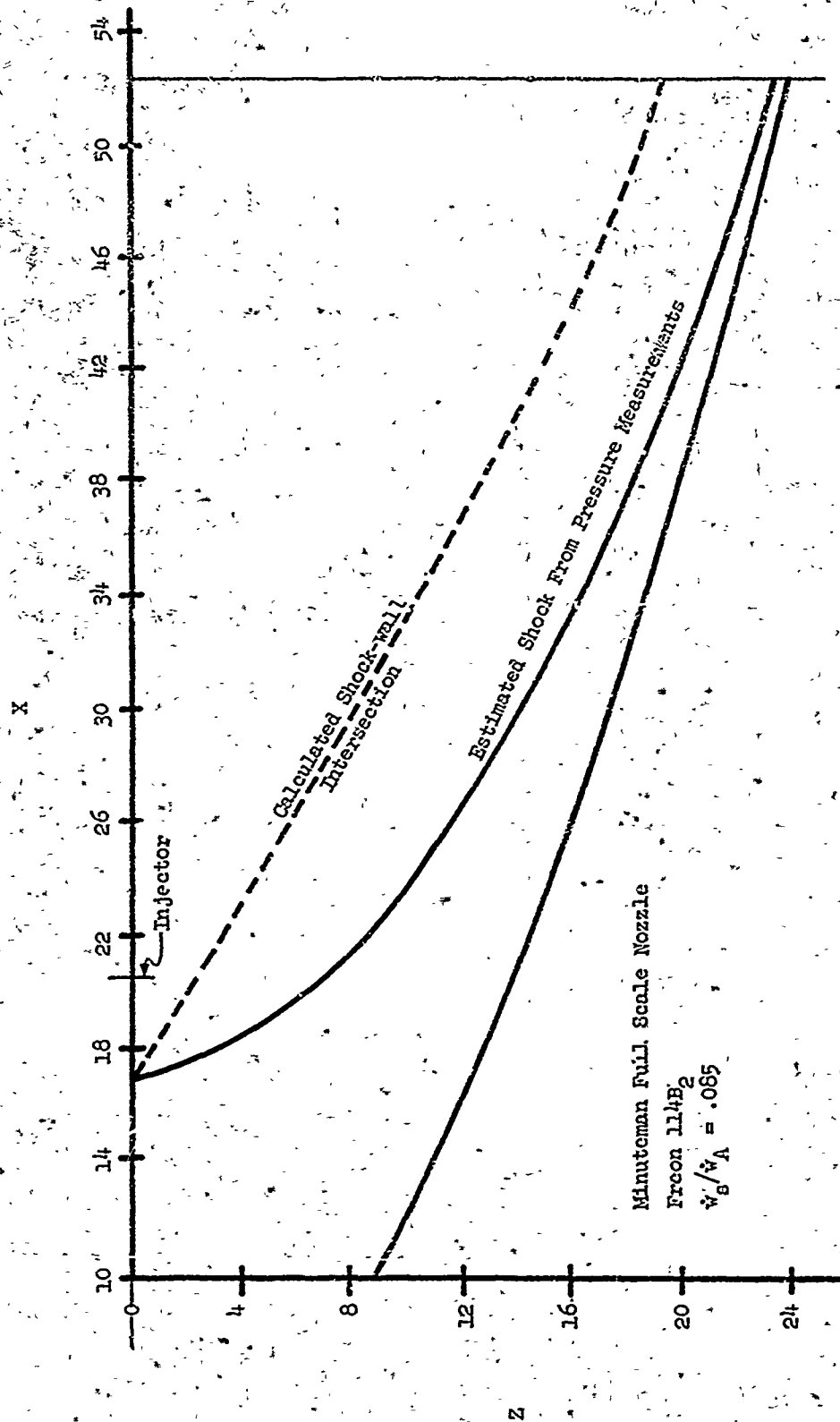


Figure 38

TM-16-SRO

APPENDIX A

VAPOR-BODY CALCULATIONS

The portion of the present liquid-injection model that calculates the equivalent solid body formed by the injectant vapor follows the general approach described by NESCO in Reference 18. A number of modifications have been made, however, to include the effect of variable free-stream conditions, and to improve the vaporization rate and drag coefficient. Further work is required to properly evaluate the coupling effects between the free stream, vapor, and droplets, and to include the effects of liquid-jet penetration.

Since the injectant is assumed to break up into droplets immediately on entering the nozzle, the first step in the present model is the calculation of the mean size droplet trajectory. By considering the droplets along the trajectory as a line source of mass, the distribution of vapor is then found by assuming a semicircular cross-section.

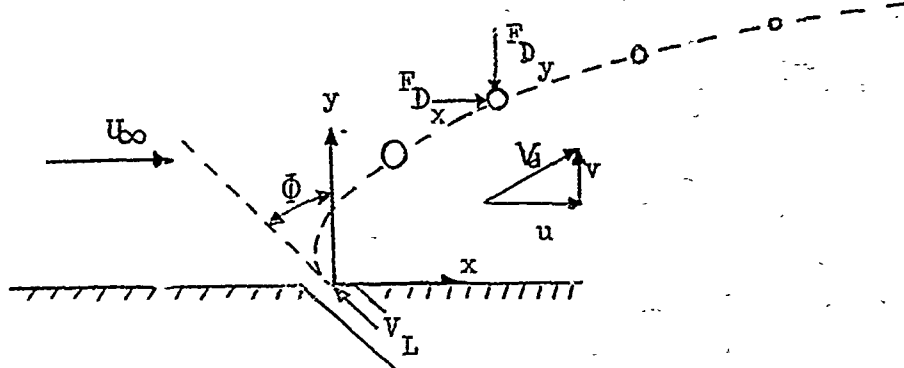
To determine the diameter of the mean size droplet, an empirical relation derived by Ingebo and Foster¹² for injection of a liquid perpendicular to a subsonic free stream is used. The free stream conditions are taken as those behind a normal shock located at the injector.

$$\frac{d_o}{d_i} = 3.9 \left(\frac{W_e}{Re} \right)^{0.25} = 3.9 \left(\frac{g \sigma_L}{\rho_n v_n^2 d_i} : \frac{v_L}{v_n d_i} \right)^{0.25}$$

or

$$d_o = 9.3 \sqrt{d_i} \left(\frac{\sigma_L v_L}{\rho_N v_N^3} \right)^{0.25} \quad (A1)$$

This relation was considered more realistic than the well-known Nukiyama-Tanasawa expression¹¹, which was derived for injection parallel to the freestream and includes no effect of the port diameter.



The equation of motion for a single particle or droplet can be written as

$$\left(\frac{4}{3} \pi r_d^3 \rho_L\right) \frac{d\vec{v}_d}{dt} = \vec{F}_D = \frac{1}{2} \rho_\infty C_D (\pi r_d^2) |\vec{v}_r| \vec{v}_r$$

or

$$\frac{d\vec{v}_d}{|\vec{v}_r| |\vec{v}_r|} = \frac{3}{8} \frac{\rho_\infty}{\rho_L} \frac{C_D}{r_d} dt \quad (A2)$$

In Reference 45, Ingebo formed the following empirical correlation between the drag coefficients for accelerating droplets and the Reynolds number based on the relative velocity between the droplets and free-stream,

$$\vec{C}_D = 27 (\text{Re})_r^{-0.84} = 27 \left(\frac{U_\infty}{\rho_\infty |\vec{v}_r| 2r_d} \right)^{0.84} \quad (A3)$$

$$\text{for } 6 < |(\text{Re})_r| < 400$$

The rate of vaporization is assumed to be proportional to the surface area of the droplet, or

$$\beta = - \frac{d(r_d^2)}{dt} = -2r_d \frac{dr_d}{dt} \quad (A4)$$

An expression for this vaporization rate is given in Reference 46 for quasi-steady-state evaporation of a spherical droplet in a stagnant atmosphere,

$$\beta_o = \frac{2 \lambda v}{c_{p_v} \rho_L} \ln \left[1 + \frac{T_\infty - T_L}{L_v / c_{p_v}} \right] \quad (A5)$$

An empirical correction can be made to this equation to make it applicable for fluid motion with respect to the droplet,⁴⁶

$$\beta = \beta_o \left(1 + 0.276 \operatorname{Re}_r^{1/2} \operatorname{Pr}^{1/3} \right) \quad (A6)$$

To arrange the trajectory equations into their final forms, equation (A4) is first rewritten as

$$2r_d dr_d = -\beta dt \quad (A7)$$

Writing equation (A2) in component form, and substituting equation (A4) into it gives:

$$\frac{du}{(U_\infty - u)^2} = -\frac{3}{4} \frac{\rho_\infty}{\rho_L} \frac{(c_D)_x}{\beta} dr_d \quad (A8)$$

$$\frac{dv}{v^2} = \frac{3}{4} \frac{\rho_\infty}{\rho_L} \frac{(c_D)_y}{\beta} dr_d \quad (A9)$$

Equations (A7), (A8), and (A9) form a set of simultaneous ordinary differential equations to be solved for the droplet radius, r_d , and the droplet velocity components u and v as a function of time, t .

To describe the actual droplet trajectory, the following two equations are then needed,

$$dx = u dt \quad (A10)$$

$$dy = v dt \quad (A11)$$

After determining the droplet trajectory, the next step is the calculation of the body formed by the vapor. The mass of vapor generated per drop in an interval $d\xi$ along the droplet trajectory is

$$dm = \rho_L 4\pi r_d^2 dr_d \quad (A12)$$

Substituting equation (A4) into the above expression gives

and

$$\frac{dm}{dt} = 2\pi \rho_L r_d \beta$$

$$\frac{dm}{d\xi} = \frac{dm}{dt} \cdot \frac{dt}{d\xi} = \frac{2\pi \rho_L r_d \beta}{v_d} \quad (A13)$$

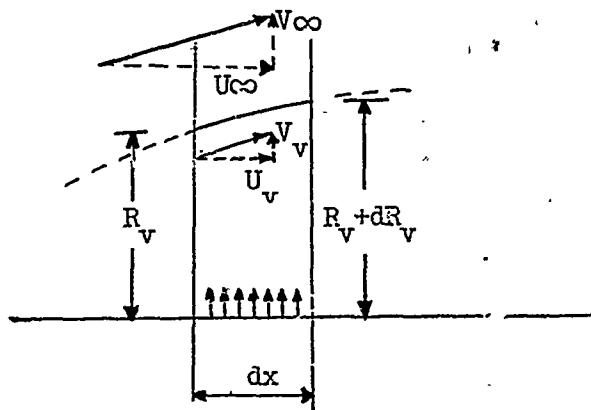
The total number of droplets per unit time entering the nozzle is

$$N = \frac{\dot{w}_s}{\frac{4}{3} \pi r_o^3 \rho_L} \quad (A14)$$

Multiplying equation (A13) by equation (A14) gives the total mass of vapor per unit time generated in the interval $d\xi$,

$$\frac{d\dot{w}}{d\xi} = N \frac{dm}{d\xi} = \frac{3}{2} \frac{\dot{w}_s r_d \beta}{r_o^3 v_d} \quad (A15)$$

Since the droplet trajectories are very close to the wall, as shown in Figure A1 the droplets are assumed to form a line source lying along the nozzle wall. The vapor thus forms a half-body of revolution also lying along the wall.



The radial velocity of the vapor at the surface of the body due to the line source is

$$V_v = \frac{1}{\rho_v \pi R_v} \frac{dw}{dx} \approx \frac{1}{\rho_v \pi R_v} \frac{dw}{d\xi} \quad (A16)$$

and the slope of the vapor body is

$$\frac{dR_v}{dx} = \frac{V_{\infty}}{U_{\infty}} \quad (A17)$$

NESCO in Reference 17 shows by a Taylor series expansion in ρv that at the body surface

$$\rho_v V_v \approx \rho_{\infty} V_{\infty} \quad (A18)$$

Therefore, substituting equations (A16) and (A18) into (A17) gives

$$\frac{dR_v}{dx} = \frac{1}{\rho_\infty U_\infty} \frac{1}{\pi R_v} \frac{d\dot{w}}{d\xi} \quad (A19)$$

and with equation (A15)

$$2R_v dR_v = \frac{3}{\pi} \frac{\dot{w}_s r_d \beta}{\rho_\infty U_\infty r_o^3 v_d} dx \quad (A20)$$

Equations (A7) through (A11) and equation (A20) constitute 6 equations for the 6 unknowns, u , v , x , y , r_d , and R_v as functions of the independent variable t . Since this is a "marching type" problem, the equations can be put into finite-difference form, which allows the numerical solution to advance from given initial values at successive discrete intervals of time.

As an example of the procedure used for deriving the finite difference equations, equation (A8) is integrated across a given interval in the following manner.

$$\int_{u_{n-1}}^{u_n} \frac{du}{(\bar{U}_\infty - u)^2} \approx -\frac{3}{4} \frac{\bar{\rho}_\infty (\bar{C}_D)_x}{\rho_L \bar{\beta}} \int_{(r_d)_{n-1}}^{(r_d)_n} dr_d \quad (A21)$$

where the quantities $\bar{\rho}_\infty$, \bar{U}_∞ , $(\bar{C}_D)_x$, and $\bar{\beta}$ are taken as constant average values in each interval. The above equation can then be integrated to give

$$\left(\frac{1}{\bar{U}_\infty - u_n} \right) - \left(\frac{1}{\bar{U}_\infty - u_{n-1}} \right) = \frac{3}{4} \frac{\bar{\rho}_\infty (\bar{C}_D)_x}{\rho_L \bar{\beta}} \left[(r_d)_{n-1} - (r_d)_n \right] \quad (A22)$$

or

$$u_n = \bar{U}_\infty - 1 / \left[\left(\frac{1}{\bar{U}_\infty - u_{n-1}} \right) + \frac{3}{4} \frac{\bar{\rho}_\infty (\bar{C}_D)_x}{\rho_L \bar{\beta}} \left[(r_d)_{n-1} - (r_d)_n \right] \right]$$

The other finite difference equations can be derived in a similar manner, and are listed below

$$(r_d)_n = \left[(r_d)_{n-1}^2 - \bar{\beta} (t_n - t_{n-1}) \right]^{1/2} \quad (A23)$$

$$v_n = 1 / \left\{ \frac{1}{v_{n-1}} + \frac{3}{4} \frac{\bar{\rho}_{\infty} (\bar{C}_D)_y}{\rho_L \bar{\beta}} \left[(r_d)_{n-1} - (r_d)_n \right] \right\} \quad (A24)$$

$$x_n = x_{n-1} + \frac{u_n + u_{n-1}}{2} (t_n - t_{n-1}) \quad (A25)$$

$$x_n = y_{n-1} + \frac{v_n + v_{n-1}}{2} (t_n - t_{n-1}) \quad (A26)$$

$$(R_v)_n = \left\{ (R_v)_{n-1}^2 + \frac{3}{\pi} \frac{\dot{w}_s \bar{\beta}}{\bar{\rho}_{\infty} \bar{U}_{\infty} r_o^3} \left[\frac{(r_d)_n + (r_d)_{n-1}}{(v_d)_n + (v_d)_{n-1}} \right]^{1/2} (x_n - x_{n-1}) \right\} \quad (A27)$$

where

$$v_d = (u^2 + v^2)^{1/2}$$

The initial values used (@t = C) are

$$u_o = -V_L \sin \varphi$$

$$v_o = V_L \cos \varphi$$

$$x_o = y_o = (R_v)_o = 0$$

$$r_o = \frac{d_o}{2}$$

where d_o is calculated by equation (A1)

For the solution, an iteration technique is used in which the values for $\overline{P_{00}}$, $\overline{U_{00}}$, $\overline{\beta}$, $(\overline{C_D})_x$, and $(\overline{C_D})_y$ for the first pass in a given interval, take the form

$$\overline{a} = a_{n-1} \quad (A29)$$

After the first pass through equations (A22) (A27), a new value is given to these terms,

$$\overline{a} = \frac{a_{n-1} + a_n}{2} \quad (A30)$$

where a_n is calculated from the results of the first pass, and the solution is repeated. This procedure continues until successive values calculated for u_n satisfy the following criterion

$$\left| 1 - \frac{(u_n)_i}{(u_n)_{i-1}} \right| < .0001 \quad (A31)$$

The converged values of the dependent variables, A_n , are then used as the initial values, $A_{(n-1)}$, for the next interval to continue the solution.

This solution has been programmed for the GE225 computer and takes approximately 5 minutes per run. This program requires the following input:

1. Propellant Properties

- a) γ , ratio of specific heats
- b) R , Gas Constant, (ft-lbf/lbm-°R)
- c) P_c , Chamber Pressure, (psia)
- d) T_c , Chamber Temperature, (°R)

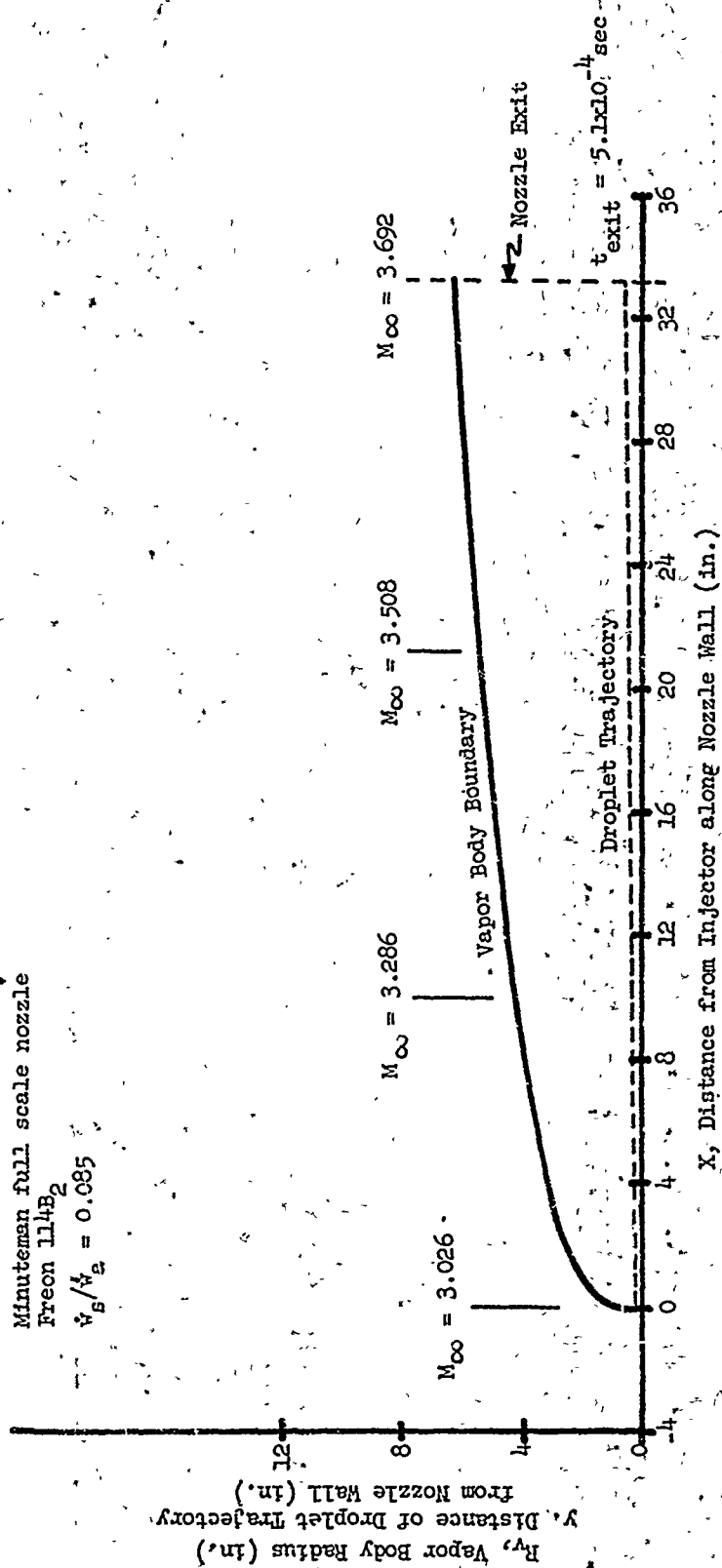
2. Injectant Properties

- a) ρ_L , Liquid Density, (lbm/ft³)
- b) ν_L , Liquid Kinematic viscosity, (ft²/sec)
- c) σ_L , Liquid Surface Tension, (lbm/ft)
- d) λ_v , Vapor Thermal Conductivity, (BTU/sec-ft-°R)
- e) L_v , Latent Heat of Vaporization, (BTU/lbm)
- f) T_L , Boiling Temperature, (°R)
- g) C_{pv} , Vapor Specific Heat, (BTU/lbm-°R)

3. Injector Parameters

- a) \dot{w}_s , injectant mass flow rate, (lbm/sec.)
- b) Φ , injection angle (degrees)
- c) d_i , Port diameter, (in.)
- d) P_{INJ} , Injection pressure, (psia)
- e) C_w , Port Discharge Coefficient

4. Table of Free Stream Mach Numbers vs. X.



Typical Calculated Vapor Body and Droplet Trajectory

Figure 1

TM-16-SRO

APPENDIX B

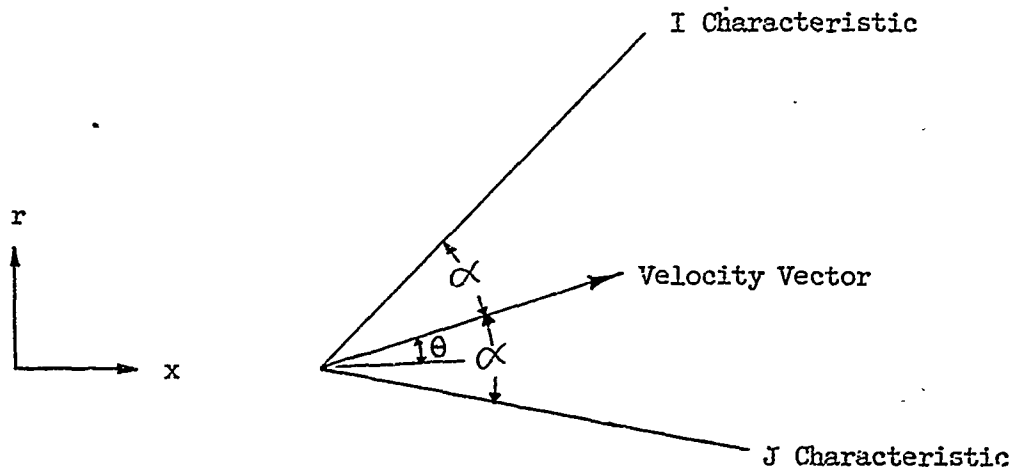
FLOW-FIELD SOLUTION

The method of characteristics has long been recognized as a valuable method for solving hyperbolic partial differential equations, and has been used extensively for compressible, inviscid, supersonic flow field solutions. Mathematically, this method transforms partial differential equations that describe the flow over the entire flow field to ordinary differential equations which apply only along characteristic lines in two-dimensional flow, or characteristic surfaces in three-dimensional flow. The general theory of the method of characteristics and the actual derivation of these ordinary differential equations, sometimes called compatibility equations, will not be discussed here, but can be found in a number of texts, such as Courant and Friedrichs⁴⁷, Ferri⁴⁸, and Shapiro⁴⁹.

Since the flow field for LITVC, as shown in Figure 35, will include curved shocks, the flow behind the shocks will be rotational, i.e., the entropy will be constant along a given streamline, but will vary from one streamline to the other. From Shapiro, for rotational axisymmetric flow, the characteristic lines are the Mach lines, described by the equations,

$$\left(\frac{dr}{dx}\right)_I = \tan(\theta + \alpha) \quad (B1)$$

$$\left(\frac{dr}{dx}\right)_J = \tan(\theta - \alpha) \quad (B2)$$



and the compatibility equations applicable along these lines are

$$(d\theta)_I - \frac{\cot \alpha}{V} (dV)_I + \frac{\sin \theta \sin \alpha}{\sin(\theta + \alpha)} \frac{(dr)_I}{r} - \frac{\sin \alpha \cos \alpha}{\gamma R} (ds)_I = 0 \quad (B3)$$

$$(d\theta)_J + \frac{\cot \alpha}{V} (dV)_J - \frac{\sin \theta \sin \alpha}{\sin(\theta - \alpha)} \frac{(dr)_J}{r} + \frac{\sin \alpha \cos \alpha}{\gamma R} (ds)_J = 0 \quad (B4)$$

The subscript I denotes the left-running characteristic and the subscript J the right-running characteristic. It is usually more convenient to work in terms of Mach Number, M, and flow angle, θ , and the above equations can be transformed to these two variables through the following relations:

$$\sin \alpha = \frac{1}{M} \quad (B5)$$

and for adiabatic flow

$$\frac{dV}{V} = \left(1 + \frac{\gamma-1}{2} M^2\right)^{-1} \frac{dM}{M} \quad (B6)$$

Using these relations, and the corresponding expressions for $\cos \alpha$ and $\tan \alpha$, equations (B1) through (B4) take the following form:

$$\left(\frac{dr}{dx}\right)_I = \frac{\sin \theta \sqrt{M^2 - 1} + \cos \theta}{\cos \theta \sqrt{M^2 - 1} - \sin \theta} \quad (B7)$$

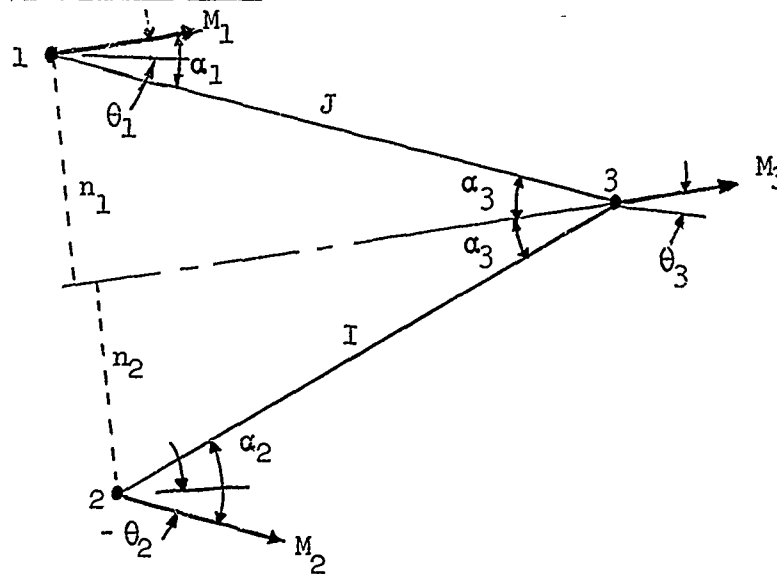
$$\left(\frac{dr}{dx}\right)_J = \frac{\sin \theta \sqrt{M^2 - 1} - \cos \theta}{\cos \theta \sqrt{M^2 - 1} + \sin \theta} \quad (B8)$$

$$(d\theta)_I - \frac{\sqrt{M^2 - 1}}{\left(1 + \frac{\gamma-1}{2} M^2\right)} \frac{(dM)_I}{M} + \frac{\sin \theta}{\sin \theta \sqrt{M^2 - 1} + \cos \theta} \frac{(dr)_I}{r} - \frac{\sqrt{M^2 - 1}}{\gamma R M^2} (ds)_I = 0 \quad (B9)$$

$$(d\theta)_J + \frac{\sqrt{M^2 - 1}}{\left(1 + \frac{\gamma-1}{2} M^2\right)} \frac{(dM)_J}{M} - \frac{\sin \theta}{\sin \theta \sqrt{M^2 - 1} - \cos \theta} \frac{(dr)_J}{r} + \frac{\sqrt{M^2 - 1}}{\gamma R M^2} (ds)_J = 0 \quad (B10)$$

The numerical solution of these equations covers the entire flow field through a combination of three basic solutions - the interior point, boundary point, and shock point.

1. Interior Point Solution



Given M , θ , and s , as well as the coordinates x and y , at two initial points, the solution can be extended to a third point located at the intersection of the characteristics of opposite families from the original two points. Actually, the characteristics are curved for a non-uniform flow field, but are approximated by straight lines between successive points with a slope based upon the average of the flow properties at each point. Thus, for accuracy, the size of the characteristic net should be kept relatively small.

For the step-by-step solution to this "marching" problem, equations (B7) through (B10) must first be put into finite difference form. Using the notation in the above figure,

$$\frac{r_3 - r_2}{x_3 - x_2} = \frac{\sin \bar{\theta}_I \sqrt{\bar{M}_I^2 - 1} + \cos \bar{\theta}_I}{\cos \bar{\theta}_I \sqrt{\bar{M}_I^2 - 1} - \sin \bar{\theta}_I} \quad (B11)$$

$$\frac{r_3 - r_1}{x_3 - x_1} = \frac{\sin \bar{\theta}_J \sqrt{\bar{M}_J^2 - 1} - \cos \bar{\theta}_J}{\cos \bar{\theta}_J \sqrt{\bar{M}_J^2 - 1} + \sin \bar{\theta}_J} \quad (\text{B12})$$

$$(\theta_3 - \theta_2) - \left[\frac{\sqrt{\bar{M}_I^2 - 1}}{(1 + \frac{\gamma - 1}{2} \bar{M}_I^2)} \right] \frac{(M_3 - M_2)}{\bar{M}_I} + \left[\frac{\sin \bar{\theta}_I}{\sin \bar{\theta}_I \sqrt{\bar{M}_I^2 - 1} + \cos \bar{\theta}_I} \right] \frac{2(r_3 - r_2)}{(r_3 + r_2)} -$$

$$\left[\frac{778 \sqrt{\bar{M}_I^2 - 1}}{\gamma R \bar{M}_I^2} \right] (s_3 - s_2) = 0 \quad (\text{B13})$$

$$(\theta_3 - \theta_1) + \left[\frac{\sqrt{\bar{M}_J^2 - 1}}{(1 + \frac{\gamma - 1}{2} \bar{M}_J^2)} \right] \frac{(M_3 - M_1)}{\bar{M}_J} - \left[\frac{\sin \bar{\theta}_J}{\sin \bar{\theta}_J \sqrt{\bar{M}_J^2 - 1} - \cos \bar{\theta}_J} \right] \frac{2(r_3 - r_1)}{(r_3 + r_1)} +$$

$$\left[\frac{778 \sqrt{\bar{M}_J^2 - 1}}{\gamma R \bar{M}_J^2} \right] (s_3 - s_1) = 0 \quad (\text{B14})$$

$\bar{\theta}_I$ and \bar{M}_I denote average values along the I characteristic between points 2 and 3, while $\bar{\theta}_J$ and \bar{M}_J are average values along the J characteristic between 1 and 3.

An additional equation is required to permit a solution for the five unknowns x_3 , r_3 , M_3 , and θ_3 and s_3 . By appropriately interpolating between points 1 and 2 to locate the streamline passing through point 3, s_3 can be expressed in terms of s_1 and s_2 . Following the approach of Shapiro⁴⁹, and again referring to the last sketch, normals to the streamline through 3 can be drawn from points along the characteristics. Since the entropy can change only along the normals, the change in entropy along the I characteristic can be expressed as

$$(ds)_I = \frac{ds}{dn} (dn)_I \quad (15)$$

$$\text{where } (dn)_I = \frac{\sin \bar{\alpha}_I}{\sin (\bar{\theta}_I + \bar{\alpha}_I)} \quad (dr)_I = \frac{1}{\sin \bar{\theta}_I \sqrt{\bar{M}_I^2 - 1} + \cos \bar{\theta}_I} (dr)_I \quad (B15)$$

The normal entropy gradient can be approximated by the difference in entropy of points 1 and 2 divided by the distance between the streamlines through 1 and 2 measured along the normal to the stream line through 3, or

$$\frac{ds}{dn} \approx \frac{s_1 - s_2}{n_1 + n_2} = \frac{s_1 - s_2}{\frac{(x_3 - x_1) \sin \bar{\alpha}_J}{\cos (\bar{\theta}_J - \bar{\alpha}_J)} + \frac{(x_3 - x_2) \sin \bar{\alpha}_I}{\cos (\bar{\theta}_I + \bar{\alpha}_I)}} \quad (B16)$$

Therefore, substituting equation (B16) into (B15), transforming to the variables M and θ , and writing the result in finite difference form gives:

$$s_3 - s_2 = \left[\frac{s_1 - s_2}{\frac{(x_3 - x_1)}{\cos \bar{\theta}_J \sqrt{\bar{M}_J^2 - 1} + \sin \bar{\theta}_J} + \frac{(x_3 - x_2)}{\cos \bar{\theta}_I \sqrt{\bar{M}_I^2 - 1} - \sin \bar{\theta}_I}} \right] \left(\frac{r_3 - r_2}{\sin \bar{\theta}_I \sqrt{\bar{M}_I^2 - 1} - \cos \bar{\theta}_I} \right) \quad (B17)$$

Equation (B17) added to equations (B11) through (B14) constitute the complete set of simultaneous equations to be solved for x_3 , r_3 , M_3 , θ_3 , and s_3 . This solution proceeds in the following manner:

- a. Setting $\bar{M}_I = M_2$, $\bar{\theta}_I = \theta_2$, $\bar{M}_J = M_1$, $\bar{\theta}_J = \theta_1$, equations (B11) and (B12) are solved simultaneously for x_3 and r_3 .
- b. Equation (B17) is solved for s_3 .
- c. Equations (B13) and (B14) are solved simultaneously for M_3 and θ_3 .
- d. Now setting $\bar{M}_I = \frac{M_2 + M_3}{2}$, $\bar{\theta}_I = \frac{\theta_2 + \theta_3}{2}$, $\bar{M}_J = \frac{M_1 + M_3}{2}$, and $\bar{\theta}_J = \frac{\theta_1 + \theta_3}{2}$,

Equations (B11) and (B12) are again solved for new values of x_3 and r_3 .

Steps b, c, and d are repeated until successive values of M_3 satisfy the following criterion:

$$|(M_3)_n - (M_3)_{n-1}| < .0001$$

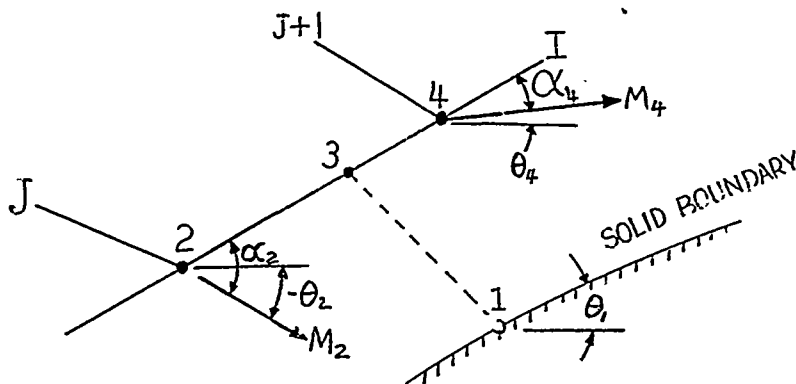
The total pressure at point 3 is a function of the entropy at 3 and the total pressure and entropy at some reference station

$$P_{t_3} = P_{t_o} \exp \left[\frac{778(s_o - s_3)}{R} \right] \quad (B18)$$

For the LITVC flow field solution, P_{t_o} is taken as the chamber pressure and s_o is set equal to zero. The static pressure can now be calculated from the isentropic pressure ratio based upon P_{t_3} , which is constant along the streamline through point 3.

$$P_3 = P_{t_3} \left(1 + \frac{\gamma-1}{2} M_3^2 \right)^{\frac{\gamma}{1-\gamma}} \quad (B19)$$

2. Boundary Point Solution



In the LITVC flow field solution, the pressure must be calculated along the solid boundary formed by the vapor body and forward separation region.

Knowing the flow properties at two points, along an upstream I characteristic, and x , r , θ , and s at the solid boundary point, the Mach number at 1 can be calculated by the following procedure.

a. The initial values for M_1 and M_3 are set equal to $\frac{M_2 + M_4}{2}$.

b. Setting $\bar{M}_I = \frac{M_2 + M_4}{2}$, $\bar{\theta}_I = \frac{\theta_2 + \theta_4}{2}$, $\bar{M}_J = \frac{M_1 + M_3}{2}$, and $\bar{\theta}_J = \frac{\theta_1 + \theta_3}{2}$,

point 3 is located by solving equations (B11) and (B12) as in the interior point solution.

c. M_3 , θ_3 and s_3 are calculated by linearly interpolating along the I characteristic between points 2 and 4, i.e.

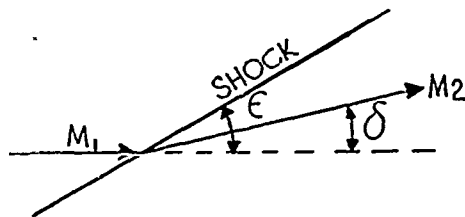
$$M_3 = M_2 + \frac{(x_3 - x_2)}{(x_4 - x_2)} (M_4 - M_2)$$

d. Equation (B14) can now be solved directly for M_1 , and steps b, c, and d repeated until successive values of M_1 satisfy the criterion

$$|(M_1)_n - (M_1)_{n-1}| < .0001$$

The static pressure can then be calculated with equations (B18) and (B19).

3. Shock Point Solution

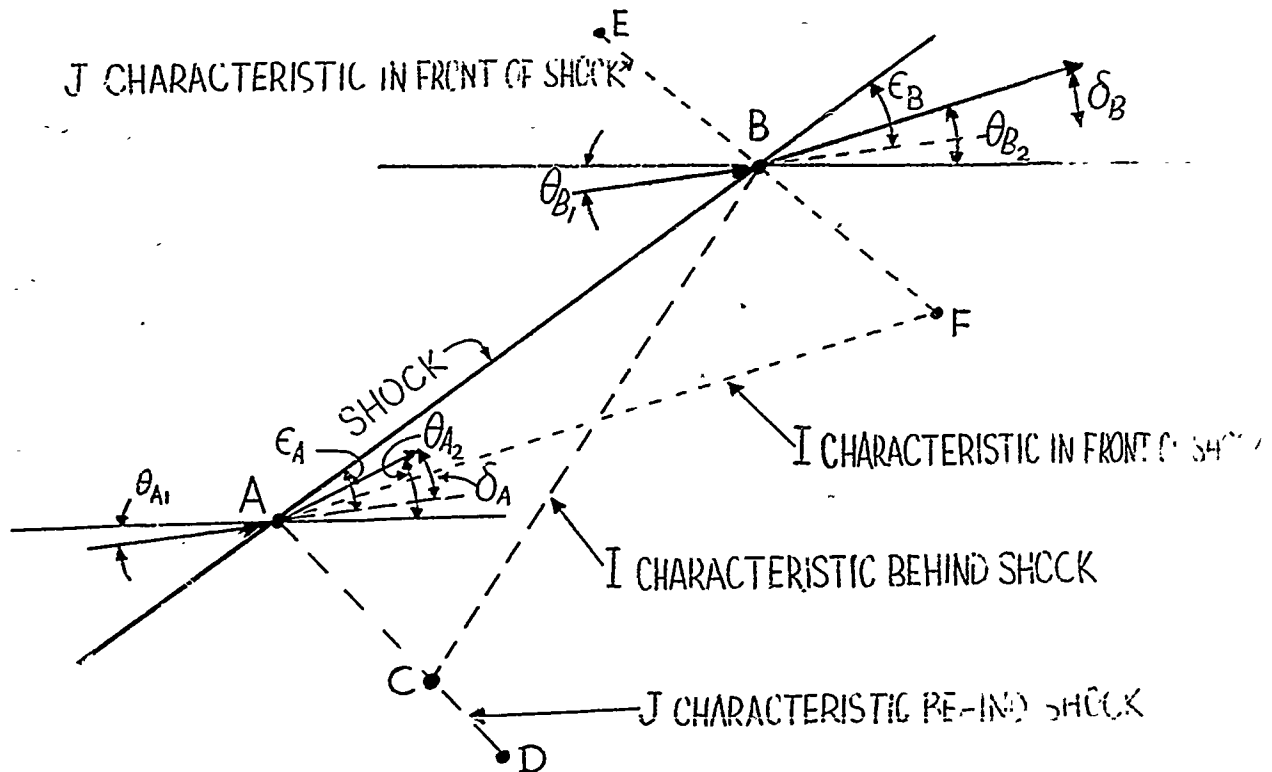


For a given Mach number before an oblique shock, M_1 , and a given flow deflection, δ , through the shock, the Mach number behind the shock, M_2 , the shock angle, ϵ , with respect to M_1 , and the entropy rise across the shock, $s_2 - s_1$, can be calculated with the following relations:

$$\cot \delta = \left(\frac{\gamma + 1}{2} \frac{M_1^2}{M_1^2 \sin^2 \epsilon - 1} - 1 \right) \tan \epsilon \quad (B20)$$

$$M_2 = \frac{1}{\sin(\epsilon - \delta)} \left[\frac{\gamma + 1}{2} \frac{\tan \epsilon}{\tan(\epsilon - \delta)} - \frac{\gamma - 1}{2} \right]^{-1/2} \quad (B21)$$

$$s_2 - s_1 = \frac{R}{\gamma - 1} \ln \left[\frac{2\gamma}{\gamma + 1} M_1^2 \sin^2 \epsilon - \frac{\gamma - 1}{\gamma + 1} \right] + \frac{\gamma R}{\gamma - 1} \ln \left[\frac{2}{(\gamma + 1) M_1^2 \sin^2 \epsilon} + \frac{\gamma - 1}{\gamma + 1} \right] \quad (B22)$$



To calculate the shock point B, the flow properties must be known at point E in front of the shock, at point A both in front of (A1) and behind (A2) the shock, and at point D on the same J characteristic behind the shock as A2. The following procedure is then used:

- a. The imaginary point F is calculated with the interior point solution using the properties at E and A1.
- b. For $\delta = \theta_{A2} - \theta_{A1}$ and $M_1 = M_{A1}$, the shock angle at A, ϵ_A , is calculated with equation (B20) using an iterative procedure.
- c. Point B is located at the intersection of the J characteristic between E and F and the shock extended from A at the angle $(\epsilon_A + \theta_{A1})$ with the horizontal.
- d. At B, the flow properties in front of the shock (B1) are calculated by interpolating between E and F.
- e. From Equation (B20) with $M_1 = M_{B1}$ and $\epsilon = \epsilon_A$, δ_B is calculated, and $\theta_{B2} = \theta_{B1} + \delta_B$. M_{B2} is calculated from equation (B21) and s_{B2} from equation (B22).
- f. For $\bar{M}_I = M_{B2}$, $\bar{\theta}_I = \theta_{B2}$, $\bar{M}_J = \frac{M_{A2} + M_D}{2}$, and $\bar{\theta}_J = \frac{\theta_{A2} + \theta_D}{2}$, equations (B11) and (B12) are used to find point C.
- g. The flow properties at C are found by interpolating between A2 and D.
- h. For $\bar{M}_I = \frac{M_{B2} + M_C}{2}$, $\bar{\theta}_I = \frac{\theta_{B2} + \theta_C}{2}$, equations (B11) and (B12) are again used to find a new point C.
- i. Steps g and h are repeated until $|(M_C)_n - (M_C)_{n-1}| < .0001$

j. Equation (B13) is used to calculate a new value for θ_{B2} , which is averaged with the last value to calculate a new δ_B , $\delta_B = \frac{\theta_{B2} + \theta_{B1}}{2}$.

k. The shock angle at B, ϵ_B , is calculated with Equation (B20) for $M_1 = M_{B1}$ and $\epsilon = \epsilon_B$.

l. A new point B is located by extending the shock from A now at the angle $(\frac{\epsilon_A + \epsilon_B}{2}) + \theta_{A1}$ to the horizontal and intersecting the J characteristic between E and F.

m. Steps d through l are repeated until successive values of M_{B2} satisfy the criteria $| (M_{B2})_n - (M_{B2})_{n-1} | < .0001$.

Once the flow properties at B2 are found, they are used, along with the properties at D, to find a new interior point and continue the solution.

The three basic point solutions just described have been combined into a computer program for the IBM 7094, which takes less than 1 minute per case for a typical flow field. The input required for this program is M , θ , s , x , and r at a number of points in front of the shock, and θ , s , x and r at points along the lower boundary. The logic followed by the program is:

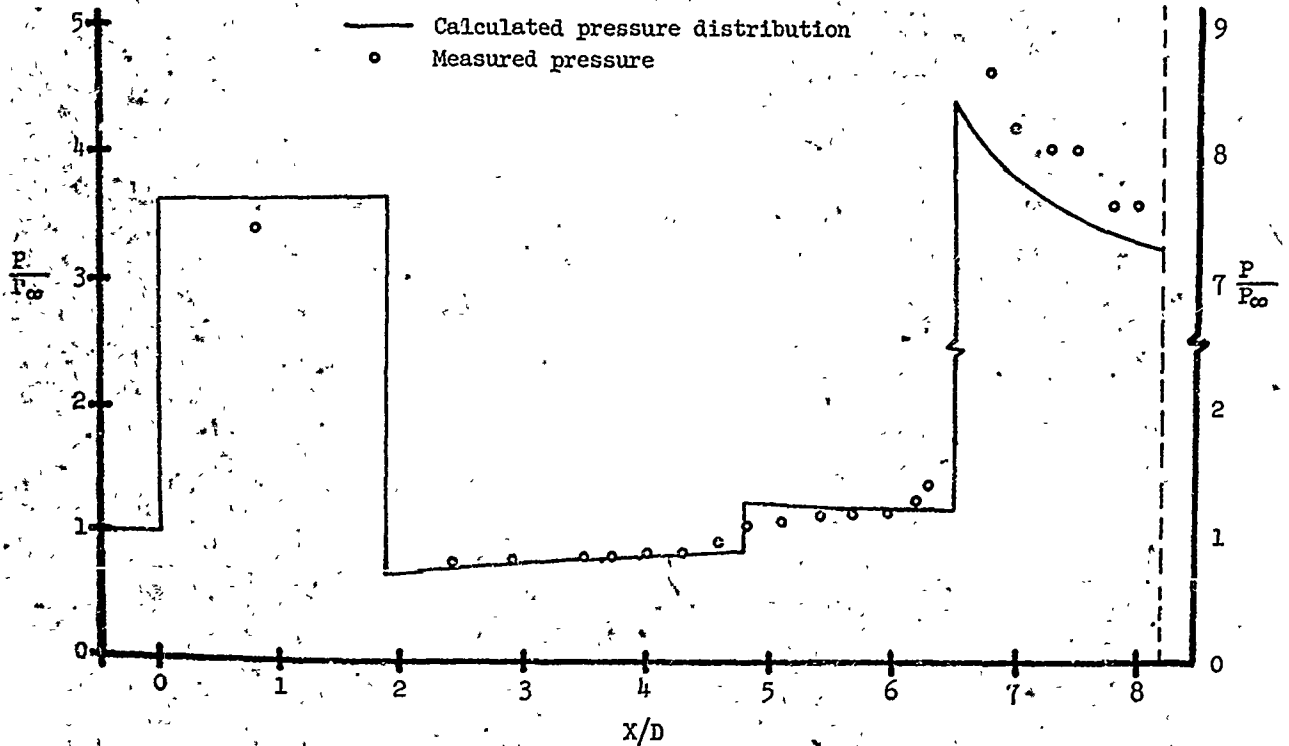
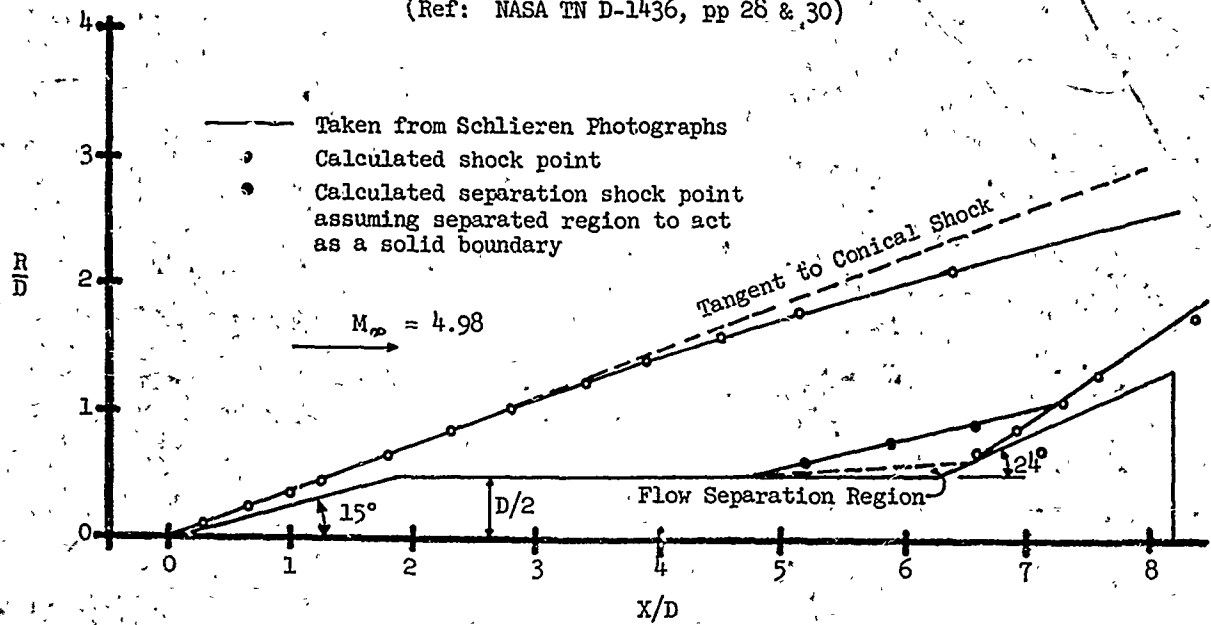
- a. Calculate the shock point;
- b. Continue the solution by calculating interior points along the J characteristic from the shock point until the lower boundary or last I characteristic is reached;
- c. Calculate the next lower boundary point, if there is one, and the interior point at the intersection of the I characteristic from the boundary point with the J characteristic being computed.

TM-16-SRO, Appendix B

d. Repeat a, b, and c until all the initial points in front of the shock are used.

Figure B1 compares the shock shape and pressure distribution calculated by this program with experimental data. Very good correlation has been obtained.

(Ref: NASA TN D-1436, pp 28 & 30)



Comparison of Calculated Shock Shapes and Pressure Distributions with Experimental Data

Figure 1